Tesis Doctoral

Observaciones multifrecuencia de blazares TeV con datos del telecospio Whipple y VERITAS

Pichel, Ana Carolina

2012-03-19

UNIVERSIDAD DE BUENOS AIRES

Facultad de Ciencias Exactas y Naturales

Departamento de Física

Observaciones multifrecuencia de blazares TeV con datos del telescopio Whipple y VERITAS

Tesis presentada para optar al título de Doctor
de la Universidad de Buenos Aires en el área de Ciencias Físicas

Ana Carolina Pichel

Director de Tesis: Dr. Adrián C. Rovero

Consejero de Estudios: Dr. Daniel Gómez

Lugar de Trabajo: Instituto de Astronomía y Física del Espacio

Buenos Aires, 2012

Observaciones multifrecuencia de blazares TeV con datos del telescopio Whipple y VERITAS

Resumen

En este trabajo se presenta un estudio multi-frecuencia sobre los blazares Mrk 421 y Mrk 501, realizado a partir de tres campañas multi-frecuencia llevadas a cabo durante las temporadas de observación 2007-08 y 2008-09. Los datos analizados incluyen mediciones realizadas en el Observatorio Whipple para rayos gamma de muy alta energía (VHE), por *Fermi*-LAT para rayos gamma de alta energía, por *Swift* y RXTE para rayos X, y con varios telescopios en la banda óptica y de radio-frecuencias. El telescopio Whipple estuvo dedicado a monitorear las fuentes Mrk 421 y Mrk 501 durante meses, todas las noches en que fuera posible. Estas observaciones, sumadas a las realizadas con VERITAS, de mayor sensibilidad y menor umbral de energía de detección, permitieron lograr un excepcional muestreo para la banda VHE de rayos gamma. Los comportamientos observados para estas fuentes durante las campañas fueron muy diferentes entre sí, presentándose períodos de baja y alta actividad en casi todas las bandas del espectro, incluyendo episodios de alta actividad en la banda VHE. Se estudió la correlación en el flujo y la energía espectral entre la banda VHE y el resto de las bandas de energía. También se analizó la variabilidad en tiempos largos y cortos. Se obtuvo la distribución espectral de energía para los distintos estados de actividad, para las dos fuentes, observándose un buen acuerdo entre los datos y los ajustes realizados empleando el modelo synchrotron-self-Compton. Estos resultados son compatibles con que los electrones acelerados son los responsables de la emisión gamma de muy altas energías en estos blazares.

Palabras Clave: rayos gamma de muy alta energía, AGN, blazares, telescopios Cherenkov, variabilidad, SED

Multi-wavelength observations of TeV blazars including Whipple telescope and VERITAS

Abstract

In this work, a multi-wavelength study of the TeV blazars Mrk 421 and Mrk 501 is reported. The survey comprehends three multi-wavelength campaigns performed during two observing seasons: 2007-08 and 2008-09. Analyzed data include observations from the Whipple Observatory for very-high-energy (VHE) gamma-rays, *Fermi*-LAT for high-energy gamma-rays, *Swift* and RXTE for X-rays, and various instruments covering the optical and radio bands. The Whipple 10 m telescope was dedicated to monitoring Mrk 421 and Mrk 501; conducting observations every night it was possible. By combining Whipple data with observations performed by VERITAS (with higher sensitivity and lower energy threshold for detection) an outstanding coverage for months in the VHE band was obtained. The behavior observed during the campaigns was substantially different for each source. Periods of low and high activity were observed for almost all the energy bands, even including VHE flares. Correlations between VHE gamma-rays and the other bands in flux and spectral energy were analyzed, and searches for short/long term variability were conducted. The spectral energy distribution for each campaign, and for different periods of activity in each source, was obtained, being well described by the one-zone synchrotron-self-Compton model. These results are compatible with the explanation that accelerated electrons are responsible for the VHE gamma-ray emission in these blazars.

Key Words: very-high-energy gamma-rays, AGN, TeV blazars, Cherenkov telescopes, variability, SED

Acknowledgments

This work was supported by fellowships from CONICET, AGENCIA, SAO; and grants by several PICT, and international collaborations.

I would like to thank all the people who contributed to accomplish this work.

My advisor, Adrián Rovero, for giving me the chance to work in such a great experiment; for giving me freedom to find my own way and being always available to discuss various matters of my work.

Trevor Weekes, for affording me the opportunity to spend several months at the Whipple Observatory; for his generous support during my visits; for his guidance, encouragement and patience.

John Kildea, for providing me useful, pertinent suggestions, which helped me in all aspects of work in VERITAS. Besides, for his hospitality, shared trips and, especially, for teaching me everything about *our* telescope.

Wystan Benbow, for patiently answering all my emails with questions about blazars.

I would also like to thank all VERITAS members, with whom I shared funny moments during observations and meetings along my PhD.

Rox, for the mojitos and happy hours; Víctor, for all the amusement in Tucson, the great parties, and for driving me to M'Elios to eat real Italian food; Ester, Andrea, Angelo, Luis and Gunes (the only person who needs two hours to get the basecamp from the Ridge), for all the shared funny moments. John E. and Mark, for sharing the St. Patrick festivities in Tucson.

Karen, for rescuing me a very hot summer Sunday afternoon when my car was broken at the I-19; Jeremy, for fixing computing problems, and for my first and only Kentucky Derby; and all the people at the basecamp: Ken, Steve, Gene, Ginnee, Cezar, Grace and Danny, for their help in many matters.

I want also to thank my family and friends, without whom this work would not have been possible either. My working mates, Andrea, Gaby, Tama, Daniel and Analía, for making of the work a fun place to go every day. My university friends, Rata, Pablo, Agus, Karo, Mariano and the rest of them, for sharing classes and study hours. My first friends, Marisa and Daniela, for having been with me for more than 30 years. My sisters and little brothers, for making my life happier every day. My parents, for teaching me passion for everything I make, to stand up and face life and consequences. Finally, Ariel, for his patience, love, and for making me laugh no matter of what.

Table of Contents

1 Introduction **1**
- 1.1 General Contents . . . 1
- 1.2 Gamma rays . . . 2
- 1.3 Gamma-ray Astronomy . . . 3
  - 1.3.1 Standard Candle: Crab Nebula . . . 7
- 1.4 AGN: Blazars . . . 8
  - 1.4.1 Blazar Spectral Energy Distribution and Emission Models . 10
  - 1.4.2 Markarian 421 . . . 16
  - 1.4.3 Markarian 501 . . . 17

2 Multi-Wavelength Observations **19**
- 2.1 X-rays . . . 19
  - 2.1.1 *Swift* . . . 19
  - 2.1.2 RXTE . . . 21
- 2.2 HE γ-rays . . . 23
  - 2.2.1 *Fermi* . . . 24
- 2.3 Radio . . . 27
  - 2.3.1 Metsähovi Radio Observatory . . . 27
  - 2.3.2 UMRAO . . . 28
  - 2.3.3 OVRO . . . 28
- 2.4 Optical . . . 29
  - 2.4.1 MITSuME . . . 30
  - 2.4.2 WIYN . . . 30
  - 2.4.3 GASP . . . 31

3 Very High Energy γ-ray Techniques & Instrumentation **33**
- 3.1 Extensive Air Showers . . . 33
  - 3.1.1 γ-ray Air Showers . . . 34
  - 3.1.2 Cosmic-ray Air Showers . . . 34
- 3.2 Cherenkov Light in Air Showers . . . 37
- 3.3 Imaging Atmospheric Cherenkov Technique . . . 40
- 3.4 The Whipple 10m Telescope . . . 41
  - 3.4.1 Whipple Data Acquisition System and Data Analysis . . . 42
- 3.5 VERITAS . . . 50
  - 3.5.1 VERITAS Data Acquisition System . . . 52
  - 3.5.2 VERITAS Calibration and Simulation . . . 53

3.5.3 VERITAS Data Analysis 54

4 Whipple Calibration Methods and Simulations 55
4.1 Whipple Calibration 55
4.1.1 Flat-fielding System and Pointing Corrections 56
4.1.2 Optimization of image cuts 60
4.2 Whipple Simulations 63
4.2.1 Whipple 10m Spectral Reconstruction 63
4.2.2 Results from Crab Nebula Observations 66

5 Multi-wavelength Campaigns of Mrk 421 & Mrk 501 75
5.1 Multi-wavelength Lightcurves 76
5.1.1 Markarian 421 in 2007-08 76
5.1.2 Markarian 501 in 2008 79
5.1.3 Markarian 501 in 2009 80
5.2 Variability & Correlation 91
5.2.1 Markarian 421 in 2007-08 92
5.2.2 Markarian 501 in 2008 96
5.2.3 Markarian 501 in 2009 98
5.3 Spectral Energy Distribution 101
5.3.1 Markarian 421 in 2007-08 101
5.3.2 Markarian 501 in 2008 102
5.3.3 Markarian 501 in 2009 104

6 Conclusions 109

List of Figures

1.1 Electromagnetic Spectrum 2
1.2 Extragalactic VHE sources 4
1.3 Multi-wavelength images of the Crab Nebula 8
1.4 SED of the Crab Nebula 8
1.5 AGN old classification 9
1.6 AGN classification 10
1.7 Extragalactic VHE sources 11
1.8 The SED of Mrk421 12
1.9 Extraordinary VHE flare from PKS2155-304 in 2006 13
1.10 SED of Mrk 421 with old data 16
1.11 SED of Mrk 501 with old data 18

2.1 The *Swift* Satellite 20
2.2 The *Swift*-BAT 58-month all sky monitor survey 21
2.3 Rossi X-ray Timing Explorer 22
2.4 The RXTE spacecraft 23
2.5 The EGRET sky map 24
2.6 Fermi Gamma-ray Space Telescope 25
2.7 Fermi Gamma-ray Space telescope with the two instruments 26
2.8 Fermi-LAT 2nd catalog 26
2.9 Fermi-LAT population from the 2nd catalog 27
2.10 Metsähovi Radio Observatory 28
2.11 UMRAO telescope 29
2.12 OVRO 40 m telescope 29
2.13 MitSume Observatory in Japan 30
2.14 WIYN 3.5 m telescope 31

3.1 Scheme of the development of a gamma-ray and a cosmic-ray induced shower 35
3.2 Simulated air-showers produced by a 1 TeV gamma-ray and proton . 36
3.3 Polarization of the surrounding atoms from a particle traveling in a medium 38
3.4 Cherenkov light distribution from an air shower 39
3.5 Lateral Distribution of the Cherenkov light at two different altitudes 40
3.6 Scheme of a Cherenkov light pool created by a gamma-ray-induced air shower 40

3.7 Schematic illustration of the imaging of an electromagnetic shower in the focal plane of an IACT 41
3.8 The Whipple 10 m telescope 42
3.9 Diagram of the Davies Cotton reflector design 43
3.10 Camera of the Whipple 10 m telescope 43
3.11 Structure of the Whipple 10 m telescope 44
3.12 Diagram of the Whipple 10 m data acquisition system 44
3.13 Hillas's parameters 45
3.14 Example of some Hillas's parameter distributions 46
3.15 Alpha plot distribution for 18 hours of Crab Nebula data taken during 2008-09 season 47
3.16 Images recorded by the Whipple 10 m telescope 48
3.17 VERITAS array with the new configuration 50
3.18 VERITAS camera with the 499 photomultipliers 51
3.19 Example of a gamma-ray event in each telescope of the VERITAS array 51
3.20 Schematic diagram of the VERITAS system trigger 53

4.1 Bright star images at the focal plane of the Whipple 10 m. 57
4.2 Stars offsets as a function of elevation for the 2007-08 observing season. 57
4.3 Stars offsets as a function of azimuth for the 2007-08 observing season 58
4.4 Alpha plots for Mrk 421 with and without pointing corrections. . . . 59
4.5 2D histogram of event lines for *on* and *off* data. 60
4.6 2D histogram of the major axis line for γ-rays events 61
4.7 Significance of γ-ray excess versus selection cut. 62
4.8 Effective area of the Whipple 10 m telescope as function of energy. . 65
4.9 Estimated energy versus true energy of simulated events. 66
4.10 Light curve of the Crab Nebula taken with the Whipple Telescope from 2008-2009 season. 67
4.11 Histograms of parameters derived from raw data before and after applying cuts 68
4.12 Histograms of the excess (ON-OFF differences) in the cut parameter distributions 69
4.13 Simulated gamma-ray cuts parameter distribution versus log(*size*). . 70
4.14 Histograms of the measured excess compared to simulated events for different cuts parameters distribution 71
4.15 Histograms of the measured excess compared to simulated events for log(*size*) and log($E_{\rm est}$) distributions. 72
4.16 Energy spectrum of the Crab Nebula in 2008-09 observations with the Whipple 10 m telescope 72
4.17 Contour plot of the 68 %, 90 % and 95 % confidence intervals from the χ^2 fit to a power law for all the data set 73

5.1 Mrk 421 mwl light curves for 2007-2008 83
5.2 Mrk 421 mwl light curves from March-May 2008 84

5.3 Mrk 421 VHE flare in 080502 85
5.4 Mrk 421 VHE flare in 080503 85
5.5 Mrk 421 VHE flare in 080502 fitted with a simple model 86
5.6 Mrk 501 light curve from March-May 2008 from radio to VHE γ-rays. 87
5.7 Light curves for Mrk 501 from April 17 to May 5, 2009. 88
5.8 Whipple 10 m and VERITAS light curve (4-minute binning) of Mrk 501 for the night of the VHE flare in 2009. 89
5.9 Whipple 10 m light curve of Mrk 501 for the night of the VHE flare in 2009 fitted with a simple model. 89
5.10 Optical flux, degree of the optical linear polarization and EVPA light curves of MRk 501 in 2009. 90
5.11 Fractional variability amplitude for all the instruments involved in the mwl campaign of Mrk421 in 2007-08. 93
5.12 Flux-flux plot for VHE γ-ray with VERITAS and hard X-ray with BAT for Mrk 421. 94
5.13 Flux-flux plot for VHE γ-ray with Whipple and hard X-ray with BAT for Mrk 421. 94
5.14 DCF plot for VHE γ-ray with VERITAS and BAT for Mrk 421. . . 95
5.15 Flux-flux plot for VHE γ-ray with VERITAS and soft X-ray for Mrk 421. 95
5.16 DCF plot for VHE γ-ray and soft X-rays. 96
5.17 Fractional variability amplitude for all the instruments involved in the mwl Campaign in March-May 2008 of Mrk 501. 96
5.18 Flux-flux plot for the VHE gamma-rays, VERITAS and Whipple Telescope, looking for correlations. 97
5.19 Flux-flux plot for the VHE gamma-rays compared to the X-ray with RXTE-PCA. 98
5.20 DCF for the X-ray 2-10 keV versus VHE gamma-ray 98
5.21 Fractional variability amplitude for all the instruments involved in the mwl Campaign in 2008-09 of Mrk 501. 99
5.22 Flux-flux plot for VHE γ-ray with HE γ-ray and X-ray for Mrk 501 in 2009 100
5.23 Spectrum of Mrk 421 obtained with VERITAS during the nights on May 2 and 3, 2008. 101
5.24 Time-averaged VHE photon spectra of Mrk 501 in 2008 103
5.25 SED of Mrk 501 obtained during the mwl campaign in March-May 2008 103
5.26 Time-averaged VERITAS and Whipple photon spectra of Mrk 501 for discrete flux levels 105
5.27 SED of Mrk 501 during the 3-weeks period in April-May 2009 . . . 106
5.28 SED of Mrk 501 during the 3-weeks period in April-May 2009 with the SSC model fit. 107

List of Tables

3.1 The Hillas parameters definition 46

4.1 Optimized cuts for season 2008-09. 62

5.1 Instruments involved in the multi-wavelength campaigns of Markarian 421 and Markarian 501 during 2007-2009. 76
5.2 Dataset of Markarian 421 for the multi-wavelength campaign in 2007-2008. 77
5.3 Dataset of Markarian 501 for the multi-wavelength campaign in March-May 2008. 79
5.4 Dataset of Markarian 501 for the 3-week period in 2009 mwl campaign. 81
5.5 Best-fit parameters for VERITAS data. 102
5.6 Best-fit parameters for VHE data. 102
5.7 The SSC model parameters used to describe the broadband SED for different flux states observed during the campaign. 104
5.8 Best-fit parameters for VHE data of Mrk 501 in 2008. 105
5.9 SED model parameters of Mrk 501 in 2009. 108

Chapter 1

Introduction

1.1 General Contents

The last twenty years were marked by a rapid development in the field of ground-based very-high-energy (VHE) gamma-ray astronomy. In 1989, the first confirmed source of VHE γ-rays was detected. At that time, there was only one observatory (Whipple 10 m telescope) with a low enough energy threshold and sensitivity to detect VHE gamma-rays. Nowadays, the total number of detected sources exceeds 130, and four major third-generation ground-based observatories are currently operational. However, the physical processes involved in VHE emission are still not well understood and far from being resolved. Several leptonic and hadronic models have been tested so far trying to explain the radiative mechanisms, but the observations do not yet sufficiently constrain them.

The aim of this work is the study of the very-high-energy gamma-ray emission coming from two well-known gamma-ray blazars, Markarian 421 (Mrk 421) and Markarian 501 (Mrk 501), using observations from the Whipple 10 m telescope and the Very Energetic Radiation Imaging Telescope Array System (VERITAS). The combination of these observations with other experiments and searching for variability and correlation between different energy bands can improve our knowledge of blazar physics, such as the physical processes involved in VHE emission. A contribution to the general problem of VHE gamma-ray emission is made from the observational point of view, focusing on the problem of the non-thermal radiation production for extragalactic sources. Due to the complexity of the spectral energy distribution (SED) of these kind of sources, multi-wavelength (mwl) observations were used to complement the VHE observations. In particular, during the 2007-2009 observing seasons, some intensive coordinated mwl campaigns were conducted on both sources. The Whipple 10 m telescope was dedicated to monitoring them for the entired period. As a results an amazing temporal and spectral coverage in the VHE γ-ray, X-ray, optical and radio bands was obtained. In this thesis, results from the analysis of VHE observations with Whipple and VERITAS are presented as well as the analysis of time series, correlations, and model fitting for the observed spectral energy distribution.

In this chapter a brief description of gamma-ray astronomy is introduced as

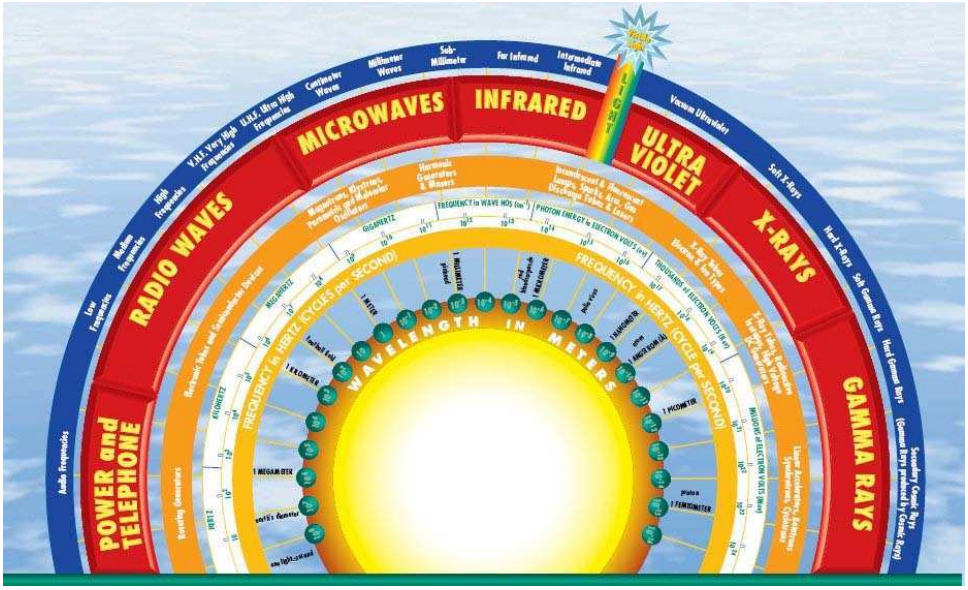

Figure 1.1: Wavelengths and energy bands for photons in the electromagnetic spectrum are shown. Plot taken from http://hacastronomy.com

well as the different types of astrophysical sources that are capable of producing gamma-rays, focusing on blazars. This class of object is the most common one in the TeV sky. In order to understand what blazars are and how they can emit such energetic radiation, the general class of active galactic nuclei must first be introduced. Then, after a general discussion about blazars, the main characteristics of Markarian 421 and Markarian 501, the two blazars that are the main focus of this study, are described. In Chapter 2, current satellite observatories and telescopes, from radio to high-energy γ-rays, and their performance are introduced. In Chapter 3, the instrumentation techniques of gamma-ray observatories are described. The spectral reconstruction of gamma-ray data is described in Chapter 4, together with the calibration techniques employed at the Whipple 10 m. In Chapter 5, the results of the multi-wavelength campaigns of Mrk 421 and Mrk 501 during the 2007-2009 seasons are presented. A variability and correlation analysis and an observed SED during those campaigns are presented as well in this chapter. Final remarks, conclusions and the future prospects for gamma-ray astronomy are discussed in Chapter 6.

1.2 Gamma rays

Gamma-rays occupy the most energetic part of the electromagnetic spectrum with more than 14 orders of magnitude in energy (see Figure 1.1) ranging from 10^6 eV to 10^{20} eV. They are produced by the hottest and most energetic objects in the universe, such as neutron stars and pulsars, supernova explosions, and regions around super massive black holes.

It is necessary to classify gamma-rays into smaller energy ranges of similar

behavior and detection techniques. The division has been historically defined in four bands: the high-energy (HE) band for energies between 30 MeV and 10 GeV, the very-high-energy (VHE) band for energies ranging from 10 GeV to 100 TeV, the ultra-high-energy (UHE) band for energies between 100 TeV and 100 PeV and the extremely-high-energy (EHE) band between 100 PeV and 100 EeV. Recently, the VHE band has changed a little, been accepted now as starting at 100 GeV, which is the point that separates space- and ground-based detectors.

VHE gamma-rays are messengers of violent, non-thermal processes that do not follow a Maxwell distribution, happening at the location of the source or very close to it.

In order to produce gamma-rays, electrons, positrons, protons, or heavier nuclei must be accelerated to very-high energies. The particles then produce electromagnetic radiation, known as gamma-rays which travels through space attenuated by its interaction with low energy photons from the interstellar medium and from the cosmic microwave background. There are several relevant emission mechanisms: Synchrotron radiation is emitted when a relativistic charged particle spirals around a magnetic field line. To generate VHE photons by this mechanism, either strong magnetic fields ($\gg 1$ G) or extremely high-energy electrons or protons are required. Another process is Bremsstrahlung, which occurs when an electron is decelerated by the electromagnetic field of a heavier charged particle or particles. The "braking radiation" produced is a result of the energy loss by the electron, which can be quite substantial. Perhaps the most important process is Inverse-Compton scattering (IC). When a low-energy photon collides with an energetic electron, the photon can be scattered to much higher energies. More information about gamma-ray emission processes can be found elsewhere (e.g. Aharonian 2004, Longair 1992).

Gamma-rays can be detected through their interaction with matter and different energy ranges lend themselves to different dominant interaction processes. For higher-energy photons, the dominant process is pair production. If the gamma-ray photon has energy:

$$h\nu \; > \; 2m_0 \, c^2 \; = \; 1.022 \text{ MeV} \tag{1.1}$$

where m_0 is the rest mass of the electron, it can convert to an electron-positron pair in the presence of an atomic nucleus, required for momentum conservation.

VHE gamma-rays interact with the Earth's atmosphere producing Cherenkov light that may be collected by a suitable detector. More details can be found in Chapter 3.

1.3 Gamma-ray Astronomy

The field of the VHE gamma-rays astronomy resulted from the extension, upwards in energy, of observations that were performed by satellites back in the 1960s, and the study of cosmic-rays, in which the detection of cosmic photons above 1 TeV with ground based instruments was pursued. As VHE observations are at the high end of the observable electromagnetic spectrum, there has been much

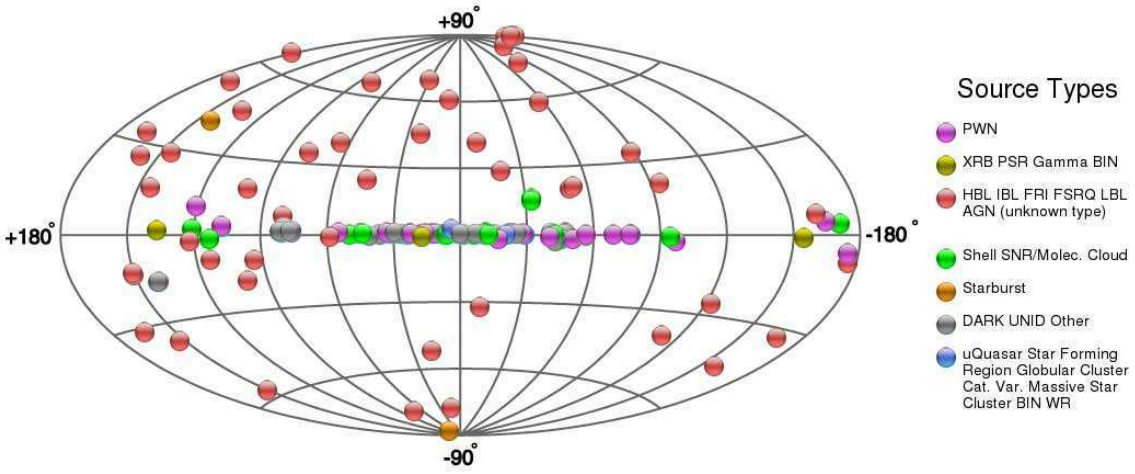

Figure 1.2: Sky map of the TeV observation. The statistics are up to November 2011. The plot is taken from http://tevcat.uchicago.edu.

difficulty in identifying sources of VHE gamma-rays. However, the development of the atmospheric Cherenkov imaging technique allowed the detection of the first source of TeV photons, the Crab Nebula about 22 years ago (Weekes et al. 1989). The detection of TeV gamma-ray sources in the past decade came as a result of great advances in the ground-based detection technique (Weekes et al. 2003). Since then, the discovery of multiple sources has allowed the field to become a very important astronomical discipline, by detecting new VHE sources, Galactic and Extragalactic, characterizing them by the study of their fluxes, which are in some cases steady and in some others variable, and the study of their spectral energy distributions. In the past few years, the third generation of very-high-energy gamma-ray observatories has started to become fully operational which is resulting in a major increase in the number of TeV sources (see Figure 1.2), reaching 130 sources by November 2011.

VHE gamma-ray astronomy can provide insights into a number of scientific areas. The origin of cosmic rays has been unknown since their discovery in 1912, as their trajectories are bent in the Galactic magnetic field. However, gamma-rays do not modify their trajectories in the Galactic magnetic field, so, they have the advantage to be traced back to their sources, through their incoming directions. Gamma-rays are expected to be produced in the same areas as the sources of cosmic rays. Thus, observations of VHE gamma-rays can possibly provide some light for the nature of cosmic-particle acceleration mechanisms, providing some constrains on the models, ultimately increasing the understanding of the underlying phenomena.

Gamma-ray bursts (GRBs) were discovered in 1969 (Klebesadel et al. 1973) by US satellites looking for Soviet nuclear tests. Since then, they have remained one of the greatest mysteries of astronomy. They have been well studied at all wavelengths, from radio to HE gamma-ray (with *Fermi* since 2008). The very-high-energy band is the only energy regime in which definitive evidence for GRB

emission has still to be found. For the observation of photons with energies above 100 GeV, only ground-based telescopes are available.

Most of the GRBs last 2 seconds or longer (known as *long and soft* GRBs) and the rest, lasting less than 2 seconds are known as *short and hard* GRBs. The *long* GRBs are followed by a strong afterglow at lower energy with long lasting emission in the X-ray, optical and radio. Most of the afterglows have been studied thoroughly in the past few years, and this kind of GRBs (long) are associated with core-collapse Supernovae or explosions of massive stars in distant star-forming galaxies (e.g. Hjorth et al. 2003, Woosley & Bloom 2006). The observation of optical counterparts of GRBs has lead some people to conclude that there is a population of electrons producing synchrotron radiation and being able to scatter some MeV photons via Inverse Compton scattering to produce TeV gamma-rays (Beloborodov 2004). The *short* GRBs are more difficult to study because they last at most a couple of seconds and there is no afterglow present in the X-rays or visible light. However the X-ray satellite *Swift* has been dedicated to detect short GRBs since it was launched in 2004. Now, the probable origin of the short GRBs has been revealed as a merger between neutron stars of a binary system and the instantaneous production of a black hole (e.g. Piran 2004).

The current most popular model is the "fireball" model which describes GRBs as the core-collapse of massive stars or the coalescence of two compact objects. Since GRBs are transient sources, the gamma-ray flashes usually last a very short time. Gamma-ray bursts can appear from any direction without warning and may last only from a few milliseconds to over a thousand seconds. Despite the time duration, they are the brightest gamma-ray phenomena known, outshining all other sources of gamma rays combined.

Clusters of galaxies are the biggest gravitationally bound systems in the Universe. The prediction of their TeV emission is based on the interactions of accelerated protons with the ambient gas. In the case of gamma-rays produced by the interactions of multi-TeV electrons with the CMB, the unknown strength of the inter-cluster magnetic fields makes the flux prediction suffer huge uncertainties. So far, one source have been observed: the Perseus cluster, observed by H.E.S.S. (High Energy Stereoscopic System) and only upper limits have been derived.

Another possibility is the detection of the decay of massive relic particles from the early universe that have clustered within the Galactic halo (Protheroe & Stanev 1996). Dark matter (DM) mysterious and exotic particles searches have made the gamma-ray field even more interesting. Evidence of the existence of DM comes from astrophysical observations, in which 20 % of the mass density in the universe are baryons and the rest remains as an enigma. In some particular sources like dwarf galaxies, huge amounts of DM are believed to exist. It is very hard to identify these exotic signals with the current generation of Cherenkov telescopes. Nevertheless, these sources have a high potential for detection of DM signal.

While it is possible that the Large Hadron Collider (LHC) will provide evidence for super-symmetry, gamma-ray observations provide the only avenue for measuring dark matter halo profiles and looking for the role of dark matter in structure formation. Gamma-ray observations are complementary to the LCH accelerator and direct searches. The LHC will only probe neutralino masses of about 600 GeV,

above this energy, ground-based gamma-ray instruments and direct detection experiments are sensitive. Although, the IceCube Observatory recently show that can measured neutralino masses of about 330 GeV (Abbasi et al. 2011).

The study of exotic objects is another motivation for VHE gamma-ray astronomy. Most of the sources detected at TeV energies contain compact objects such as black holes and neutron stars. In addition, there are many speculative objects, such as cosmic strings and primordial black holes that may produce TeV photons. VHE gamma-ray astronomy can provide a further insight into the known as well as the speculative phenomena. Finally, the study of photon propagation through the intergalactic medium is addressed by VHE gamma-ray astronomy. Observations of TeV sources can provide a direct measurement of the density of the infrared component of the extragalactic diffuse photon background which is currently unknown.

Since the detection of the first TeV gamma-ray source by the Whipple Telescope in 1989, more than 20 years later, over a hundred of sources have been detected as can be seen in Figure 1.2, with only six types of objects: Active Galactic Nuclei (AGN), Supernova Remnants (SNRs), Pulsar Wind Nebulae (PWNe), binary systems, young star clusters and starburst galaxies.

All the extragalactic sources detected at the VHE band are AGNs except for the two starburst galaxies M82 and NGC 253 discovered in 2009 by VERITAS (Acciari et al. 2009) and H.E.S.S. (Acero et al. 2009) collaborations. The starburst galaxies are galaxies containing regions of intense star formation, and due to that, they can help to answer the century old question of the origin of cosmic rays.

Most of the discovered AGNs sources are blazars and only 3 AGNs are radio galaxies FR1 (NGC 1275, M87 and CenA). The radio galaxies are low-luminosity, radio-loud AGNs with their jets oriented at an angle greater than $\sim 20^\circ$ from the line of sight. The different types of AGNs are explained in detail in section 1.4.

The galactic sources detected at the VHE band are quite different. The first type of source detected at VHE was the Crab Nebula, which became the standard candle (see section 1.3.1). This source is a Pulsar Wind Nebula (PWNe) in which a supernova remnant (SNR) surrounds a rapidly rotating pulsar and interacts with the pulsar wind, producing non-thermal emission. In several cases, it was found that the emission comes directly from the shell of the remnant itself without the presence of a pulsar interacting with the interstellar medium. Another class of Galactic TeV emitters are X-ray binaries. These systems are composed of a compact object (black hole or neutron star) and a stellar companion. There are six members of X-rays binaries detected at VHE band (LSI+61 303, VelaX-1, CentaurusX3, PSR B1259-63, LS 5039 and CygnusX-1). The last type of galactic TeV source are young star clusters. Four young star clusters were detected at TeV energies: Westerlund 1 (Abramowski et al. 2012), Westerlund 2 (Aharonian et al. 2007a), HESS J11614-518 (Aharonian et al. 2005) and HESS J1848-018 (Chaves et al. 2008). These objects are populated by massive stars, including Wolf-Rayet stars and the emission process is still unclear and might be explained by shocks between the winds from massive stars.

Several Galactic TeV sources are still unidentified having no distinguishable counterpart at other wavelengths. Trying to look at the counterpart of uniden-

tified sources at HE and VHE gamma-ray energies is of great interest for the astronomical community. Thus, the classes of objects emitting at VHE will certainly increase in the future.

1.3.1 Standard Candle: Crab Nebula

The Crab Nebula is a PWN system that is located in the constellation of Taurus, 6.500 light-years away from the Earth, being one of the most studied objects in the sky. It was first observed by Chinese astronomers in the early 1000s and rediscovered by the English astronomer John Bevis in 1791. The name "Crab Nebula" was given in the 1850s by William Parson. It was the first object discovered as a SNR, the first SNR connected to a pulsar, and the first pulsar observed at optical, X-rays and γ-rays wavelengths. It was also the first source discovered at VHE in 1989 (Weekes et al. 1989) and which opened the VHE γ-ray astronomy field. It remains as a very important object in VHE astrophysics and has become the standard candle at TeV energies due to its super-steady flux during all these decades. This steady flux allows the TeV telescopes to study its emission and use it in order to calibrate observations of other variable sources and to cross check simulations. Figure 1.3 shows multi-wavelength images of the Crab Nebula.

VERITAS measured a differential spectrum for the Crab Nebula TeV range which obeys a power law of the form:

$$dN/dE \;=\; F_0\;(E/Eo)^{-\Gamma}\;\;\mathrm{TeV}^{-1}\;\mathrm{cm}^{-2}\;\mathrm{s}^{-1} \tag{1.2}$$

where dN/dE is the differential flux as function of the energy, with $F_0 = (3.63 \pm 0.15_{stat}) \times 10^{-11}$ a normalization index and $\Gamma = 2.54 \pm 0.05_{stat}$ a power law index. Other TeV telescopes report comparable values (Aharonian et al. 2006, Otte et al. 2007). Figure 1.4 shows the archival SED for the Crab Nebula taken with several instruments. The two characteristic bumps that reveal the γ-ray emission can be seen. It is believed that the lower energy peak, usually from radio to UV or soft X-rays, is due to synchrotron radiation emitted by the electrons moving ultra-relativistically in the jet, while the higher energy peak, from X-rays to gamma-rays, has an origin which is still unknown, presumably by Inverse-Compton of accelerated electrons (more details in section 1.4.1).

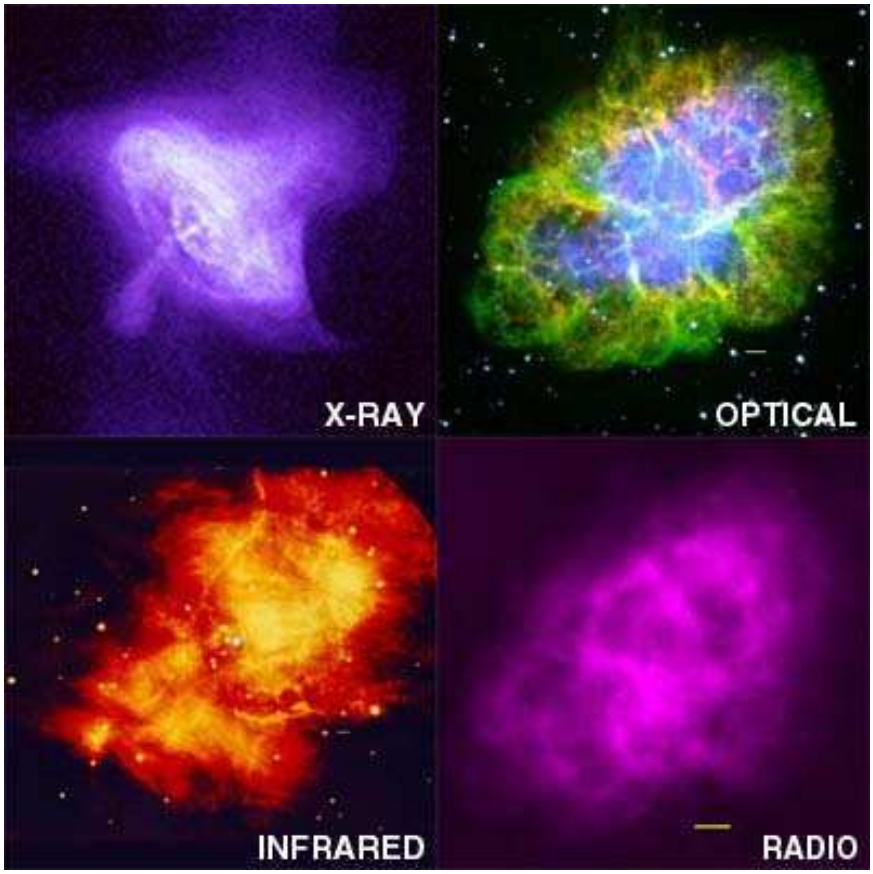

Figure 1.3: Multi-wavelength images of the Crab Nebula at X-ray (Chandra), optical (Palomar), infrared (Keck), and radio (VLA) wavelengths.

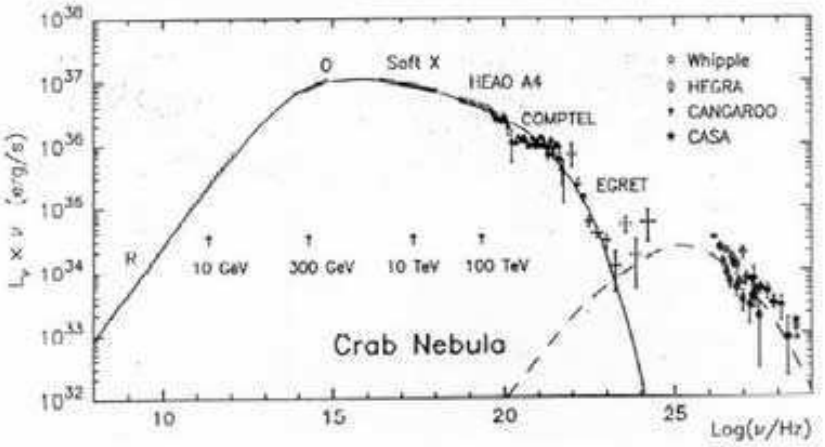

Figure 1.4: SED of the Crab Nebula with a theoretical curve for a leptonic-hadronic model (Image taken from: http://ihp-lx.ethz.ch/CompMethPP/magic/magicIntro.html).

1.4 AGN: Blazars

Active Galactic Nuclei (AGN) are galaxies whose central cores are believed to be super massive black holes ($10^6 - 10^{10}$ solar masses) surrounded by bright accretion

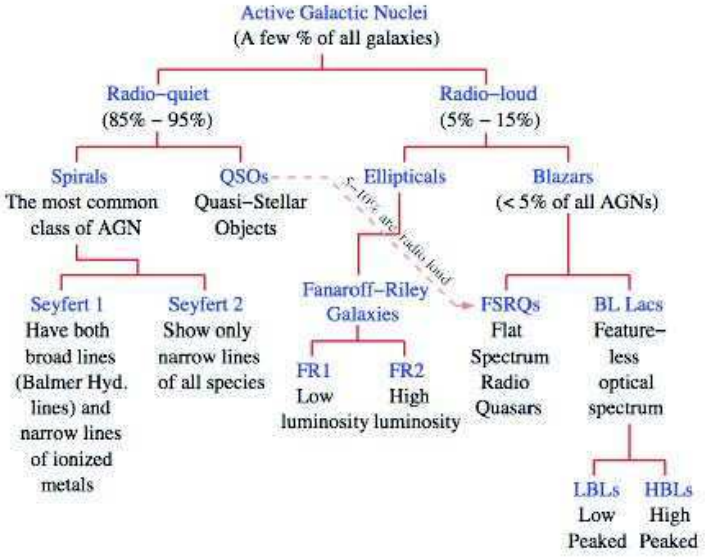

Figure 1.5: AGN classification scheme. Figure from Errando (2009), based on Urry et al. (1995).

disks. Based on the observed phenomenology, AGN have historically been divided into different subgroups, which in the past were empirically discerned by their radio emission, the properties of their optical emission lines, morphological considerations and other properties (see Figure 1.5). Today, one of the classification relies on the viewing angle of the jet under which the AGN is observed (see Figure 1.6).

Blazars are an AGN subclass in which the viewing angle of the jet is very small ($< 10°$), such that the observer is looking straight down the jet. Blazars exhibit strong, rapid and irregular variability over the entire electromagnetic spectrum. Episodes of high variability are produced in a compact zone of the system, most probably in the relativistic jet. The mechanisms responsible for this variability are the motivation for the study performed in this work. Blazars provide us the unique opportunity to observe the properties of these processes occurring within the jets, and particularly, the determination of the types of accelerated particles. Acceleration processes in these jets generate non-thermal emission over an energy range from radio to VHE γ-rays.

Blazars are traditionally divided into two subclasses: Flat Spectrum Radio Quasars (FSRQ), that display emission lines, and BL Lac objects (BL Lacs), that display a lack of emission lines. It has been suggested that this subclassification of blazars into FSRQs and BL Lacs is merely a selection effect and that emission line luminosities of blazars are actually a continuous function (Scarpa & Falomo 1997). BL Lac objects are classified as HBL, IBL or LBL (where the first letter stands for High-, Intermediate- and Low-peaked) depending on the position of the lower energy bump in the spectral energy distribution (see section 1.4.1). The classification into LBL and HBL was introduced by Fossati et al. (1998) suggesting

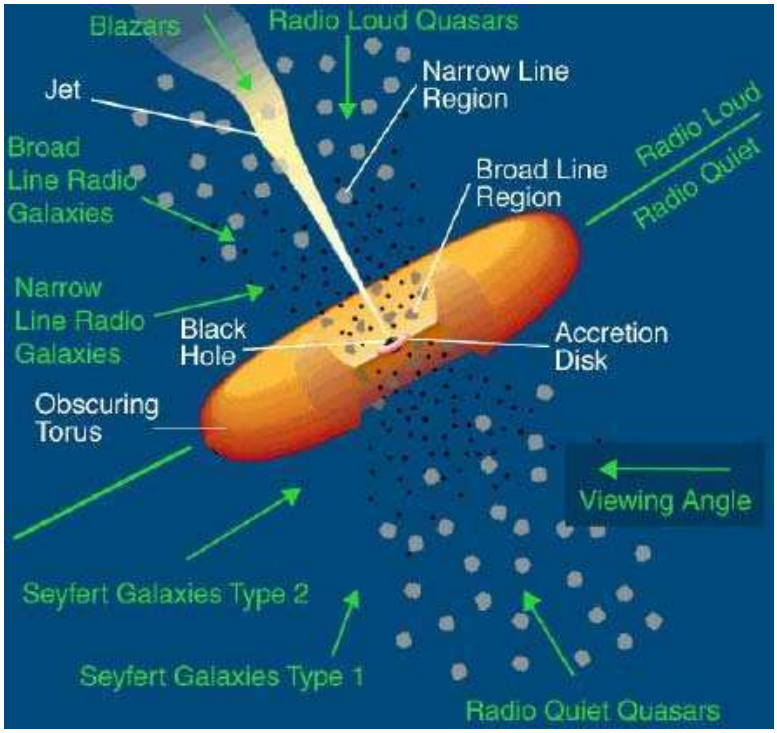

Figure 1.6: The unified AGN model based on orientation of viewing angle.

a continuous spectral sequence within the blazar family rather than separated spectral classes. LBLs have their first peak in the infrared-optical band and the second one at keV-MeV energies. In LBLs, the high energy component dominates over the low energy one. On the other hand, in HBLs, the first peak is found at UV-X-ray frequencies and dominates over the high-energy component, which peaks at GeV-TeV energies. IBLs lie between both. It is widely believed that the relativistic jet is the key element of blazar emission. In order to explain the observed broad-band spectrum most models assume that a relativistic population of particles (electrons, protons or both) is accelerated within the jet. The relativistic beaming plays a very important role in the emission properties of these objects.

The large majority of the established TeV-emitting AGNs belongs to the blazar class, with the subclass of HBL playing an important role. The IBL WComae and the LBL BL Lac represent the remaining minority. In Figure 1.7 an updated map of the extragalactic detected sources is provided. In total, there are 29 HBLs, 4 IBLs, 4 LBLs and 2 AGNs of unknown type.

1.4.1 Blazar Spectral Energy Distribution and Emission Models

The blazar spectral energy distribution has a double peak structure when is plotted as $\nu\ F_\nu$ which is an indication of the emission power. Both peaks are found to vary as the activity of the blazar changes (see Figure 1.8). Several models have

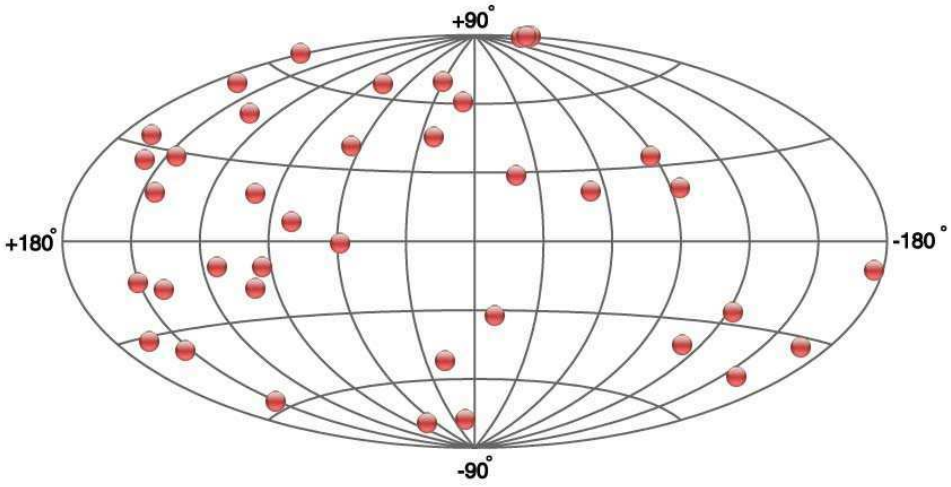

Figure 1.7: Sky map of the TeV extragalactic sources. Plot from http://tevcat.uchicago.edu.

been developed to explain the double peak structure, in which the first peak at keV energies is referred to as the synchrotron peak due to the synchrotron emission from relativistic electrons and positrons that are present in the jet. The VHE peak is not well understood, and there are different models to explain the emission process. Leptonic models assume that synchrotron photons are up-scattered to higher energies by the accelerated electrons (Synchrotron-Self-Compton, SSC, model), whereas in External Inverse Compton (EIC) models, these seed photons can come from the accretion disk, the broad-line region, the torus, the local infrared background, the local microwave background, the ambient photons from the central accretion flow or from some combination of these sources (e.g. Dermer et al. 1992, Maraschi et al. 1992, Marscher & Gear 1985, Sikora et al. 1994).

Some hadronic models propose that the emission from X-ray to γ-rays is synchrotron radiation from protons that are accelerated in highly magnetized compact regions of the jet (Aharonian 2000), by proton-proton collisions, either within the jet itself or between the jet and ambient clouds (Beall & Bednarek 1999, Dar & Laor 1997, Pohl & Schlickeiser 2000).

Blazars present outbursts in the X-ray and VHE γ-ray bands. These flares have been observed over a large range of time scales from months to less than an hour. The observed flares may be caused either by internal shock waves within the jet (Rees 1978, Spada et al. 2001) or the ejection of relativistic plasma (Böttcher et al. 1997, Mastichiadis & Kirk 1997). More recently, it has been suggested that flares may be associated with magnetic reconnection events in the jet that is dominated by the magnetic field (Lyutikov 2003). In some blazars, a strong correlation between fluxes in the X-ray and VHE γ-ray bands has been observed. This would imply that the same population of electrons is responsible for producing emission in both energy bands, via synchrotron emission and Inverse-Compton scattering.

Figure 1.9 shows the most outstanding flare observed until now from the blazar PKS 2155-304, having a well-resolved substructure on a short timescale of 200 s

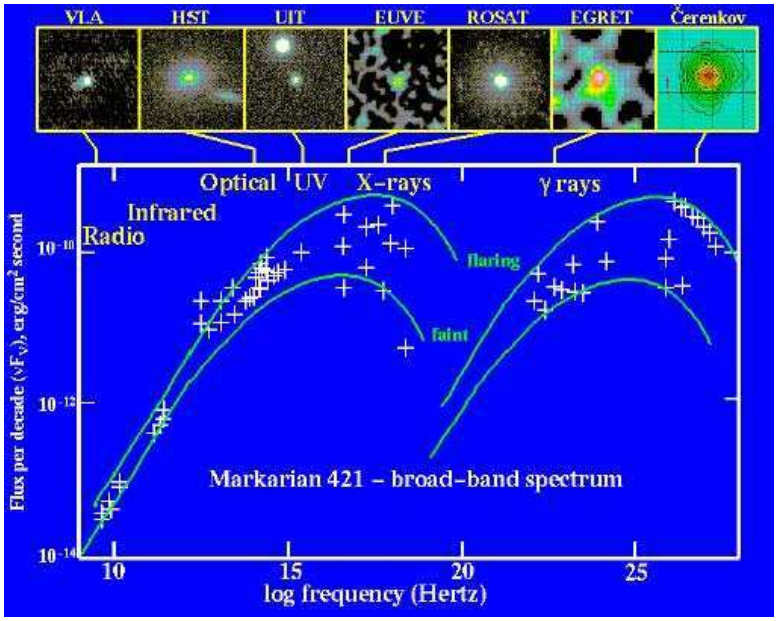

Figure 1.8: The SED of Mrk421 from radio to TeV band. Mrk421 is a HBL object, in which the two peaks are located at X-rays and γ-rays respectively. Usually, the first peak is well sampled and measured, however, the high energy peak usually has a lot of uncertainties.

(Aharonian et al. 2007b). Such rapid variability has implications regarding the size of the emitting region. In the presence of beaming, observed time intervals may be much shorter than those occurring in the rest frame of the source. This extremely short variability implies a more compact (smaller than the central black hole size) or more violent (with a Doppler factor $\delta >> 10$, and a Lorentz factor $\Gamma \sim 50$) emission region for the TeV radiation than has been previously considered (Begelman et al. 2008, Weekes 2007).

It is essential to have long-term, well-sampled, observations of a blazar in order to understand the physical process and the emission mechanisms (Steele et al. 2007). Multi-wavelength observations of gamma-ray emitting blazars are important in order to test models of non-thermal emission from these objects. Measurements of the temporal correlation between flux variations at different wavelengths during flares are particularly useful, providing constraints on the emission models in various energy regimes (Horan et al. 2009).

The activity of the source can be analyzed through the comparison of the different light curves. From the study of the light curves, the typical variability (e.g. Vaughan et al. 2003) at different energy ranges or possible correlations in the flux variation within the different frequency bands, can be extracted (Edelson & Krolik 1988). Tools for the study of the correlation are described in Chapter 5. Focusing on the X-ray/γ-ray bands sometimes gives a precise correlation between the evolution of both emissions. This provides an excellent opportunity to test theoretical models for VHE emission of blazars (Katarzyński & Walczewska 2010), since different emission models provide different predictions regarding the relationship between the two bands and might reveal information about a common

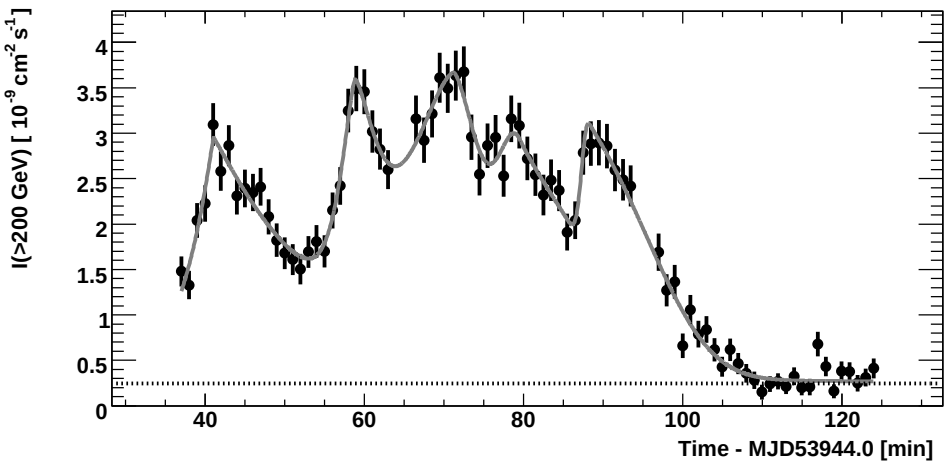

Figure 1.9: The extraordinary VHE flare observed by H.E.S.S. from PKS2155-304 in 2006 (Aharonian et al. 2007b). The maximum peak was around 15 times the Crab Nebula flux and shows a short variability over a few minutes.

population.

Leptonic Models

The SSC Model

The most successful model that explains the TeV emission from blazars is the SSC model. It assumes that both the X-ray and the VHE gamma-ray emissions originate in the relativistic jets due to the synchrotron radiation and IC scattering of the same population of high energy electrons. In the simplest case, i.e. in the one-zone homogeneous SSC model, the seed photons for the IC scattering are assumed to be synchrotron photons produced in the same emission region within the jet. The emission region has a characteristic size R, moving at a relativistic speed $\beta = v/c$, with an angle θ to the observer's line of sight. In the co-moving frame of the source, the distributions of hot electrons and photons are isotropic and homogeneous. The observed SED of TeV-emitting blazars is characterized by two broad peaks, as has been mentioned above. At both sides of the peaks, the spectrum may be described by two different power law indices, Γ_1 and Γ_2. However, the spectrum on the right hand side of the peak (the highest energy regime) is still poorly known and may be affected by intergalactic absorption. In order to fulfill the observed curved spectral shape, the relativistic electron spectrum is required to steepen with increasing energy (Holland et al. 2008). With the above assumptions, there are seven parameters needed to fully describe the model. They are the magnetic field intensity B, the size of the emission region R, the Doppler factor δ, the slopes of the electron spectrum (Γ_1 and Γ_2), the Lorentz factor of the electrons at the break energy γ_b, and the electron density parameter K (Tavecchio et al. 1998).

From the multi-wavelength data, there are several parameters which can be derived from observations. They are the photon index of the synchrotron radia-

tion before the break, Γ_1, the photon index of the synchrotron radiation after the break, Γ_2, the synchrotron frequency at the peak, ν_s, the frequency of IC peak, ν_c, the total measured energy flux of the synchrotron component, Ls, and the total measured energy flux of the IC component, Lc.

EIC Model

In some cases, the SSC model cannot satisfactorily explain the observed SED (e.g. Senturk et al. 2011). For instance, the number of seed photons from the synchrotron radiation of high energy electrons does not sufficiently explain the huge amount of luminosity of the observed IC peak. Therefore, the addition of extra seed photons might be necessary. A possible additional source of the seed photons are ambient infrared or optical photons, cosmic microwave background, or thermal radiation photons. The thermal photons may come from the accretion disk or from scattered photons from surrounding clouds. All these sources are outside the jet, thus this model is called External Inverse Compton model.

Hadronic Models

The hadronic models assume that there are high-energy protons being accelerated together with electrons inside the jet. They explain the observed gamma-ray emission as being initiated by accelerated protons interacting with ambient matter (Pohl & Schlickeiser 2000), photon fields (Mannheim 1993), magnetic fields (Aharonian & Atoyan 2000), or both magnetic and photon fields (Mucke & Protheroe 2001). In these models, protons need to be accelerated to very high energies ($\geq 10^{18}$ eV), otherwise, they cannot provide enough γ-rays inside the jets. Particularly in the proton synchrotron and proton-radiation interaction models, protons have to be accelerated close to 10^{20} eV (Atoyan & Dermer 2003). Also, in order to make the proton synchrotron radiation an effective mechanism for γ-ray production, a strong magnetic field close to 100 G inside the jet is required. Although, it is not known how those protons are accelerated up to such high energies, particles with such high energies can be seen in ultra-high energy cosmic rays. The low energy peak of the SED in this scenario is explained by the synchrotron radiation of the co-accelerated electrons, since the proton synchrotron radiation will not be as efficient as for electrons. If the proton acceleration takes place at a very high rate, for a typical Doppler factor $\delta \geq 10$, the proton synchrotron radiation would fit well into the TeV regime. Also, this process allows very hard intrinsic γ-ray spectra, giving a reasonable explanation for the stable spectral shape of the TeV emission observed during the strong flare of Mrk 501 in 1997 (Aharonian & Atoyan 2000). The challenge of hadronic models is to explain the variability correlation of the X-ray and VHE gamma-ray observations. In the proton synchrotron model, the synchrotron peak at X-rays is explained by the counter components of UHE protons in the jets, i.e. electrons. Synchrotron photons are generated by the electrons but at different places from the VHE photon production region by protons. However, there is another possibility of the synchrotron radiation, coming from secondary electrons produced by interactions of the primary VHE γ-rays with the ambient low frequency radiation. In this scenario, tight correlation between X-

rays and VHE γ-rays photons are expected, because these secondary electrons are immediately cooled down in the strong magnetic field. Nevertheless, if the magnetic field outside the emission region (blob) drops significantly, more complicated correlations cannot be excluded.

Mixed Models

In some cases, the VHE γ-ray flare of a blazar cannot be associated to any X-ray counterpart. This is called an "orphan" flare. Genuine "orphan" VHE flares cannot be easily understood either by applying SSC or hadronic models. It is interesting that the "orphan" flare may be understood in a hybrid scenario, where protons are present in the jet but they are not necessarily the dominating component compared to lepton components (Böttcher 2005). The synchrotron photons (here X-ray) are reflected back to the jet by some external clouds. The returning photons interact with the protons inside the jet producing pions and thus the resulting "orphan" VHE flaring originates from π_0 decay. This model has shown to work for the "orphan" VHE flare observed in 1ES1959+650 (Böttcher 2005).

Despite all the observations made since the first discovery of a VHE γ-ray blazar in 1992 and all the theoretical models involved, the answers of the most basic questions about blazars (such as how is the matter accelerated to VHE, how are the jets generated and collimated, what is the content of matter, electrons or protons, what is the origin of high variability, etc.) have not been found yet.

The main physics motivations for TeV long term monitoring of AGNs are the following:

- Understanding the variability and time evolution of the VHE emission.
- Observing and understanding the "orphan" flares or any variability without counterparts.
- Getting a better sampling for the different states through multi wavelength campaigns trying to find basic intrinsic differences between states.
- Studying correlations between different energy bands and constraining the emission mechanism.
- Studying the broad band spectrum of the source.
- Searching for periodicity.

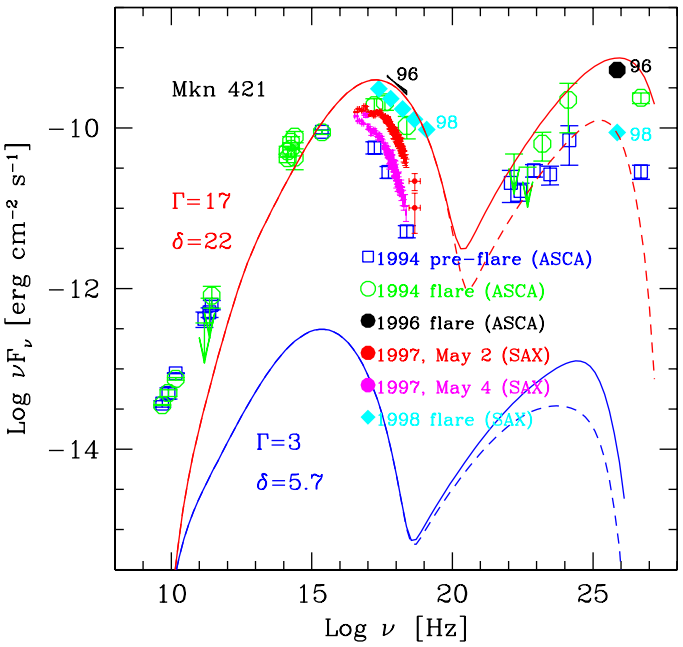

Figure 1.10: Example of SED of Mrk 421 with data from 1996-99. Figure taken from Ghisellini et al. (2005)

1.4.2 Markarian 421

Markarian 421, located in the constellation of Ursa Major at a redshift $z = 0.030$, is the closest known and best studied TeV blazar. It was the first extragalactic γ-ray source detected in the TeV band by the Whipple telescope in 1992 (Punch et al. 1992) and is the brightest blazar detected in X-rays and UV. Figure 1.10 shows the SED of Mrk 421. It ranges from radio to TeV energies.

Mrk 421 is a high-frequency-peaked BL Lac object, in which the synchrotron peak lies in the X-ray regime and the Inverse-Compton peak at GeV/TeV energies (see Figure 1.10). It has historically exhibited strong variations in both frequency peaks of the SED (Fossati et al. 2008). During 2005 and 2006, a multi-wavelength observing campaign on Mrk 421 was conducted with different instruments that were involved to cover observations of this source in the radio, optical, X-ray and γ-ray bands (Horan et al. 2009). During the past 20 years, Mrk 421 has shown a high variability from years (Acciari 2010) to hours (Acciari et al. 2011, Pichel et al. 2009) from radio to VHE gamma-ray wavelengths with several events of high states and flares, specially in X-ray and TeV bands. Also, intensive multi-wavelength campaigns were carried out many times on this source (e.g. Abdo et al. 2011b, Acciari et al. 2011).

Through the observations and the absence of absorption lines, some indications can be made. For instance, the stars are not the source of the observed light and

neither the presence of very hot gas due to the emission properties. Also, the short variability indicates that the region of bright gas is very small compared to the host galaxy and yet it emits more light than the stars in the surrounding galaxy.

1.4.3 Markarian 501

Markarian 501 (Mrk 501) is a BL Lac object with a redshift $z = 0.034$ and it was first detected by the Whipple Telescope in 1996 (Quinn et al. 1996). Early detections of Mrk 501 revealed a very low flux of TeV γ-rays at the level of about 0.5 Crab. However, in 1997, Mrk 501 exhibited an unprecedented flare in TeV γ-rays with an integral flux of up to 10 Crab (Catanese et al. 1998, Pian et al. 1998). Even though Mrk 501 is a highly variable source of VHE gamma-ray emission, it has shown less flares and changes in flux activity than Mrk 421. The shortest flux variability discovered has a rise/fall time of a few minutes (Albert et al. 2007). Such fast variability of the source is associated with sporadic changes of the flux level on much longer time scales. Mrk 501 has been the target of many multi wavelength campaigns mainly covering the object during flaring activity (e.g Abdo et al. 2011a, Acciari et al. 2011, Kranich et al. 2009, Pichel et al. 2009; 2011). Simultaneous broadband observations of blazars in a flaring state provide an excellent test of emission models. Observations of blazars at GeV and TeV energies can profile the spectral shape of the high-energy component of their emission. Figure 1.11 shows the SED of Mrk 501. It ranges from radio to TeV energies.

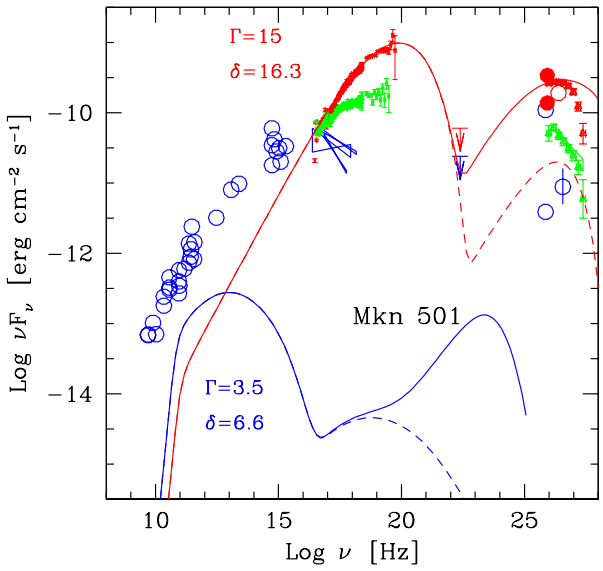

Figure 1.11: Example of SED of Mrk 501 with data from 1996-99. Figure taken from Ghisellini et al. (2005). The data correspond to the outstanding flare in 1997, taken from Djannati-Atai et al. (1999), Pian et al. (1998).

Chapter 2

Multi-Wavelength Observations

As pointed out in Chapter 1, it is necessary to have long-term, well-sampled observations of a blazar in order to understand the involved physical processes and emission mechanisms, and to test different emission models. Also, studying the temporal correlation between flux variations at different wavelengths during different time scales may provide constraints on the emission models. As the Earth's atmosphere is transparent to optical and radio wavebands and opaque to X-rays and γ-rays, using different techniques is essential to detect radiation for each energy band in order to discover the outstanding universe and its features across the electromagnetic spectrum.

This chapter is focused on presenting observational features related to several facilities used for the multi-wavelength campaigns of Markarian 421 and Markarian 501 from 2007 to 2009.

2.1 X-rays

X-ray astronomy began in the 1960s with rocket experiments, and since then all major X-ray observatories have been satellite-based. Particularly, the study of the broadband emission of blazars, with strong emission in X-rays, would not be possible without the development of X-ray astronomy. This section discusses X-ray astronomy and describes the hardware specifications and analysis techniques used by the observatories considered in this work: the telescopes on *Swift* (Gehrels et al. 2004) and the RXTE, Rossi X-ray Timing Explorer (Swank 1994) satellites. X-ray analysis and results are detailed in Chapter 5.

2.1.1 *Swift*

Swift is a first-of-its-kind multi-wavelength observatory dedicated to the study of GRBs by measuring their fluxes, spectra and light curves (see Figure 2.1). It was launched in 2004 and has three instruments: a Burst Alert Telescope (BAT), an Ultraviolet-Optical Telescope (UVOT) and an X-ray Telescope (XRT), working together to observe GRBs and afterglows in the gamma-ray, X-ray, ultraviolet, and optical wavebands. The three instruments are combined to make a powerful multi-

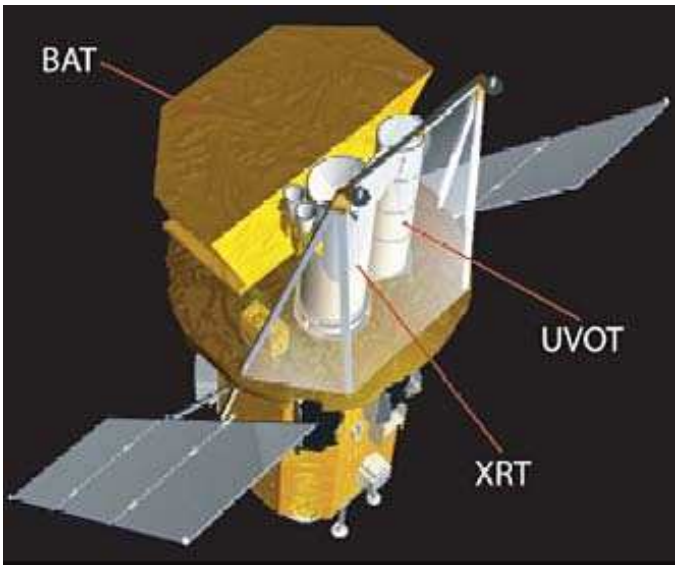

Figure 2.1: The Swift artistic impression with the three instruments. Drawing courtesy of NASA.

wavelength observatory with the capability of rapid position determinations of GRBs to arcsecond accuracy within 1-2 minutes of their discovery. Upon discovery, an alert is sent to the astronomical community to continue the effort observing the afterglows at other wavelengths. Also, *Swift* provides multi-wavelength light curves during the afterglow, a gamma-ray spectrum of the burst, X-ray spectra of the afterglow and some constrains on the redshift. All the data of *Swift* measurements are available to the astronomical community within a few hours of the observation.

Target of opportunity requests may be made once a year to follow up several sources like blazars. This request does not affect *Swift*'s capability for GRB detection, and offers the *Swift* capabilities, using more than one instrument at different wavelengths.

BAT is a large field-of-view (FOV; 1.4 steradians) X-ray telescope with imaging capabilities in the energy range from 15 - 150 keV (Gehrels et al. 2004, Krimm 2008a;b). BAT first detects the GRB and localizes the burst direction to an accuracy of 1-4 arcmin within 20 sec of the beginning of the event, which is used to slew the spacecraft to point the other two instruments (XRT and UVOT) for follow-up observations. While observing bursts, BAT simultaneously and automatically accumulates an all-sky hard X-ray survey, observing 50 % to 80 % of the sky each day. After 58 months of observations in the hard X-ray band, around 1092 sources (Baumgartner et al. 2010) were detected. Figure 2.2 shows the sky map with the BAT 58-month survey including a source classification; whereas most of the sources continue being AGNs, with a surprising number of new Type I Seyfert galaxies and high luminosity quasars.

The X-ray telescope on board of the *Swift* satellite (Gehrels et al. 2004) is a focusing, sensitive, autonomous X-ray telescope with a CCD imaging spectrometer at the focal plane of a 3.5 m focal length, a 110 cm^2 effective area and a 23.6 $\times$

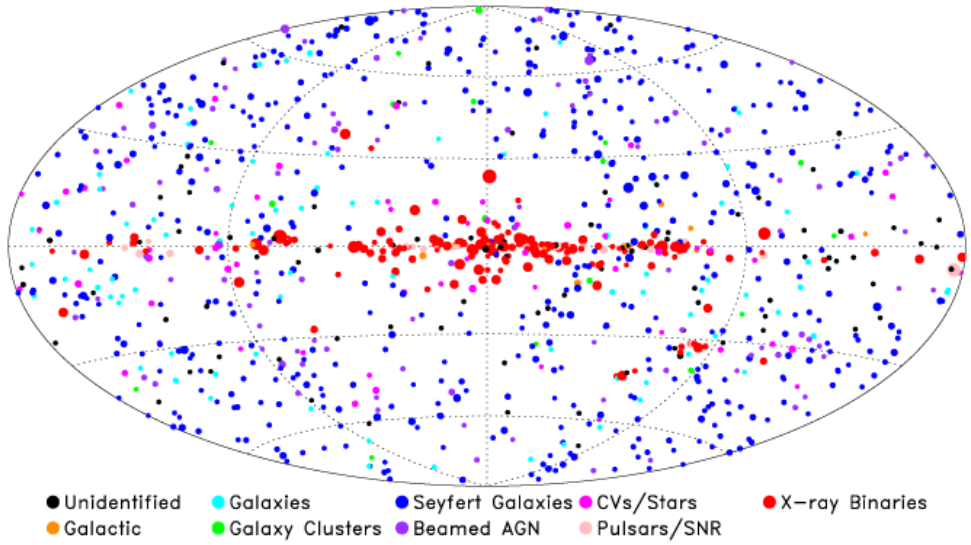

Figure 2.2: *Swift*-BAT 58-month all sky monitor survey. Figure taken from Baumgartner et al. (2010).

23.6 arcmin field of view (Burrows et al. 2005). It is sensitive to X-rays in the 0.2-10 keV energy range. The XRT is required to measure the afterglow position with an accuracy better than 5 arcseconds within 100 s of a burst alert from the BAT instrument.

UVOT makes *Swift* a complete multi-wavelength facility. It has a 30 cm aperture Ritchey-Chretien telescope and 6 bandpass filters operating over a range of 170-650 nm, as well as two grisms. The FOV is 17×17 arcmin^2 with a sensitivity of B=24 magnitude in a 1000-sec exposure. It can center sources to an accuracy of 0.3 arcsec. UVOT provides simultaneous ultraviolet and optical coverage (170-650 nm) and is a powerful complement to other instruments because of its UV capabilities and the absence of atmospheric extinction, refraction and background. Since UVOT has photon counting detectors, which are able to retain individual photon positions and timing information, its operation is similar to typical X-ray telescopes rather than to typical optical telescopes. The details of the UVOT are described in Roming et al. (2004) and Gehrels et al. (2004). The XRT and UVOT are co-aligned and pointed near the center of the BAT FOV.

2.1.2 RXTE

RXTE was launched on December 1995 (see Figure 2.3 and 2.4). It was originally designed for a lifetime from two to five years, however, RXTE is still functional. RXTE was designed to study the time variability in the emission of X-ray sources with moderate spectral resolution. The mission carries two pointed instruments: the Proportional Counter Array (PCA) which is formed by 5 proportional counters units (PCU) detectors covering the lower energy range (between 2 and 60 keV), with an energy resolution of ∼18 % and total effective area of 5200 cm^2 at 6 keV; and the High Energy X-ray Timing Experiment (HEXTE), that operates at high

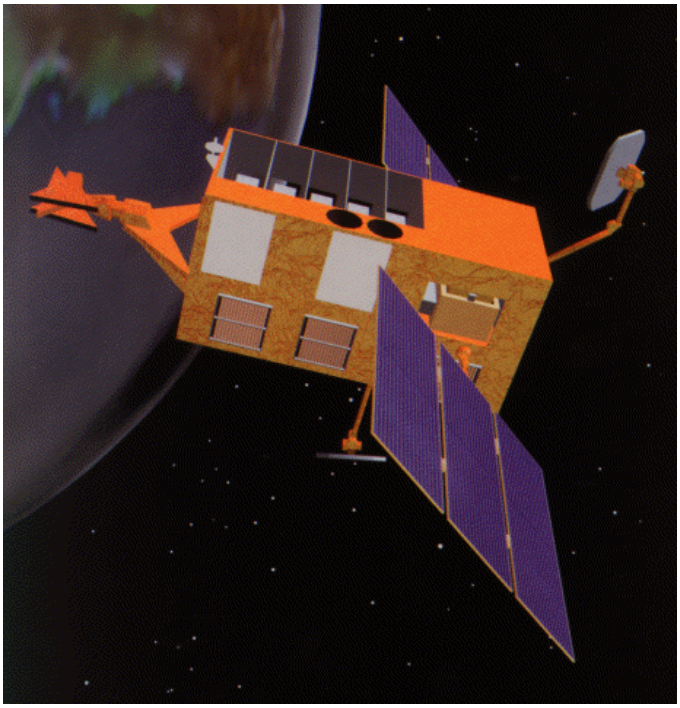

Figure 2.3: Rossi X-ray Timing Explorer. Drawing courtesy of NASA.

energies (from 20 to 200 keV) with an energy resolution of 15 % but with much lower sensitivity than PCA. Both instruments are equipped with collimators yielding one degree of field of view. In addition, RXTE carries an All-Sky Monitor (ASM) (Levine et al. 1996) that scans about 80 % of the sky in every orbit, allowing a monitoring over time scales of 90 minutes or longer, providing long-term X-ray rate monitoring over ∼350 sources in the energy band from 2 to 12 keV. X-ray point sources are identified in the wide 6 degree by 90 degree ASM field of view by shadow patterns in the slit masked detector. The systematic uncertainties in the ASM rate are 5 %, and only estimated relative fluxes are available for long (month time-scale) monitoring. The data used in this work were obtained from the public MIT archive in the form of 1-day averaged binning, as well as the dwell-by-dwell binning (for the short-term light curve and flux correlation studies).

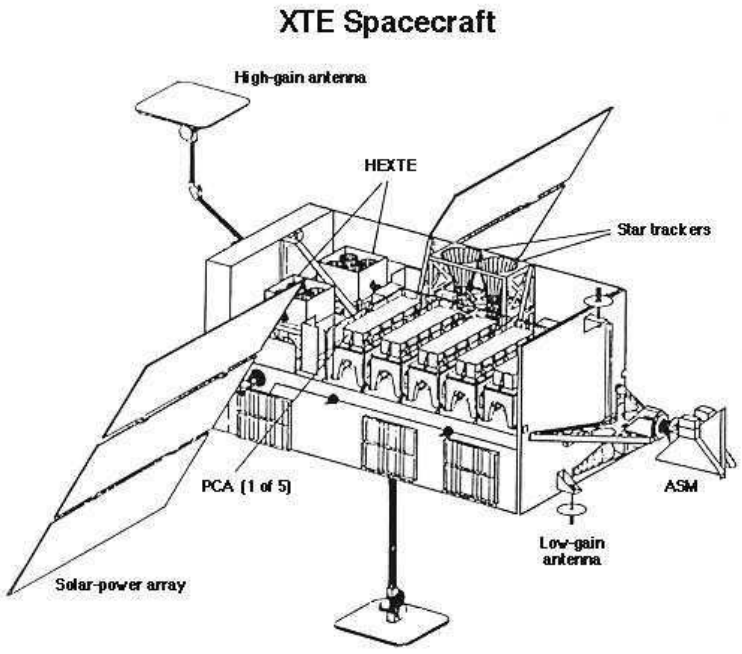

Figure 2.4: RXTE with the PCA, ASM and HEXTE. Courtesy of NASA.

2.2 HE γ-rays

Since the discovery of HE gamma-rays coming from the Crab Pulsar using balloon-borne detectors in the early 1970s, space-based detectors have been responsible for detecting gamma-rays in this energy band. There have been several detectors with different success, such as SAS-II, launched in 1972 (energy range 35 MeV - 1 GeV) and COS-B, launched in 1975 (energy range 150 MeV - 5 GeV). These two instruments discovered around 30 sources, from which only 5 were identified.

In 1991, the Compton Gamma Ray Observatory (CGRO) was launched and its discoveries caused a great impact on the gamma-ray community. It was operational until 2000, and it detected a total of 90 extragalactic sources, 6 extended sources and 170 unidentified sources. This observatory had four instruments: BATSE (Burst And Transient Source Experiment), in soft γ-rays (from 20 keV to 1 MeV), OSSE (Oriented Scintillation Spectrometer Experiment), working from 50 keV to 10 MeV, COMPTEL (imaging COMPton TELescope), operating with energies between 800 keV and 30 MeV and EGRET (Energetic Gamma-Ray Experiment Telescope) designed to operate from 20 MeV to 30 GeV. All were designed to work simultaneously covering an energy range from 15 keV to 30 GeV.

EGRET provoked a major revolution in the field of HE gamma-ray astrophysics, creating the first map of the sky at energies above 100 MeV (see Figure 2.5) and discovering 250 sources, most of which remain unidentified.

In 2002, the INTEGRAL (INTErnational Gamma-Ray Astrophysics Laboratory) satellite was launched by the European Space Agency (ESA) to study gamma-rays with energies between 15 keV and 8 MeV. This satellite is still taking

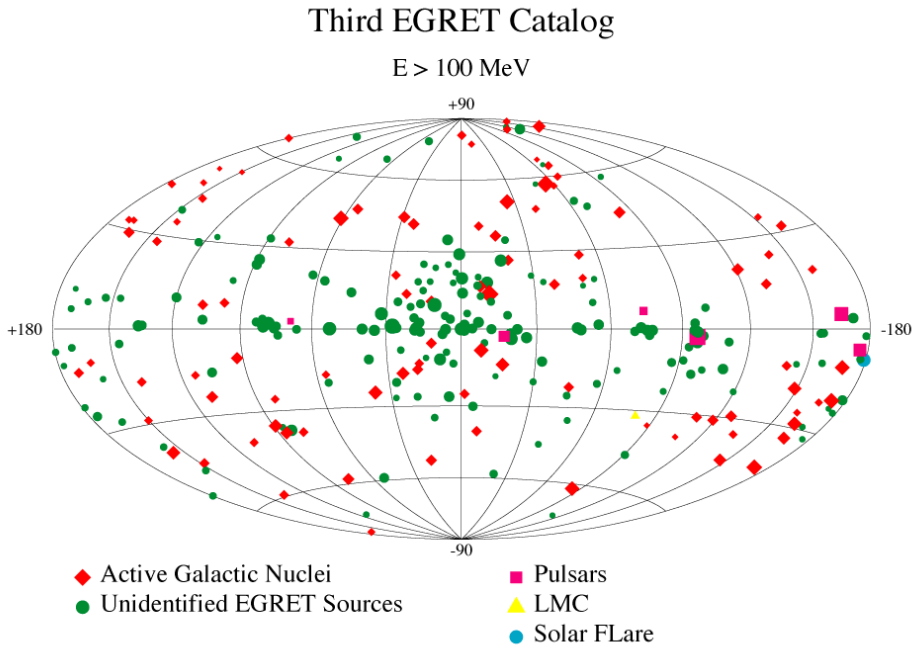

Figure 2.5: EGRET sky map above 100 MeV and all the sources for the 3rd EGRET catalog are also shown. Credit: EGRET Team

data.

In 2007, the Italian satellite AGILE (Astro-rivelatore Gamma a Immagini LEggero) was launched to study the HE gamma-ray sky at energies from 30 MeV to 50 GeV. This satellite is also still taking data.

After the amazing success of EGRET, a new generation of satellites was designed, and NASA created the successor called the Gamma-ray Large Area Telescope (GLAST), which was commissioned to be launched in 2008. GLAST had a field of view and sky survey capability twice as large as the CGRO, and a sensitivity 30 times greater than Compton's EGRET instrument. GLAST also improved upon the BATSE instrument. The satellite was renamed the Fermi Gamma-ray Space Telescope in the honor of the physicist Enrico Fermi.

2.2.1 *Fermi*

Fermi, the new generation HE γ-ray observatory, was designed to observe sources in the energy band from 8 keV to 300 GeV. It was launched in June 2008. *Fermi* travels in a circular low-Earth orbit, at an altitude of 565 km with inclination of $\sim$24.7 degrees. It covers its orbit around the Earth every 90 minutes and is able to view the entire sky every three hours. The mission is designed for a lifetime of five years with a goal of ten years of operations. *Fermi* (see Figure 2.6) carries two instruments: the Large Area Telescope (LAT) and the Gamma-ray Burst Monitor (GBM). The main instrument, the LAT (Figure 2.7), has a field of view of $\sim$2 sr (20 % of the entire sky). Within its 1.8 m^3 housing, it uses 880000 silicon strips to

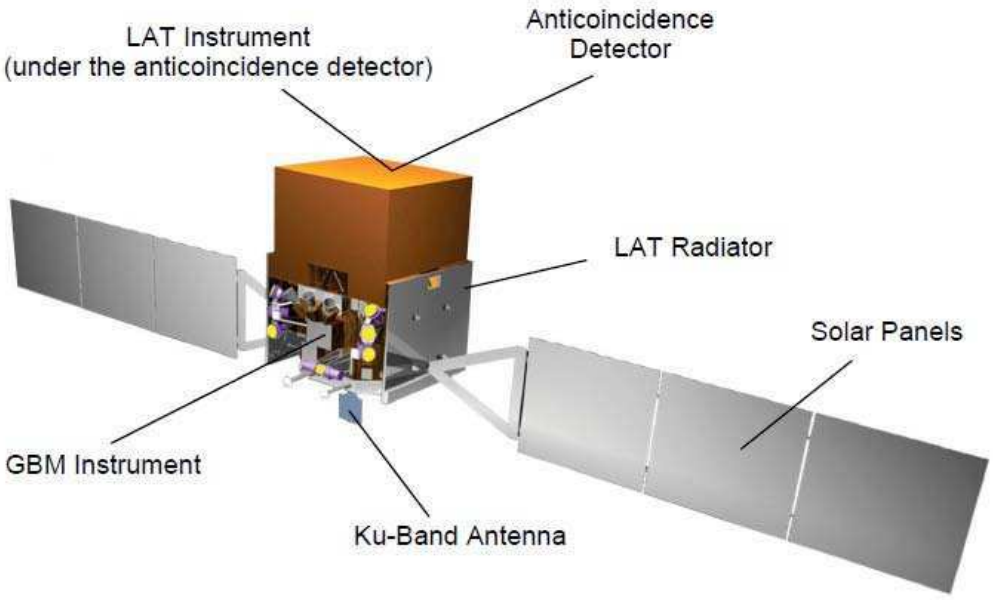

Figure 2.6: Fermi Gamma-ray Space Telescope. Images credit: NASA.

detect γ-ray photons in the energy range from 30 MeV to 300 GeV. The LAT has highest sensitivity above 10 GeV, and is at least 30 times more sensitive than any previous γ-ray instrument. The complementary GBM instrument is designed to detect gamma-ray bursts over a wide range of timescales.

The *Fermi*-LAT instrument is a pair-conversion telescope in which the four main subsystems are: a tracker, a calorimeter, an anti-coincidence detector (ACD) and the data acquisition system (DAQ). When an incoming γ-ray photon enters the LAT (see right diagram in Figure 2.7), it first passes through the ACD without producing a signal. The γ-ray photon interacts in one of the 16 thin tungsten sheets turning into an electron-positron pair. The tracker uses silicon strips that are alternated in perpendicular directions, allowing the tracks of the electron-positron to be measured, which allows the arrival direction of the photon to be determined. The electron-positron enter the cesium diodide calorimeter which finally measures the total energy deposited by the particles so that the energy of the photon can be determined. The ACD makes it possible to reject 99.97 % of undesired cosmic rays events (Jenner 2008) because when a cosmic-ray passes through the ACD, it causes a flash of light.

In September 2011, the *Fermi*-LAT Collaboration released to the public the second catalog with all the *Fermi* sources detected until then (see Figure 2.8). This catalog contains 1873 sources detected and characterized in the 100 MeV to 100 GeV range, of which 127 are firmly identified and 1170 are reliably associated with known counterparts or likely gamma-ray-producing source classes.

The *Fermi*-LAT Collaboration has constructed the populations of gamma-ray sources that are represented in the catalog and the results are shown in Figure 2.9. Individual LAT-detected sources provided identifications or plausible associations

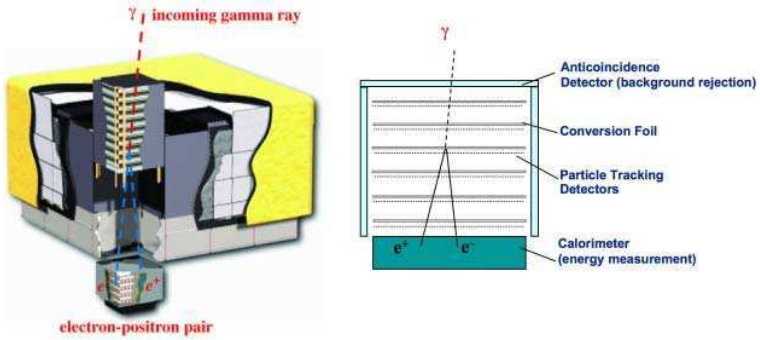

Figure 2.7: The LAT has 16 towers of particle detectors, seen (left) before the installation of the anti-coincidence detector. Each tower contains a tracker module and a calorimeter module (right). The data acquisition system is located underneath the towers. Images credit: NASA.

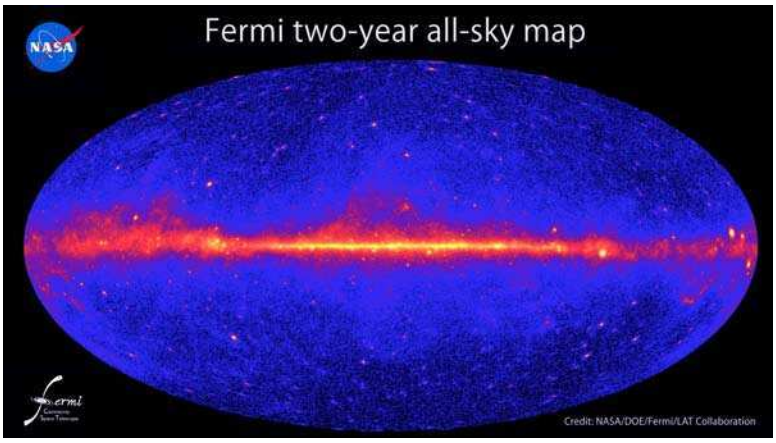

Figure 2.8: Fermi-LAT second catalog containing 1873 sources detected in the 100 MeV to 100 GeV range. Image credit: NASA.

with sources in other astronomical catalogs. More than 55 % of the detected sources are blazars.

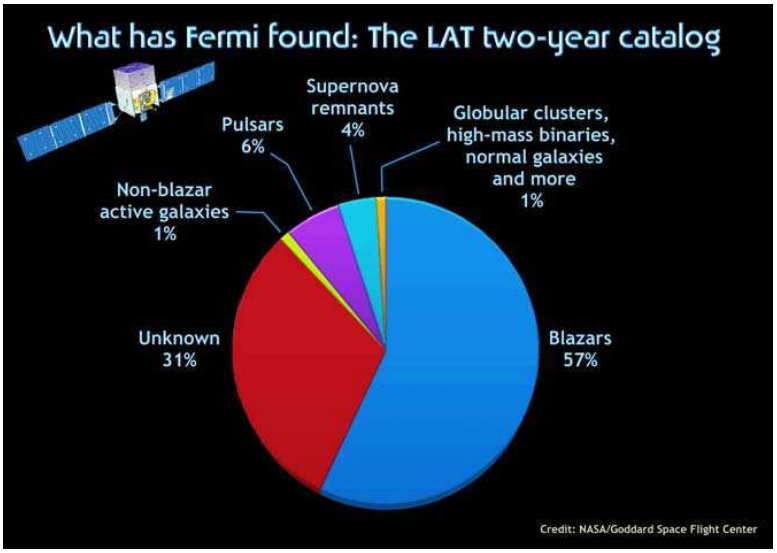

Figure 2.9: Different types of sources detected by *Fermi*-LAT in the second catalog. Image credit: NASA.

2.3 Radio

The search for radio sources in the sky began when Hertz first demonstrated the existence of radio waves in 1888. After decades of non-detection on bright sources such as the Sun, in 1933 Jansky discovered cosmic radio waves which are originated in the Milky Way. With the improvement in sensitivity and reliability of radio systems during World War II, the discovery of radio sources other than the Sun and the Milky Way became commonplace. Astronomical radio sources may be classified into two categories: those which are radiated by thermal mechanisms and those which are radiated by non-thermal processes.

The Earth's atmosphere is transparent to radio waves, in the frequency range from 15 MHz to 600 GHz. Radio telescopes are typically created with a parabolic dish where the radio waves are reflected to the detector. There the signal is amplified, fully reduced and imaged using adequate software packages. The employed strategies to make those images, depend on the frequency of which the observations were performed.

In the following section the radio instruments involved in several campaigns of Mrk 421 and Mrk 501 from 2007-2009 are described.

2.3.1 Metsähovi Radio Observatory

The Metsähovi Radio Observatory has operated a 14-meter diameter radio telescope located in Finland since 1974. An upgrading of the telescope was completed in 1994 providing a surface accuracy of the present telescope of around 0.1 mm (see Figure 2.10).

The activities at Metsähovi are concentrated on millimeter and microwaves with frequencies from 2 to 150 GHz. Since the early 1990's Metsähovi Radio Ob-

Figure 2.10: Metsähovi Radio Observatory. Image courtesy of Metsähovi Radio Observatory, Aalto University

servatory has been one of the few institutes in the world where very long baseline interferometry (VLBI) data acquisition systems have been actively constructed and further developed.

2.3.2 UMRAO

The University of Michigan Radio Astronomy Observatory (UMRAO) operates a radio telescope with a 26-meter diameter parabolic reflector and 10.98 m focal length, which was built in 1958 on Peach Mountain, MI, US (see Figure 2.11). During the past two decades this telescope has been used for the study of total flux density and linear polarization from active extragalactic objects in the radio-wavelength region at 4.8, 8.0 and 14.5 GHz. The main purpose of this telescope is to obtain long term scale observations, searching for long/short periodicity, variability in the jet and the core, and detecting outbursts.

2.3.3 OVRO

A 40 m radio telescope was constructed at the Owens Valley Radio Observatory (OVRO) in 1968 (see Figure 2.12). In the 1970s, it has been used as part of a baseline of 1.25 km, using it as interferometer. Also, it has been used as part of the Very Long Baseline Interferometer (VLBI).

Since 2007, the 40 m telescope at the OVRO has been dedicated to monitor in the 15 Ghz, than 1500 blazars almost twice a week. The importance of this monitoring is to compare those observations with the *Fermi*-LAT HE gamma-ray observations of the same blazars, looking for correlations, variability in the fluxes, and finally, getting a better understanding of the emission mechanisms of those blazars.

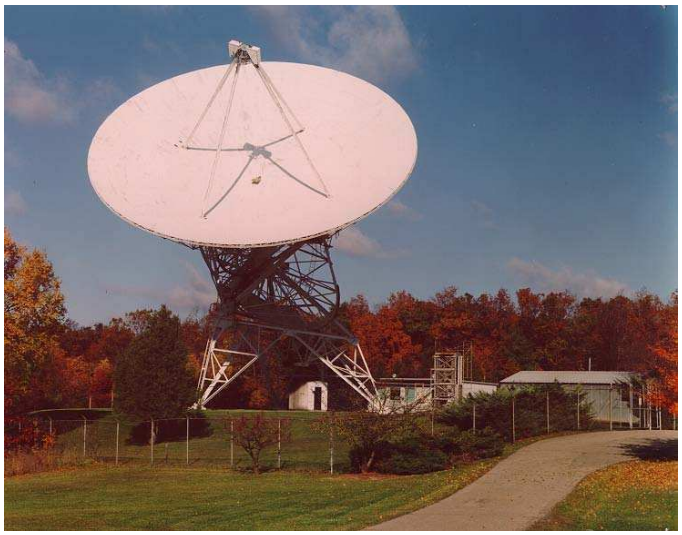

Figure 2.11: UMRAO telescope.

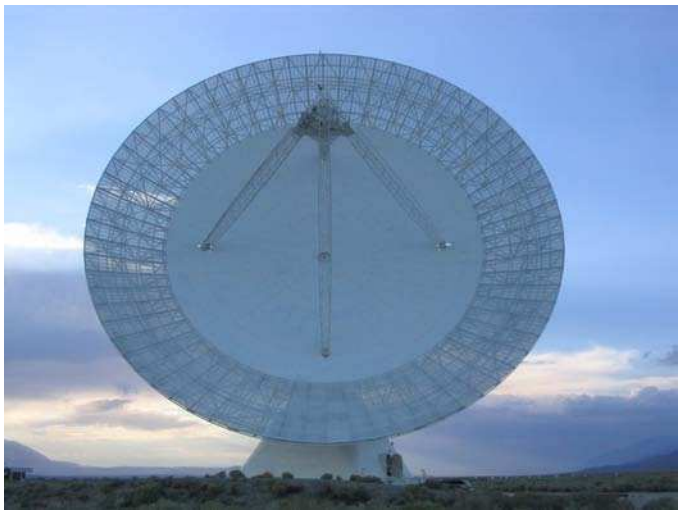

Figure 2.12: The 40 m telescope at the Owens Valley Radio Observatory.

2.4 Optical

Looking at the sky with optical telescopes has been done for centuries since Galileo. To study the mysteries of the universe and trying to explain them have been the main goals of optical astronomers since then. There have been many improvements in the optics over the years, which have allowed outstanding discoveries, such as the deep field and amazing images taken with the Hubble Space Telescope during the last 20 years. Another improvement in ground-based optical telescopes was the adaptive optics, a mechanism that compensates air atmospheric changes. This kind of improvements were implemented, e.g., by the ESO, in the four 8.2-meter telescopes located in Paranal, Chile that can be used as part of a giant

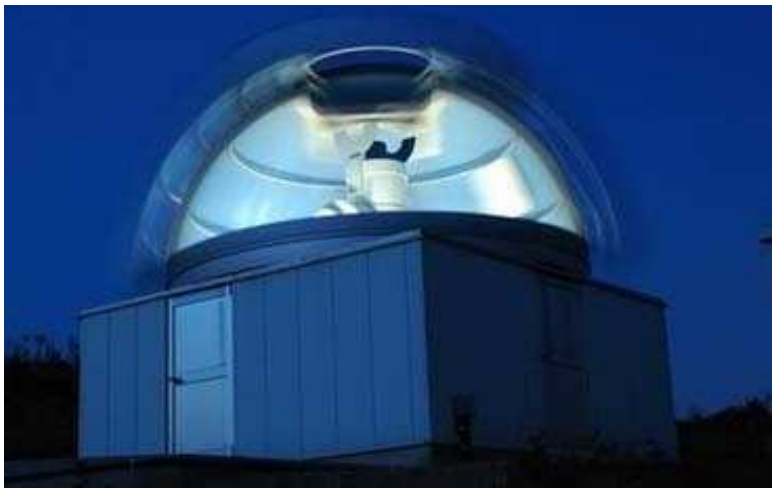

Figure 2.13: MitSume Observatory in Japan.

interferometer, the Very Large Telescope Interferometer (VLTI). The VLTI can reconstruct images with an angular resolution of milliarcseconds and take images of objects with magnitudes of 30 in a one-hour exposure.

In the case of blazars, attempts to find correlation between gamma-ray and optical bands have been made for several blazars (e.g. Albert et al. 2006; 2007) but it is not clear that such correlation exists. Additionally, there have been attempts to correlate the optical polarization in the jet with flares at the VHE regime (e.g. Marscher et al. 2010).

A description of the optical instruments involved in the various campaigns is given in the following section.

2.4.1 MITSuME

Multicolor Imaging Telescopes for Survey and Monstrous Explosions (MITSuME) have been built to perform Multi-color photometry of NIR/optical GRB afterglows, covering the wavebands from *Ks* to *g*, and allowing photometric redshift measurements up to $z = 10$. Two 50 cm optical telescopes were built, one at Akeno and the other one at Okayama Astrophysical Observatory (OAO), in Japan. Each telescope has a Tricolor Camera, which allows it to take simultaneous images in *g*, *Rc*, and *Ic* bands. A previous 91 cm telescope at OAO was modified to an IR telescope and performed *JHKs* photometry (see Figure 2.13). MITSuME telescopes automatically monitor pre-selected AGNs and galactic transients for multi-wavelength studies with *Fermi* while it is waiting for GRBs. A search for an optical counterpart is also performed.

2.4.2 WIYN

The Wisconsin Indiana Yale NOAO (WYIN) Telescope is a 3.5-meter optical instrument located at Kitt Peak, Arizona (see Figure 2.14).Its instrumentation in-

Figure 2.14: The WIYN 3.5 m telescope in Kitt Peak, Arizona. Image courtesy of Kitt Peak Observatory

cludes a CCD camera with a 10 arcminute field of view, an infrared image with tip-tilt correction, and a bench spectrograph which is fed by fibers from either a multi-object, a fiber-positioning robot or an integral field unit for studies of extended objects.

2.4.3 GASP

In 2007, the Whole Earth Blazar Telescope (WEBT) started the GLAST-AGILE Support Program (GASP). Its aim is to provide observing support at longer wavelengths (optical-to-radio) for the observations of the gamma-ray satellites *Fermi* and AGILE. The GASP strategy is a long-term monitoring of selected targets, with periodic data gathering and analysis. Markarian 421 and Markarian 501 are amongst its blazar targets. At present, a dozen telescopes are involved in this effort.

Chapter 3

Very High Energy γ-ray Techniques & Instrumentation

VHE gamma-ray astrophysics uses observation techniques that are quite different from observations at any other wavelength. Astronomical observations in optical and radio bands can be performed from the Earth's surface with minimal absorption in the atmosphere. At gamma-ray energies, however, photons are absorbed by the atmosphere and are unable to penetrate to the ground level. Therefore, telescopes need to be placed outside the atmosphere in order to receive the energetic photons, as it happens in the case of satellites or balloons that are used to detect X-rays and HE gamma rays. Nevertheless, satellites cannot be used for VHE gamma-rays, simply because the TeV gamma-ray fluxes are typically too low (1 photon/m^2/year). Nevertheless, the result of the interaction of gamma rays with the atmosphere can be used to detect these photons using detectors on the ground. The Imaging Atmospheric Cherenkov Technique (IACT) is, until now, the only available method for the detection of this very high energy radiation.

The following sections of this chapter are devoted to describing the phenomena produced by primary gamma-rays and cosmic-rays reaching the Earth, its interaction with atoms in the atmosphere and the development of these interactions. Differences between particle and photon showers, methods of detection for these radiations and the available analysis methods used to characterize these showers using the imaging atmospheric Cherenkov technique are also discussed. In sections 3.4 and 3.5, a more detailed description of the inner workings of the Whipple 10 m telescope and the VERITAS array, being the main telescopes which observations are used in this work, can be found.

3.1 Extensive Air Showers

The interaction of an energetic primary ray (proton, heavy nucleus or photon) with the Earth atmosphere creates a cascade of secondary particles, which, if electrically charged, disturb the environment producing Cherenkov light that can be collected by a suitable detector. These cascades are known as extensive air showers because the lateral development of generated Cherenkov photons is ap-

proximately $10^4\,\mathrm{m}^2$ (at the Earth's surface). Thus, the atmosphere acts as a very good calorimeter for primary rays. By detecting the Cherenkov light generated by the passage of charged particles and photons from the cascade in the medium, it is possible to obtain the energy of the primary ray. The advantage of this detector is that it can be located anywhere within the radius of development of the photons generated in the process. By detecting the Cherenkov radiation from air showers, this detector has the immense advantage of increasing the effective collection area by several orders of magnitude compared to satellites, since the collection area is approximately the area of the air shower.

A steady isotropic flux of high-energy hadronic cosmic rays (protons and heavy nuclei) bombard the upper Earth atmosphere all the time, initiating cascades of secondary particles and photons. Most of these secondary particles travel faster than the speed of light in the medium and emit Cherenkov radiation. Also, VHE gamma rays induce extensive electromagnetic air showers in the atmosphere irradiating Cherenkov light. Therefore, it is very important to be able to distinguish between images from gamma rays and those from cosmic rays. The air showers produced by gamma rays and by cosmic rays and the differences between them are qualitatively described below.

3.1.1 γ-ray Air Showers

When gamma rays enter the atmosphere, the main radiative process that occurs is pair production, which dominates over all other processes at high energy. As shown in Figure 3.1, the secondary particles (electrons and positrons) produce gamma-rays via Bremsstrahlung radiation, and these gamma rays again undergo pair production. These chain reactions continue producing lower energy particles, reaching a maximum development of the cascade, when the average particle energy goes down the critical energy ($E_c = 81\,\mathrm{MeV}$ in air), and the probability of pair production and ionization is the same, with no longer enough energy to induce further reactions. The radiative processes are then dominated by ionization of electrons and positrons, and by Compton scattering of gamma rays.

The total number of particles in the shower and the height at which the shower maximum takes place, depend on the energy of the primary gamma-ray incident on the upper atmosphere as well as on the depth of the first interaction. Gamma rays with energies of 100 GeV and 1 TeV produce showers with the maximum at an altitude of approximately 10 km and 8 km, respectively (Weekes 2003).

One characteristic of the pair production process is that the electrons and positrons are produced at a small angle relative to the incident gamma ray. Therefore, the electromagnetic shower is small in lateral size (see discussion below) and the primary gamma-ray direction is preserved by the shower (see Figure 3.2).

3.1.2 Cosmic-ray Air Showers

Cosmic rays are charged particles, such as protons, electrons, ions or heavier nuclei like iron. In the context of gamma-ray astrophysics, protons are of major interest since they constitute around 90 % of the cosmic rays. Electrons represent only

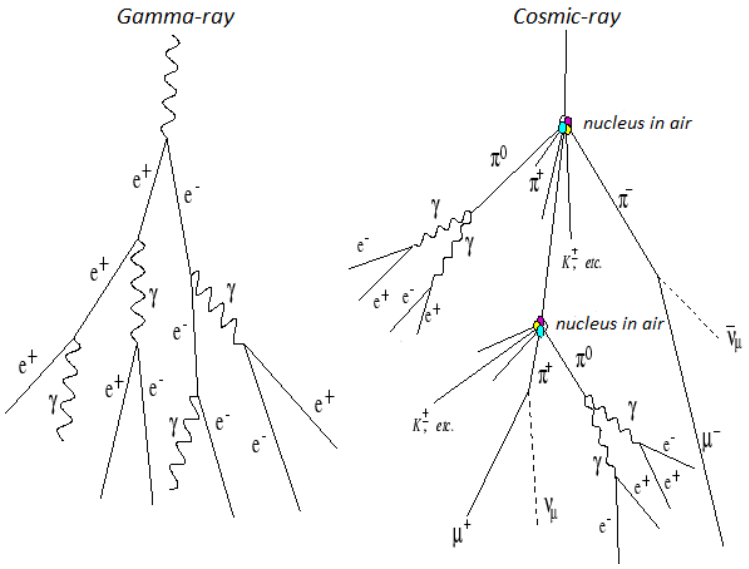

Figure 3.1: Scheme of the development of a gamma-ray (left) and a cosmic-ray (right) induced shower. Figure credit: Konrad Bernlöhr.

1 % of the cosmic rays and their arrival directions are distributed isotropically. Heavier nuclei are also rare (less than 1 %) and produce showers that are much more spread on the ground. As such, they cannot be detected efficiently with the technique described in section 3.3. Therefore, only proton-induced showers will be discussed here. When protons enter the atmosphere, they interact with nuclei that are present in the atmosphere. The interactions create charged and neutral pions and other particles, such as muons, electrons and light atomic nuclei. Figure 3.1 illustrates schematically an example of a cosmic-ray induced shower. The pions are responsible for electromagnetic sub-showers. Neutral pions decay into two gamma rays, and the charged pions decay into muons and neutrinos. In the first case, secondary gamma rays are induced by the pair creation process and in the second, muons decay into electrons or positrons or propagate to the ground. Compared to gamma-ray induced showers, cosmic-ray showers are much broader.

The main observational characteristic differentiating air showers produced by gamma- and cosmic-rays is the lateral spread of the showers. As shown in Figure 3.2, gamma-ray showers are much more compact.

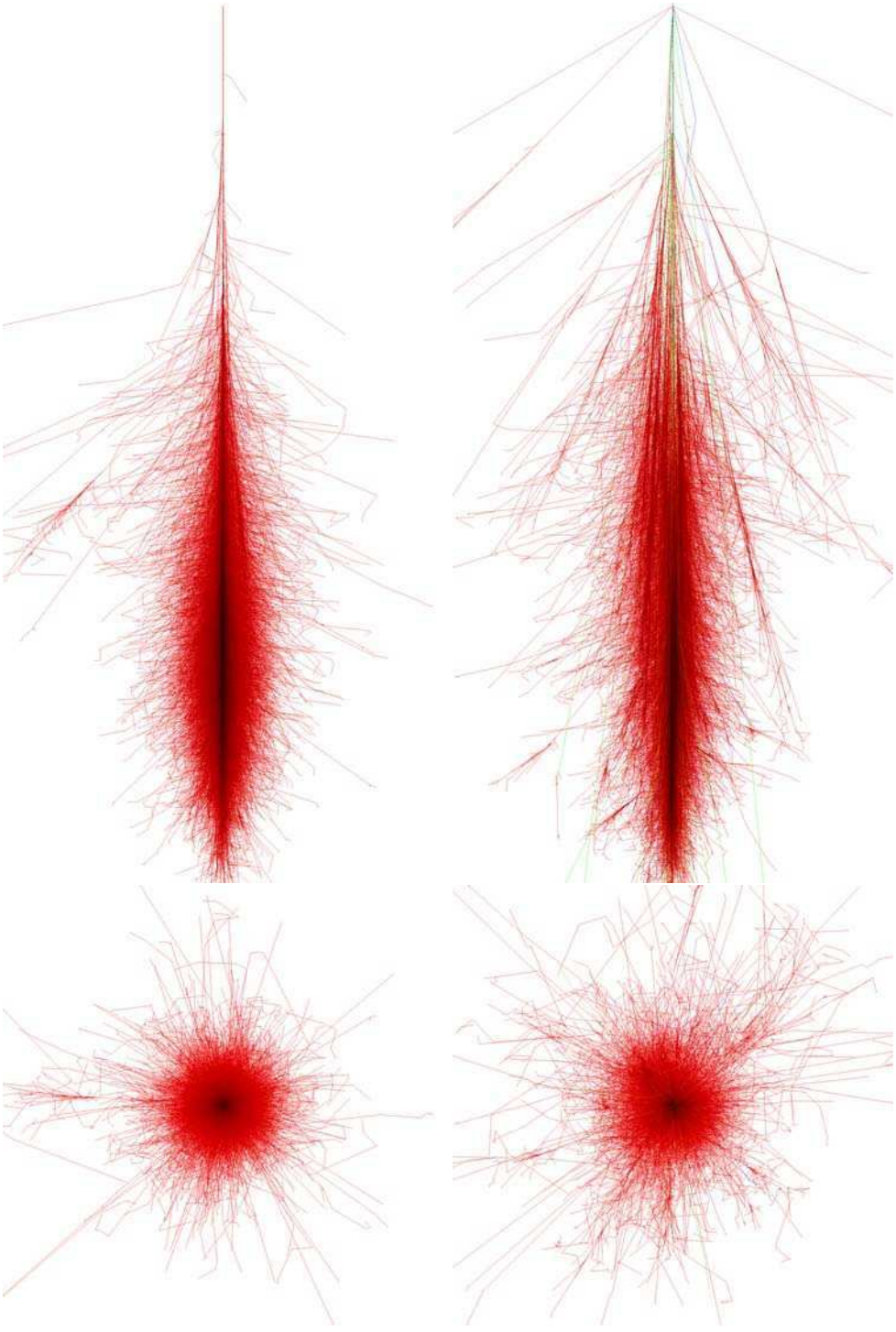

Figure 3.2: Simulated air-showers produced by a 1 TeV gamma-ray with longitudinal view (left) and a 1 TeV proton (right). Vertical scale is 30 km and horizontal scale is ± 5 km around the shower core. Bottom panels shows the same showers seen from the floor. Colors indicate different particles: electrons, positrons or photons (red), muons (green) and hadrons (blue). Figure taken from http://www-ik.fzk.de/corsika/.

3.2 Cherenkov Light in Air Showers

Cherenkov radiation is emitted when a particle passes through a dielectric medium while traveling faster than the speed of light in the medium. The speed of light (v_{light}) in a medium different than vacuum is determined as:

$$v_{\text{light}} = c/n$$

where c is the speed of light in vacuum and $n > 1$ is the refractive index of the medium.

Thus, the speed of light in the medium is lower than c and it is possible that the particle be traveling with a speed greater than v_{light}. When a charged particle travels through a dielectric medium, the atoms in the surroundings become polarized. Once the particle has passed, the polarized atoms relax by emitting a light pulse which lasts for a very short time (∼10-100 ns). The emitted light properties depend on the speed of the traveling particle (v). If it is moving slowly ($v < v_{\text{light}}$) the polarization is symmetric along the path of the particle (see left panel in Figure 3.3); the radiation produced by the relaxation is not coherent and the radiation does not travel long distances. If the particle moves fast ($v > v_{\text{light}}$), the polarization becomes asymmetric as shown in the right panel of Figure 3.3. In this case, the emitted radiation is coherent, permitting emission over long distances. The coherent radiation emitted during the relaxation is called Cherenkov radiation. The coherent Cherenkov radiation is emitted as a wavefront with an angle θ respect to the direction of the traveling particle. Since the particle travels at a speed $v > v_{\text{light}}$, in a time t the particle will have covered a distance of vt. As the wavefront is moving at v_{light}, it will have traveled a distance $v_{\text{light}}t < vt$. It is geometrically easy to deduce the angle θ as:

$$\cos(\theta) = \frac{1}{n\beta} \tag{3.1}$$

where β is v/c.

Thus, for a particle traveling in a medium of constant refractive index, θ will stay constant. In addition, from Equation 3.1, the energy threshold for a particle to create Cherenkov radiation can be deduced. Indeed, just below the threshold, $\theta = 0$ and $\beta = 1/n$. The energy of the particle is therefore given by:

$$E_{\text{threshold}} = \frac{m_p c^2}{\sqrt{1 - \frac{1}{n}}} \tag{3.2}$$

where m_p is the mass of the particle.

In the context of extensive air showers, Cherenkov radiation is emitted by the shower's particles as long as they have a speed $v > v_{\text{light}}$. In the case of gamma-ray-induced air showers, since only electrons and positrons are produced in a compact

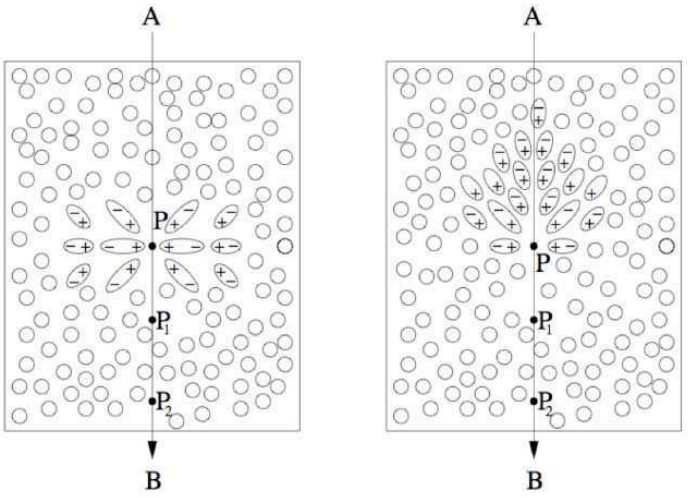

Figure 3.3: Polarization of the surrounding atoms from a particle traveling in a medium. Left panel: Case of a slow particle ($v < v_{\text{light}}$). Right panel: Case of a fast particle ($v > v_{\text{light}}$). Figure taken from Horan (2001).

shower, the Cherenkov emission is compact. In the case of cosmic-ray-induced showers, since several sub-showers are created, the Cherenkov radiation is emitted along the main shower and sub-showers, leading to a less uniform distribution on the ground. Since the density of the atmosphere changes with the height (being lower at higher altitudes) the atmosphere's index of refraction changes as well, being also lower at higher altitudes. From Equation 3.2, it can be deduced that $E_{\text{threshold}}$ is higher at higher altitudes and increases with the mass of the particle. Therefore, more massive particles such as muons or protons need higher energies to produce Cherenkov radiation in comparison to electrons.

Figure 3.4 shows the Cherenkov emission schematically along an air shower. Most of the Cherenkov light is emitted at the shower maximum (~ 8 km), as seen in the lower panel of Figure 3.4. The Cherenkov light pool created has a radius of $\sim$120 m. Therefore, a single incoming gamma-ray can be detected in an area of ~ 50000 m^2.

Figure 3.5 shows the lateral distribution of Cherenkov photons at the ground and at an altitude of 2300 m. The curves may serve as a warning of that the simple picture of a roughly uniform light pool is correct until 130 m from a gamma ray shower (Hillas 1996).

After 1961, when Hill & Porter (1961) recorded image-intensifier pictures of Cherenkov light from air showers, the potential of the IACT technique for gamma-ray telescopes was discussed. The first implementation for this technique was made by Grindlay (1972) with a simple stereoscopic system (the "double beam technique") that was used to reduce the hadron background, producing some interesting results in 1976 (Grindlay et al. 1976). These type of detectors were called the first generation of Cherenkov telescopes. In the 1980s, a second generation of Cherenkov telescopes were built with better mirror design, photomultipliers with better quantum efficiency, better optimization for selecting gamma rays, and re-

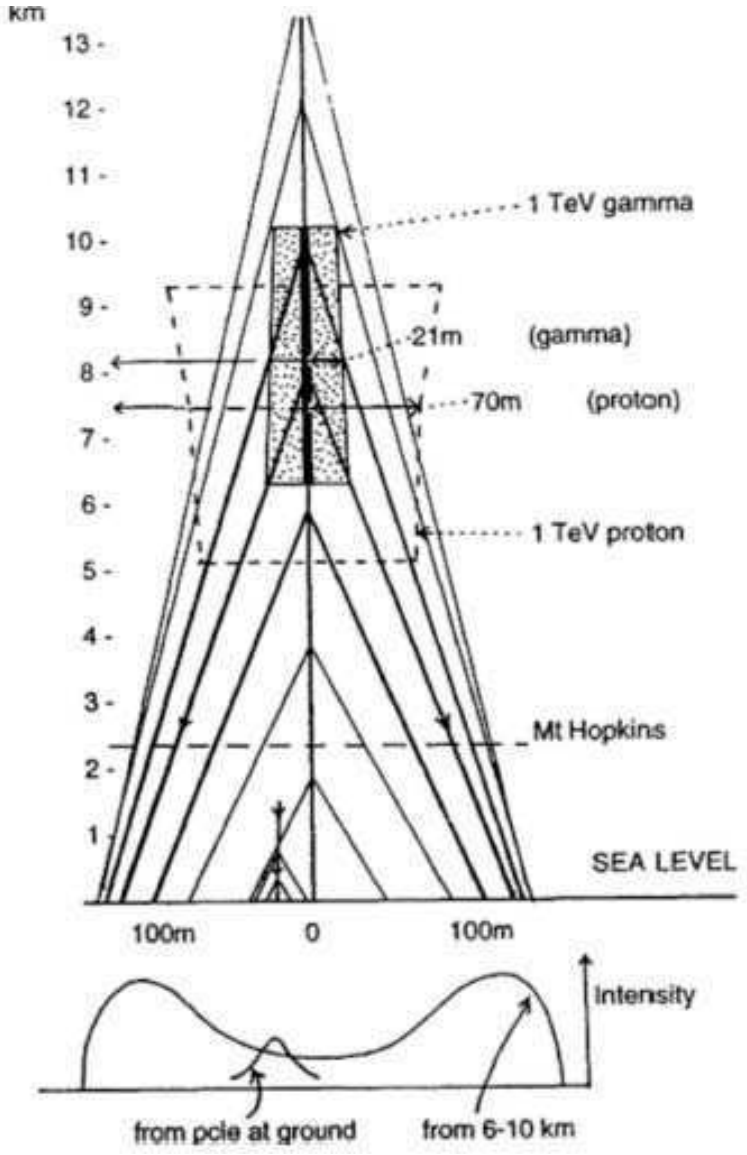

Figure 3.4: Cherenkov light distribution from an air shower. The grey box represents the region where the maximum of light is emitted by a gamma-ray shower. The dashed-line box represents the maximum emission region for a cosmic-ray shower of the same energy. The bottom panel shows the intensity of the Cherenkov light on the ground. Figure taken from Hillas (1996).

jecting hadron showers. The Whipple Telescope has been the pioneer in this field (Cawley et al. 1990). Also the experiments HEGRA (Aharonian et al. 1991) and CANGAROO (Ebisuzaki et al. 1991) adopted the IACT technique.

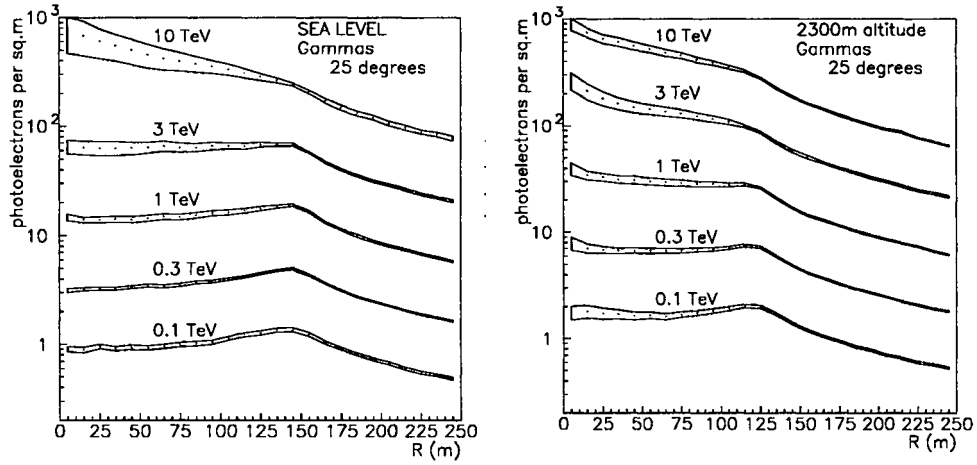

Figure 3.5: Lateral Distribution of the Cherenkov light at two different altitudes. The uncertainty in the average is indicated as the width for each band. Figure taken from Hillas (1996).

3.3 Imaging Atmospheric Cherenkov Technique

In opposition to radio or optical telescopes, in which photons are directly detected, Imaging Air Cherenkov Telescopes detect VHE gamma-rays indirectly by looking the Cherenkov radiation produced in air showers, in the upper atmosphere, by photons or cosmic rays, as shown in Figure 3.6.

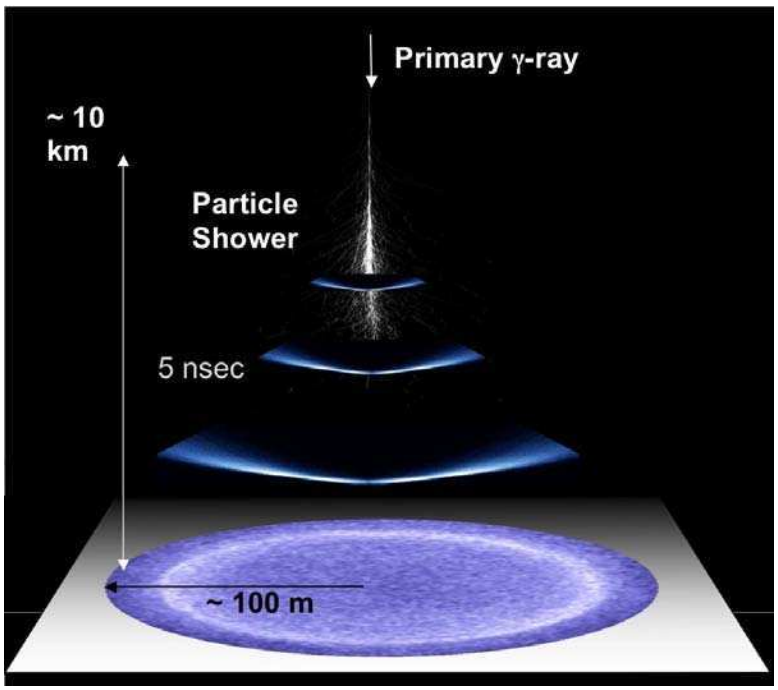

Figure 3.6: Scheme of a Cherenkov light pool created by a gamma-ray-induced air shower. Figure from http://astrum.frm.utn.edu.ar

The general aim of an imaging atmospheric Cherenkov telescope is the detection of gamma-rays coming from the target source. However, 99 % of the images recorded by this kind of telescope come from hadronic showers or radiation from single local muons or sky-noise fluctuations. Thus, it is important to record as many events as possible, finding the differences between γ-ray images and background images in order to facilitate the maximal rejection of background events (Quinn 1995).

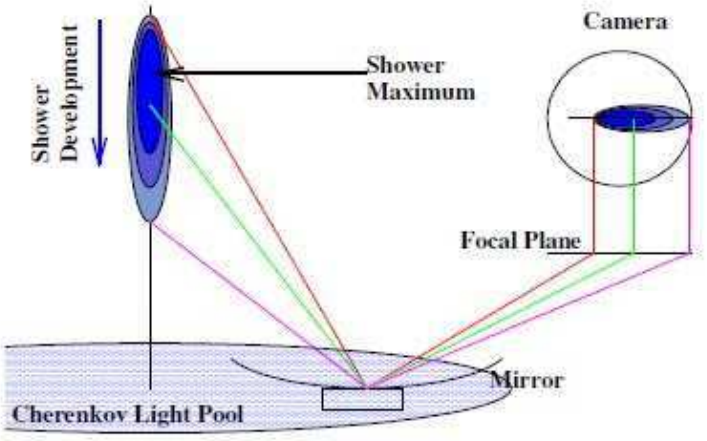

Figure 3.7: Schematic illustration of the imaging of an electromagnetic shower in the focal plane of an IACT located within the Cherenkov light pool. Image from Cogan (2006).

The important aspect of this technique is that it can reconstruct the direction and energy of the primary gamma-ray (see Figure 3.7), by examining the candidate gamma-ray-initiated shower remaining after the image cuts discussed in section 3.4.1. The incidence direction of the candidate gamma-ray shower can be determined from the shower orientation, whereas the primary's energy can be estimated by using simulations to produce tables of energy values, "lookup tables" that are based on several parameters of the image (see section 4.1).

3.4 The Whipple 10m Telescope

The Whipple 10 m γ-ray telescope (see Figure 3.8) is located at the Fred Lawrence Whipple Observatory (Kildea et al. 2007), in southern Arizona, at an elevation of 2312 m. It was built in 1968 and it is sensitive in the energy range from 200 GeV to 10 TeV, with a peak response energy (for a Crab-like spectrum) of approximately 400 GeV. This telescope has been exclusively used for gamma-rays detection since 1982, and it is significantly less sensitive than the current version of IACTs such as VERITAS (see section 3.5). It has been used since 2005 to extend the TeV coverage as part of a blazar monitoring program, for several blazars, including Mrk 421 and Mrk 501. The Whipple Telescope has a slew speed of 1° per second, and a tracking resolution of approximately 0.01°.

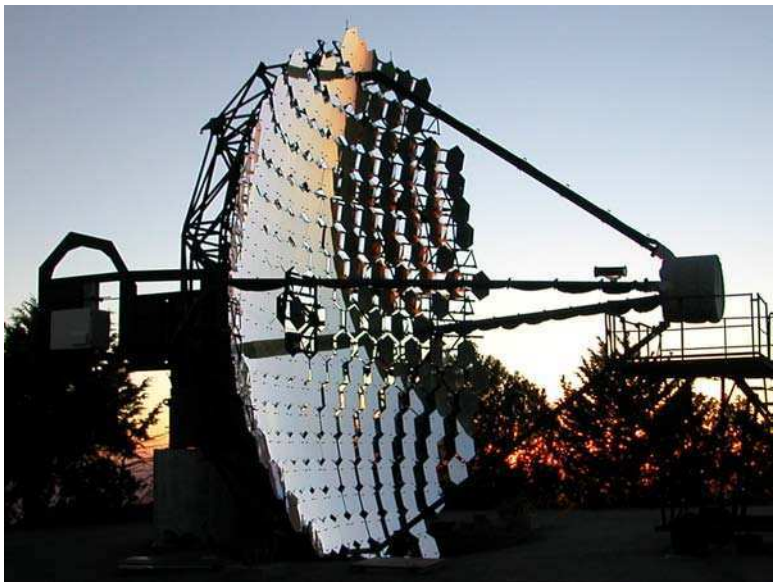

Figure 3.8: The Whipple 10 m telescope.

The telescope comprises a 10-meter optical reflector, composed of 248 spherical front-aluminised glass mirrors in a Davies-Cotton design (Davies & Cotton 1957, Weekes et al. 1972) (see Figure 3.9). The camera is located at the focal plane, whose last upgrade was in 1999 (Finley et al. 2001), with 379 photo-multiplier tube (PMT) pixels sensitive to blue and ultra-violet (UV) with a quantum efficiency of 20 %, where each PMT has a 0.12° FOV (see Figure 3.10), giving a total FOV of 2.6° for the camera. Light cones are placed in front of the PMTs to shield the PMT photo-cathodes from background light and to reduce photon losses from gaps between pixels. The telescope has an elevation-azimuth mount and a counterweight (see Figure 3.11 for more details). The mirror point spread function (PSF) is measured using a CCD camera in the center of the dish, recording images of bright stars projected onto the focal plane. It is optimized for elevations of $60° - 70°$ (where most observations are made), with a value around 0.11°, comparable to the PMT diameter. Details of the PSF, mirror alignment measurements and pointing corrections are given in Chapter 4.

Because IACTs cannot directly observe gamma-rays, the physical parameters of the primary gamma-ray need to be reconstructed from the recorded shower images. Gamma-rays are selected using the image shape and the Hillas parameters (Hillas 1985) after a cleaning process, a pedestal subtraction and a flat fielding process. More information about the energy reconstruction can be found in Chapter 4.

3.4.1 Whipple Data Acquisition System and Data Analysis

A schematic of the data acquisition system for the Whipple telescope is shown in Figure 3.12. Photons enter PMTs where electronic photoelectrons are produced and multiplied typically 10^5 times to give short pulses at the anodes. The signal

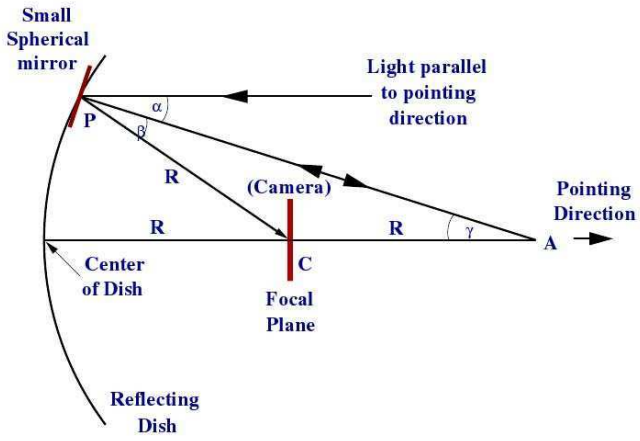

Figure 3.9: Diagram of the Davies Cotton reflector design. Figure taken from Kildea (2002).

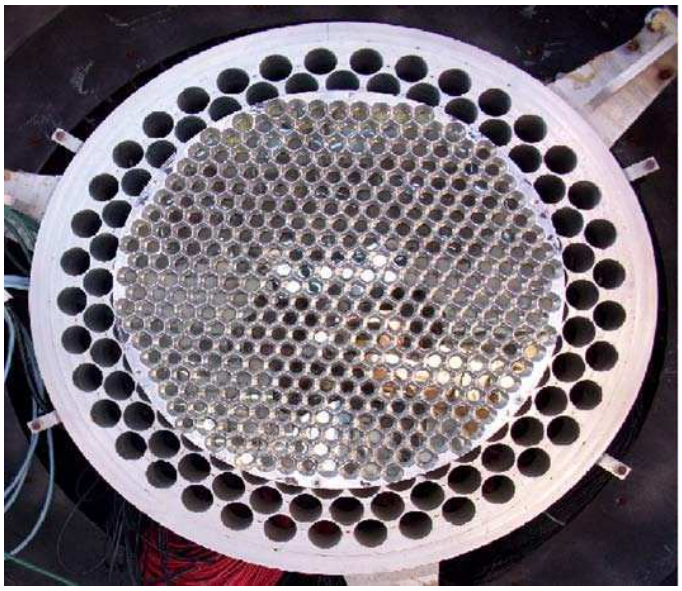

Figure 3.10: Camera of the Whipple 10 m telescope.

from the PMTs goes to the amplifiers, where it is amplified 10 times. From there it is split into the current monitor, the trigger system and a 120 ns delay cable that goes to the charge-to-digital converter (QADC). The trigger system processes the signal, saving the events in which the pixels exceed a threshold level within a short coincidence time window of a few nanoseconds. When a trigger occurs the signal for each PMT is integrated for 20 ns and converted to digital counts by the QADC. This information is sent to a data acquisition computer along the Computer Automated Measurement And Control (CAMAC) backplane with the information of the global position system, GPS, time of each event, together with telescope elevation and azimuth positions. More information can be found in Toner (2009).

Figure 3.11: Structure of the Whipple 10 m telescope.

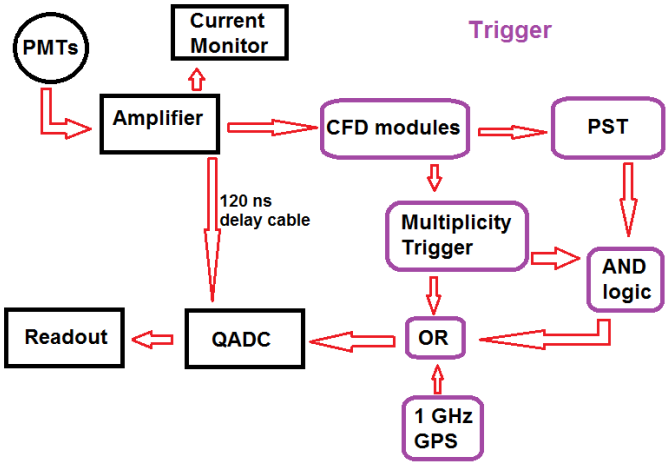

Figure 3.12: Diagram of the Whipple 10 m data acquisition system.

Due to the 20 ns ADC integration time, some signal from night-sky background is introduced. This is accounted for in offline analysis by using a regularly injected pedestal. The pedestal of a channel is a measure of its integrated mean charge in the absence of a Cherenkov signal. In order to measure the pedestal in each channel, forced triggers are injected into the data stream at a rate of 1 Hz. Also, the pedestal-variance is calculated in each pixel and is used to determine the sky brightness, noise level and image cleaning threshold. The cleaning process works to discern in all the PMTs with signal which ones are related to Cherenkov light coming from the gamma-ray shower and which are from noise or background. To be considered in the core of the image called *picture* pixels, the signal recorded in a pixel must be more than 4.25 times its pedestal distribution; and to be included in the *boundary* pixels (pixels adjacent to the core) the signal must be more than 2.25 times the pedestal distribution. These values are derived from the optimization of the signal-to-noise ratio using Crab Nebula observations. All pixels not fulfilling the *picture* and *boundary* conditions are not taken into account for the rest of the analysis. The images are flat-fielded using a laser run taken every night to determine the PMTs gains.

Each clean, pedestal subtracted and flat-fielded image is parameterized using the Hillas 2nd-moment-parameterization recipe (Hillas 1985, Reynolds et al. 1993); the Hillas parameters are used in order to distinguish between gamma-ray and hadronic showers. Assuming each event (image) has an elliptic shape, the *length*, *width*, *size*, *distance* and *alpha* parameters are determined (see Figure 3.13 and Table 3.1 for a better description of each parameter). Figure 3.14 shows an example of parameter distributions for a 28 minute run of Crab Nebula data. Other parameters are also defined taking into account the brightness of the image; *max1*, *max2*, *max3* parameters, are defined as the three highest ADC signals recorded in the camera for each event. Figure 3.15 shows the alpha plot distribution for a 28 minute run of Crab Nebula data. One of the conditions for an event to be considered as a gamma-ray is that *alpha* should be $< 15°$, in which it is assumed that a point source is located at the center of the camera's field-of-view. If the events are truly coming from the source, the peak must be in the first bin of the alpha plot, for which $\alpha < 5°$ (see Figure 3.15).

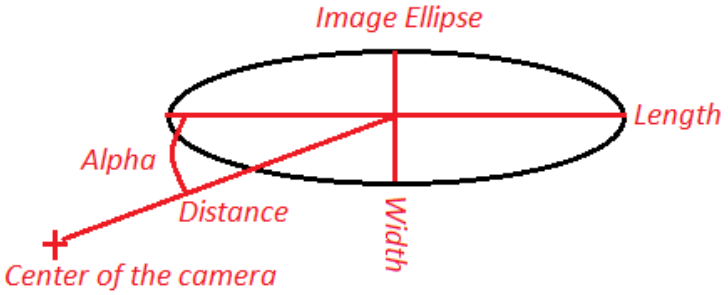

Figure 3.13: Hillas's parameters.

Parameters	Definition
Size	Total light content in a cleaned image. It is used to get an estimation of the gamma-ray energy.
Width	Lateral extension of the air shower, minor axes of the ellipse.
Length	Longitudinal extension of the air shower, major axis of the ellipse.
Distance	Angular distance from the centroid of the ellipse to the center of the camera.
Alpha	Angle that determines the orientation of the ellipse, formed between the major axis of the ellipse and the distance parameter.

Table 3.1: The Hillas parameters definition.

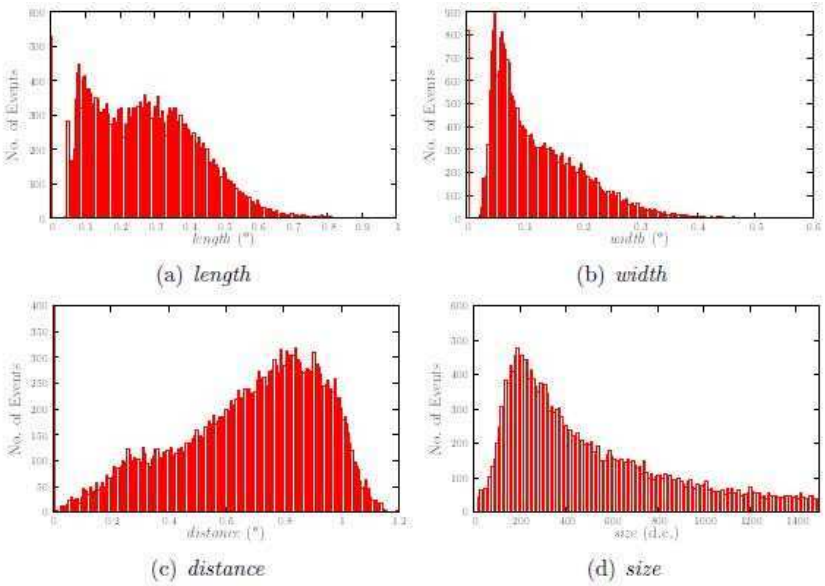

Figure 3.14: Hillas's parameter distributions for a 28 minute run of Crab Nebula. Figure taken from Toner (2009).

The recorded images are fitted with the Hillas parameters and analyzed for selecting gamma-ray events from the target source. The hadron images are isotropically distributed around the FOV and generally have larger values of alpha. Another parameter used for the rejection of hadronic showers is *width*, images produced by gamma-rays being more compact than those produced by hadronic showers. In the case of muons, they tend to produce a ring-like or arc images in the focal plane. An example of each type of image recorded by the Whipple telescope is shown in Figure 3.16.

In 2000, after the major upgrade to the Whipple camera, the data for that season were analyzed using the standard 2nd-moment-parameterization technique

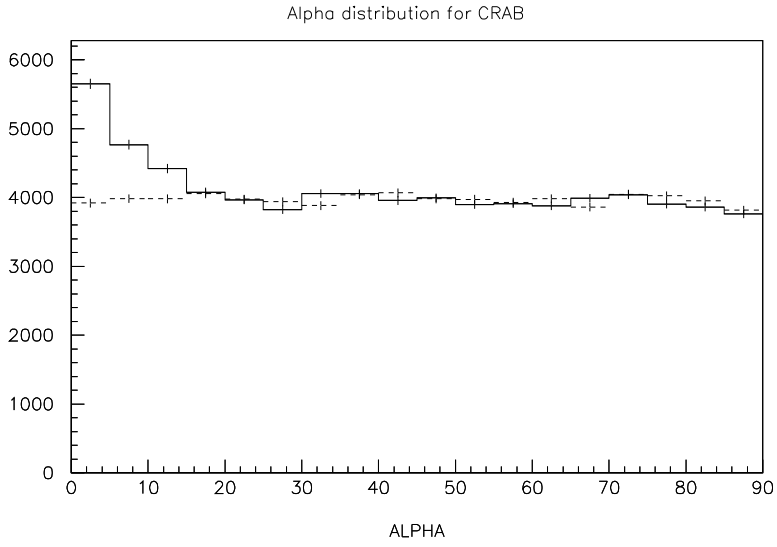

Figure 3.15: Alpha plot distribution for 18 hours of Crab Nebula data taken during 2008-09 season.

(Hillas 1985) and the optimized Hillas parameters cuts were found. These parameters maximized the gamma-ray significance above the background, looking for the highest gamma-ray signal-to-noise ratio for the Crab Nebula observations. Those cuts are called Supercuts 2000 and have been by default used to select γ-ray events and to suppress background cosmic-ray events (de la Calle Perez et al. 2003) for all the Whipple data since then. The optimization procedure and the results obtained for the 2007-09 seasons are discussed in Chapter 4.

Sometimes a hadronic shower may create an image that can pass all the selection criteria and be considered as a gamma-ray event. Also, it could be by chance that a noise-sky background fluctuation or a muon ring passes as a gamma-ray event. Therefore, it is important to quantify the probability that these kind of events are triggering as a gamma-ray event. A study of background events is also crucial to avoid biasing gamma-ray rate. Different methods are applied to estimate the background depending on the observing mode used (Horan 2001).

Good observing conditions are limited in time, so a strategy must be developed to achieve most of what is available. First, it is natural to minimize the amount of background light by observing only during the darkest times, when the moon is below the horizon. This means, periods of two to three consecutive weeks (depending on the season of the year) during which each night has at least three hours of observable sky. In July and August, during the summer, there is a complete shut down of observations due to the monsoon season in Arizona; and all the electronic components are powered off and disconnected in order to be protected from lightning storms. The criteria in determining the good quality of the data is to choose only observations under very good atmospheric conditions, such as no clouds passing through, wind less than 50 km/h and humidity less than 50 %.

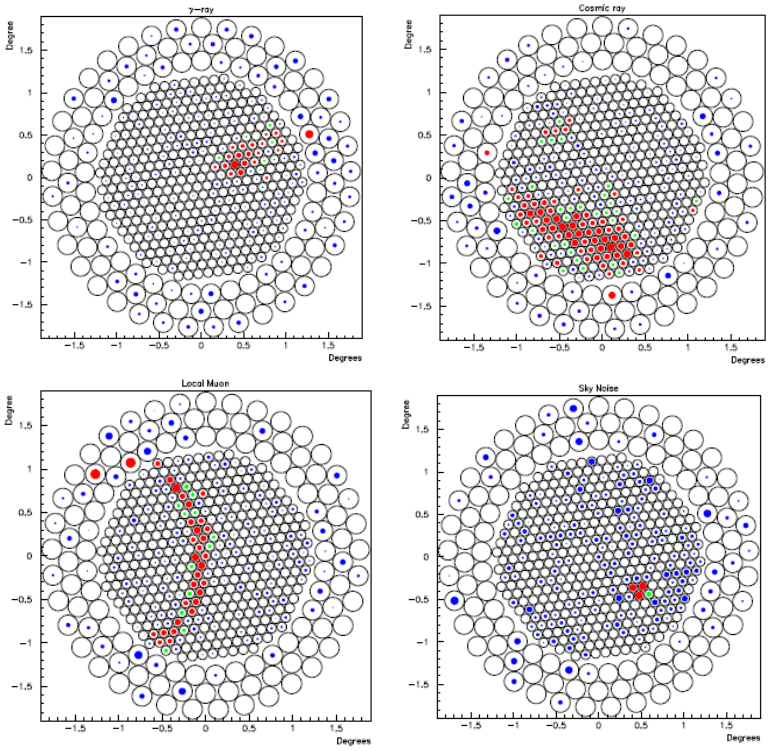

Figure 3.16: Images recorded by the Whipple 10 m telescope. The top-left corresponds to a gamma-ray event, the top-right to a cosmic-ray event, the bottom-left to an arc generated by a local muon and the bottom-right to an event generated by noise. Red pixels are the core pixels and the green ones are the boundary pixels. The blue ones are pixels that fail the *picture-boundary* criteria and are eliminated in another part of the analysis. Images taken from Dunlea (2001).

The observations may be conducted in two modes: ON/OFF and TRK (tracking). In the first case, the telescope tracks the source which is centered in the field of view for 28 minutes (ON run). The corresponding OFF run is collected at an offset of 30 minutes from the source's right ascension for a period of 28 minutes. The two runs are taken at the same declination over the same range of telescope azimuth and elevation angles. This removes systematic errors that depend on slow changes in the atmosphere. In this mode, direct background subtraction of cosmic-ray events in the ON run (as determined by the OFF run) is possible. So, the corresponding gamma-ray rate and the error (associated Poisson error), with the significance σ can be estimated as:

$$Rate = \frac{N_{ON} - N_{OFF}}{duration} \pm \frac{\sqrt{N_{ON} + N_{OFF}}}{duration} \tag{3.3}$$

$$Sig = \frac{N_{ON} - N_{OFF}}{\sqrt{N_{ON} + N_{OFF}}} \tag{3.4}$$

where N_{ON} is the events ON-source and N_{OFF} is the background OFF-source events.

This kind of observing mode is crucial for determining the presence of a new source (or to calculate an accurate flux upper limit) and/or for estimating the energies and making the spectral reconstruction of the primary gamma-rays. The disadvantage of this method is that 50 % of the time is spent in observing the background, reducing the duty cycle of the telescope to half.

In the TRK mode only ON runs are taken with no corresponding OFF observations. TRK mode is useful for monitoring the variability of well-established sources. The background is estimated from events whose major axis points are away from the center of the camera. TRK observations are also taken when the sky is possibly cloudy. Clouds in the field of view are noticeable from fluctuations in the cosmic ray rate. An OFF run is, in this case, not possible as the background rate is changing. Often, data are taken in a mixed mode, ON-OFF runs are interspersed with TRK runs, to achieve the best balance between systematic and statistical errors. The ON-source *alpha* for a TRK run is taken as all the events in which the alpha value is less than $10° - 15°$ since the gamma-ray events are compact and coming for the center of the FOV. The background, OFF-source alpha, is also estimated for the TRK run (ON run) considering events with *alpha* in the $35° - 65°$ range. The calculation for the rate and significance is the same as in the ON/OFF method.

The analysis package used to study the rate coming from the sources was first developed in the University College Dublin, and it is called the *UCD* code. The author of this work developed part of the code once it was installed at the Whipple telescope. This code has been used as the official data analysis package from 2008 to 2011.

Each run, kept as a raw data file, includes all the information about each event that passes through the triggers. The UCD code is divided in several steps to analyze the raw data. The first step, called *xfastlook*, extracts all the information about the run (elevation, duration, number of events, etc.) and generates a change of data format to a Hierarchical Data Format (hdf). This output is used by the *xanalyze* step to perform the Hillas parameterization for each event and reject all the cosmic-rays, muons and noise events. Then, the *xcut* step allows only the selected events to pass a set of predetermined cut values. The final step is the *xtabout*, where a text and postscript file are generated with a summary of the results, with the significance, rate or upper limit for each run and for the total of the list of data files. The output includes the alpha plot distribution and all the information related to the source and the telescope operation during the observation time.

More detailed descriptions of Whipple observing modes and analysis procedures can be found in Punch & Fegan (1991), Reynolds et al. (1993), Weekes

(1996). Details about the Whipple telescope have been given in Kildea et al. (2007). Details about the calibration procedures of the Whipple 10 m, and the shower simulations to reconstruct the energy of the primary γ-ray are detailed in Chapter 4.

3.5 VERITAS

VERITAS is an array of four atmospheric Cherenkov telescopes located at the basecamp of the Fred Lawrence Whipple Observatory in southern Arizona at 1268 m of altitude (see Figure 3.17) (Maier et al. 2007). It is used to study astrophysical sources of gamma-ray emission in the energy range from 100 GeV to 30 TeV using the imaging atmospheric Cherenkov technique explained in section 3.4. The telescope design is based on Whipple 10 m telescope, with each of the four telescopes consisting of a 12 m diameter segmented reflector with a Davies Cotton design (see Figure 3.9). Each camera has a 499-pixel photomultiplier tube with a FOV of 0.15° each covering a total FOV of 3.5° at the focus (see Figure 3.18). The 354 hexagonal mirrors are attached to the 12 m diameter optical support structure (OSS) supported in turn by an elevation-azimuth positioner mount. The positioners have an accuracy of 0.005° and can be moved as fast as 1° per second (Holder et al. 2006).

Figure 3.17: The VERITAS array with the new configuration. Photo credit: S. Criswell, FLWO.

A coincident Cherenkov signal in at least 2 out of 4 telescopes triggers a readout of the PMT signals (see Figure 3.19) at a typical rate of 250 Hz. The resulting images in each camera are parameterized by their moments, and these parameters are used to discriminate gamma-ray initiated air showers from those initiated by cosmic-ray particles, and to reconstruct the energy and arrival direction of the primary photon. The angular resolution and energy resolution of the reconstruction is energy dependent, reaching 0.1° and $> 15\,\%$ for primaries with an energy of 1 TeV.

The sensitivity of the array can be quantified by the observing time required to detect a typical weak source. VERITAS sensitivity has improved over the years

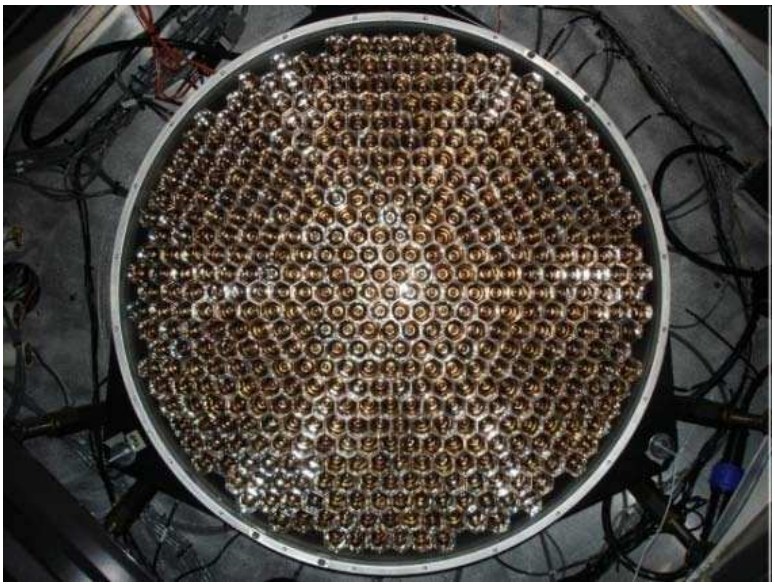

Figure 3.18: VERITAS camera with the 499 photomultipliers. Photo taken from http://veritas.sao.arizona.edu

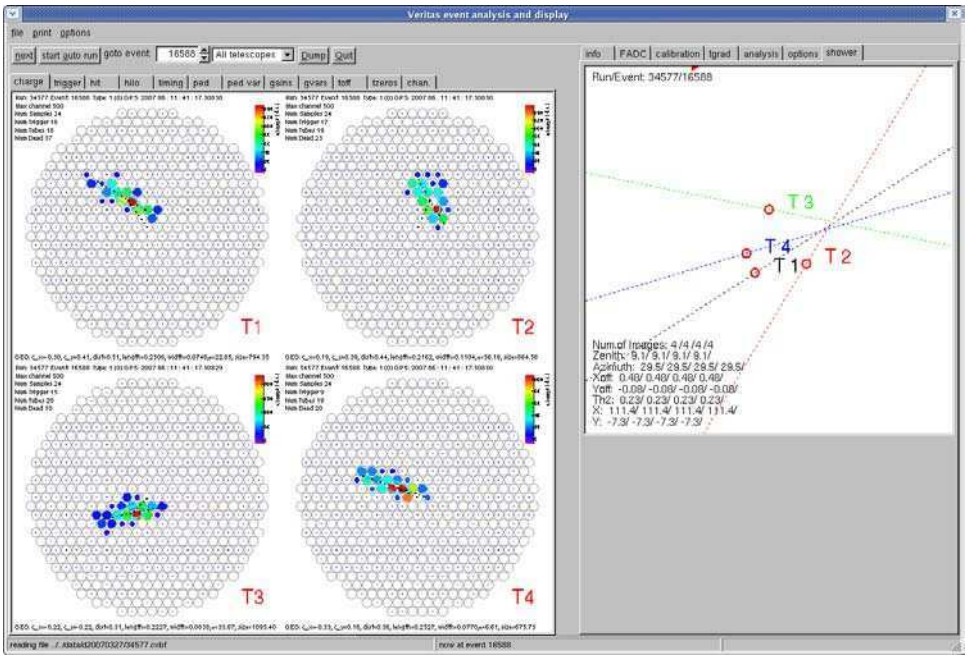

Figure 3.19: Example of a gamma-ray event in each telescope of the VERITAS array. The images are used to reconstruct the direction of the primary gamma-ray. The semi-major axis of each ellipse is extended and intersected at the shower core location. Archival VERITAS image.

due to improvements in data analysis techniques, optical alignment, calibration and, most significantly, by the relocation of the original prototype telescope to a better location in 2009. Currently, a source with a flux of 1 % the Crab Nebula flux and a spectrum similar to the Crab Nebula can be detected in approximately

25 hours of observations, half the time required when the array was originally commissioned. Approximately 1000 hours of data are collected every year, more than 20 % of the data are taken when the moon is visible.

Observations are performed (in 20 min runs) on moonless nights using the "wobble" mode of operation, in which all telescopes are pointed to a regular sky position offset of $\pm 0.5^{\circ}$ (alternating the direction, north-south-west-east between consecutive data runs) with respect to the source position. The offset is determined using simulations of the detector response; and may change depending on the source. This method allows performing simultaneous background estimations.

The observing conditions are similar to those presented before for the Whipple telescope. The main goal of VERITAS in terms of observing strategy is to observe sources under some moderate moonlight conditions, when the moon is less than half full and the source location is $\sim 90^{\circ}$ off the moon.

The importance of having stereoscopic or multi-telescope arrays is that the background can be reduced by placing coincidence requirements on events that are occurring at multiple telescopes. In addition, the energy resolution of stereoscopic systems is improved by unambiguously determining the position of the shower core by geometric arguments.

3.5.1 VERITAS Data Acquisition System

The VERITAS data acquisition system has three levels of trigger in order to record only gamma-ray events (see Figure 3.20). When a photon hits the PMTs, the electrical signal is sent to the Flash Analog to Digital Converter (FADC) boards, where it is kept until the trigger decision to discard or record the event is made. A Cherenkov pulse normally lasts less than 20 ns, and the process of either keeping it or not, takes less than 100 ns. For each camera with the 499 pixels, 50 FADC are used to record all the signals. The first trigger is called L1 and is at the pixel level, where the pixel has to detect more light than a threshold value. In order to do that, the signal is split into three parts: the first signal is checked against the threshold going to the Charge Fraction Discriminator (CFD), the second signal is inverted and delayed, while the third one is attenuated. The 2nd and 3rd signals are sent to the Zero Cross Discriminator (ZDC). It waits for the time when both pulses cancel each other, and then sends the information to the CFD. The L2 trigger (Pattern trigger) is made to avoid night sky fluctuations that could trigger the CFDs. This level triggers on groups of adjacent pixels (usually 3) triggered at the CFD within a certain time window (typically 6 ns). Having this small coincidence window, a large number of false triggers are eliminated. The L3 trigger (Array trigger) was designed to eliminate events generated by an isolated muon. Finally, an L3 trigger is generated when at least two telescopes trigger the L2 signals within a specified coincidence window that is usually around 100 ns. The L3 trigger is sent to all the telescopes and the event is recorded. During that time (dead-time) the trigger system is stopped (it is normally a 10 % of the time).

For each telescope, the shower data are transferred to the event-builder computer that combines the event information from the 4 VME crates (where all the FADCs are held), plus the time information (GPS clock) from the auxiliary crate,

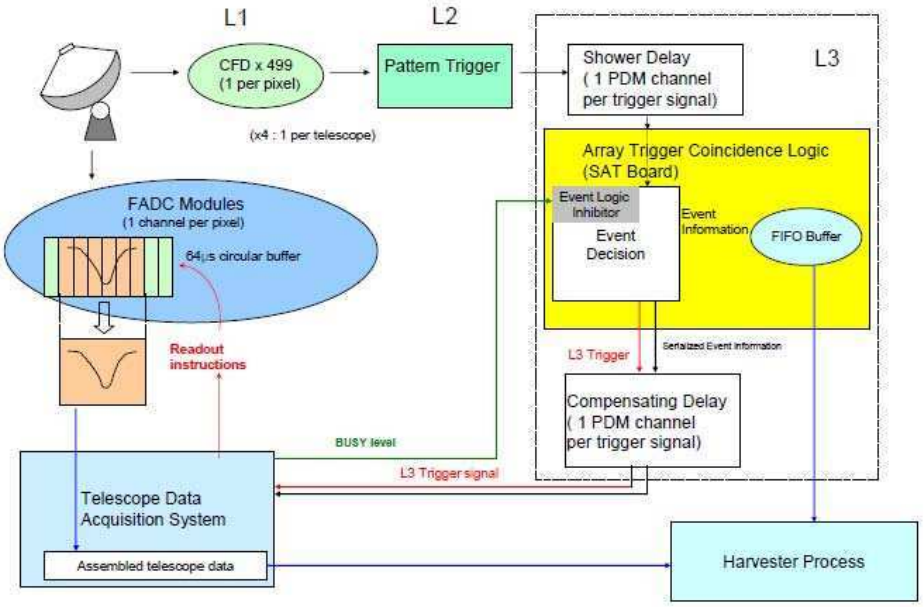

Figure 3.20: Schematic diagram of the VERITAS system trigger. Figure taken from Weinstein (2007).

into a telescope event file. This file is written to disk in a harvester-computer that assembles the telescope files into a single array file in the VERITAS Bank Format (VBF). The file is also compressed to 5 Gb per run and sent to the data archive, which can be used for offline analysis.

3.5.2 VERITAS Calibration and Simulation

A series of tests are performed on a regular basis in order to understand the behavior and to maintain the performance for all the telescopes.

Telescope pointing calibration is done once a month by imaging bright stars with the telescope's Optical Pointing Monitor cameras. The offset between the center of the star and the center of the camera is measured and applied as a correction to the telescope positioning at several values of elevation and azimuth. The resulting pointing accuracy is around 0.02 degrees.

It is important to collect as much Cherenkov light as possible, so a mirror alignment is crucial. The mirrors of the telescopes are washed once a month. The mirror alignment is carried at the beginning of the observing season and some other times when it is necessary (during periods with lack of observing time). In 2009, a new alignment system was developed at Mc Gill University (see McCann et al. 2009 for further information). This alignment considerably improved the PSF for each telescope, being very important for gamma-ray analysis as it improved the angular resolution for extended sources.

A bias curve is made in a dark patch of the sky, with similar elevation for the observations, in order to study the response of the CDF threshold to night sky

background, looking for the best value in which such events cannot be triggered.

Monte-Carlo simulations from photon- and proton-induced air-showers are made with CORSIKA (Heck et al. 1998) and KASCADE (Kertzman & Sembroski 1994). These simulated showers are then passed through a simulation of the detector in order to produce simulated data files as measured by the telescopes. The simulations are then analyzed through the data analysis package, where noise and pedestals are added to emulate real data, and finally the showers are processed through the reconstruction stages of analysis. In this case, the simulated data can be compared to real data and the effective collection area of the array can be calculated depending on the energy of the primary that initiated the shower, the zenith angle, night sky noise, offset of the gamma-ray source from center of the FOV and the cuts made on the data. Also, it is used to create the lookup tables needed to reconstruct the shower, find the energy estimated of the primary gamma-ray, the reconstructed location of the source, and to create the spectral energy distribution for that source.

3.5.3 VERITAS Data Analysis

The analysis of VERITAS data for this work was carried out using the VEGAS analysis package (see Cogan 2007 for further information). It consists of six stages. Stage 1 takes the raw data coming after the electronics and calculates all the needed calibration parameters, such as the pedestal calculation, the relative gain calculation, the high voltage, the current for the PMTs, the telescope information and the source data. Stage 2 consists of applying all the calibration constants to the raw data and generating the calibrated events. In Stage 3, the image is cleaned by using the *picture/boundary* technique (similar to the one explained above for the Whipple telescope), and the Hillas parameters (*width* and *length*) are obtained. In Stage 4, the parameters obtained are used to reconstruct the shower using Monte-Carlo simulations and to calculate the Mean-Scaled Width (MSW) and the Mean-Scaled Length (MSL) using lookup tables. Also, quality cuts are applied at this stage and only showers passing all the quality cuts can be properly reconstructed. In Stage 5, stereo cuts are applied to the MSW and MSL obtaining a dataset of gamma-ray events. The last stage, Stage 6, gives the results. It calculates the number of events in the source and background region and gives the excess events. The rate and the statistical significance of any excess is calculated using equations from Li & Ma (1983) and also the upper limits are given if there is no signal. Additionally, maps of significance, excess, spectrum are automatically given in this stage.

Chapter 4

Whipple Calibration Methods and Simulations

Since September 2005, when VERITAS started to be operational, the Whipple 10 m telescope has been used primarily to monitor known TeV AGNs. Markarian 421, H1426+428, Markarian 501, 1ES 1959+650 and 1ES 2344+514, the five blazars that have been previously detected at Whipple, are monitored each observable night they are visible. Several multi-wavelength campaigns were undertaken for almost all the five blazars during the last years and the results were presented elsewhere (e.g. Fortson & Kildea 2008, Horan et al. 2009, Pichel & Rovero 2008). The Whipple 10 m telescope is used as a trigger alert for VERITAS in case of enhanced activity from any of the sources being monitored is detected. It is important to have a dedicated telescope to get a long term monitoring of these sources in order to study their variability, searching for periodicity and to detect periods of highly-intense short-term variability (flares), as well as to put some constraints into the emission models. After VERITAS was fully operational in 2007, the Whipple 10 m telescope was adjusted and recalibrated in 2008.

This chapter describes the applied calibration methods and simulations generated for the Whipple 10 m observations during 2008-09. Section 4.1 outlines the measurement techniques used to calibrate the brightness of the recorded Cherenkov images. Section 4.2 describes the sample of air showers and detector simulations used in the energy reconstruction routines implemented in this work for the Whipple 10 m data. Finally, Section 4.2.2 shows the simulations applied to the Crab Nebula observation taken by Whipple during the 2008-09 season.

4.1 Whipple Calibration

The image brightness of Cherenkov events measured by IACTs is affected by atmospheric conditions, the telescope's optical system (mirror and light cone efficiencies), and the gain at the camera. As a first step, the camera was flat-fielded to correct for the non-uniform response of pixels across the field of view. The measured gain in the camera was then used to convert the Cherenkov signal from digital counts to photoelectrons. The time dependent efficiency of the optical sys-

tem and PMTs in the camera were determined by comparing the intensity of muon events to the expected intensity from simulations. Finally, an overall detector efficiency was defined in this work, which is relative to the nominal gain at the time when the camera was installed in 1999.

4.1.1 Flat-fielding System and Pointing Corrections

High voltages in each pixel were adjusted at the beginning of the season in an iterative flat-fielding process to obtain a relatively uniform response across the camera. Nevertheless, pixel gains after this process were slightly different, being initially spread around 5 % and corrected every night with a 4 minutes run using diffuser light pulses from a laser. The laser was located inside the telescope control building, from which light pulses were transmitted by fibre-optic cable to illuminate a diffuser fixed at the center of the reflector, facing the PMT camera. The fast pulses illuminated the camera with a nearly uniform light intensity. Thus, relative gains for each pixel were determined. The laser calibration runs are generally taken with the telescope in its stow position, but they can be taken at any elevation provided there are dark patches in the sky with no bright stars in the field of view.

The pointing monitor is an important calibration instrument which was reinstalled on the Whipple 10 m telescope in 2008. It consists of a CCD camera mounted at the center of the OSS viewing the PMT camera. Also, four LEDs were installed fixed in the focal plane, allowing the center of the PMT camera to be precisely located in the CCD images. The pointing monitor was used to find the pointing offset of the telescope in order to apply corrections to the data. It was also used to perform PSF and bias-alignment measurements. It is crucial to have the telescope pointing directly to the source (with no offset present due to positioning problems), to keep most of the gamma-ray events after selection, when the cut in the *alpha* parameter is applied ($\alpha < 10^{\circ}$ to $10 - 15^{\circ}$, see Figure 3.15). This assumption is not entirely correct when the pointing error is taken into account, having the *alpha* peak for bigger values, in which some gamma-ray events are considered as background events and are rejected.

In order to test the pointing position, a white screen was placed in front of the PMT camera and CCD images of bright stars were taken under different elevation and azimuth angles (see Figure 4.1).

For each bright star, the telescope was moved using the elevation-azimuth positioner until the center of the star and the center of the camera were in the same position. The offsets in elevation (y_{off}) and azimuth (x_{off}) were recorded into a file. This procedure was made several consecutive nights in order to find the dependence of the offsets as a function of the elevation and azimuth of the telescope. Both x_{off} and y_{off} were found to be correlated with the elevation angle (see Figure 4.2), having no clear evidence of correlation with the azimuth position of the telescope (see Figure 4.3).

The offsets were fitted with a linear function for elevation and a polynomial of second degree for azimuth. The results were introduced in the *whipple.c* routine inside the UCD analysis in order to properly correct the position of the center

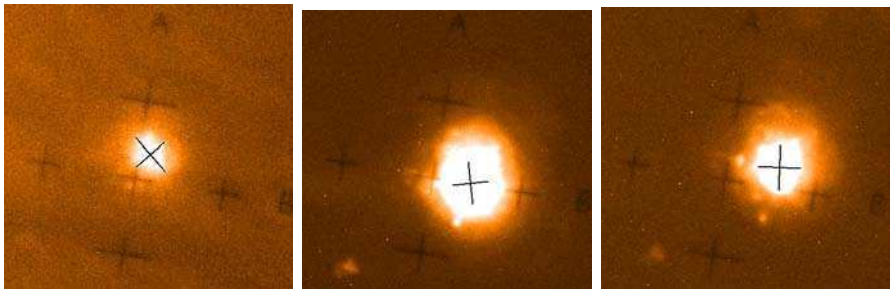

Figure 4.1: Bright star images at the focal plane of the Whipple 10 m. The cross on the center of the four crosses (positions of the LEDs) is the center of the camera. *Left*: Polaris at 31° of elevation and 0° of azimuth. *Middle*: AlphaUma at 60° of elevation and 358° of azimuth. *Right*: DeltaLeo at 78° of elevation and 206° of azimuth.

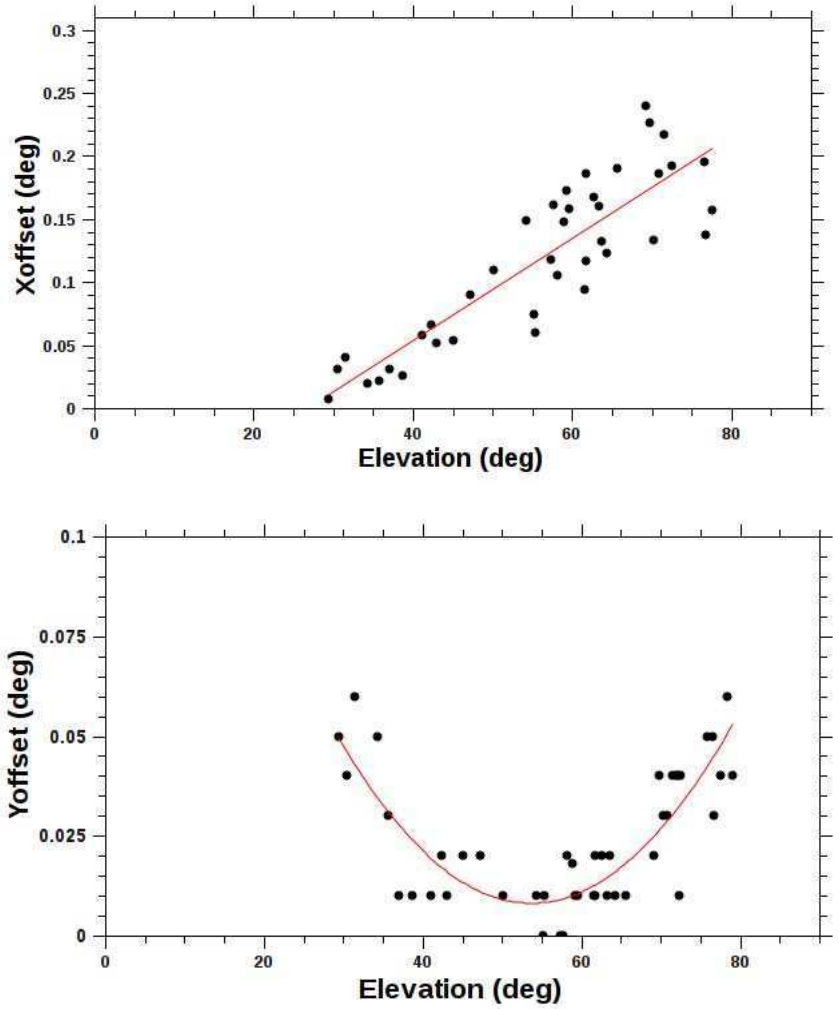

Figure 4.2: Stars offsets as a function of elevation for the 2007-08 observing season.

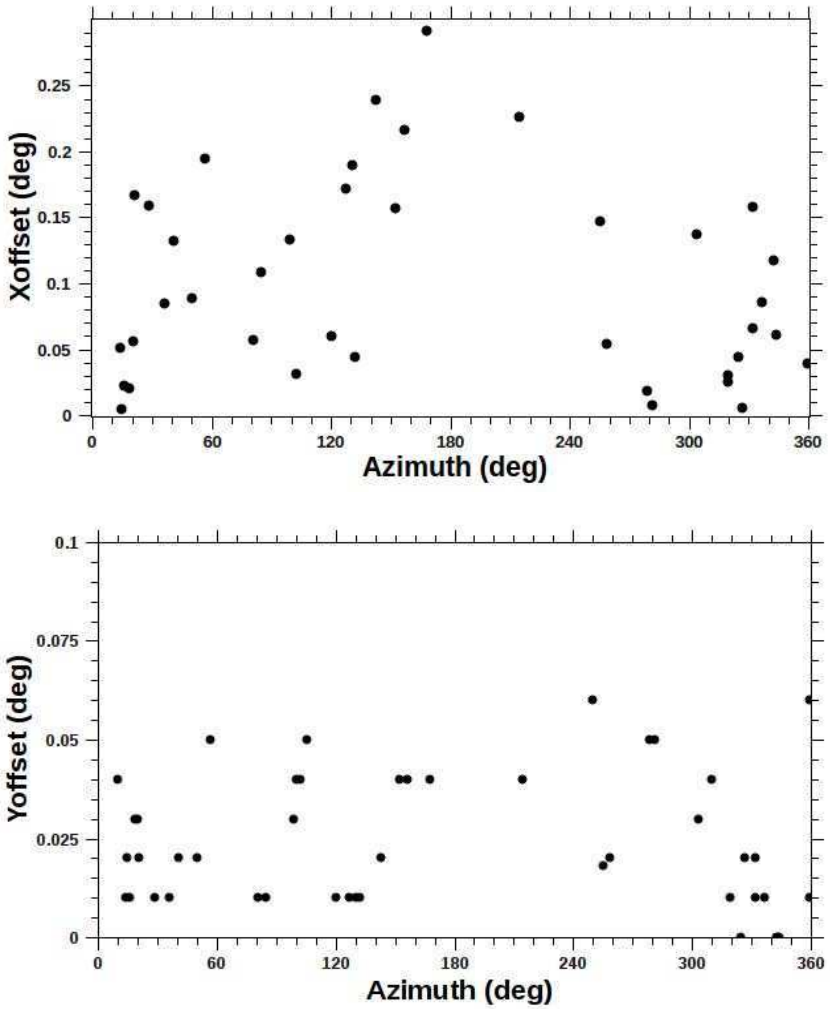

Figure 4.3: Stars offsets as a function of azimuth for the 2007-08 observing season.

of the camera. In this way, the mis-pointing of the telescope was corrected and, consequently, the results of the analysis were improved, having more events with $\alpha < 3°$. An example of this correction is depicted in Figure 4.4, in which the results of 1.8 hours of observations taken from Mrk 421, during a night in April 2008, are shown as alpha plots (see section 3.4.1). It can be noticed that in the first plot, the peak was located in the second bin with $3° < \alpha < 6°$. After adding the pointing corrections, the same data were re-analyzed and the results showed the peak in the first bin with $\alpha < 3°$. Thus, the pointing corrections were left inside the code and the data for the season were re-analyzed.

A checking procedure was made every night during observations in order to test the pointing corrections. When an observing run was finished, before moving the telescope to another target, the telescope was slewed to a near bright star and the readings from the anode current monitor were recorded. If the corrections applied before were working properly, the central PMT would have the maximum current.

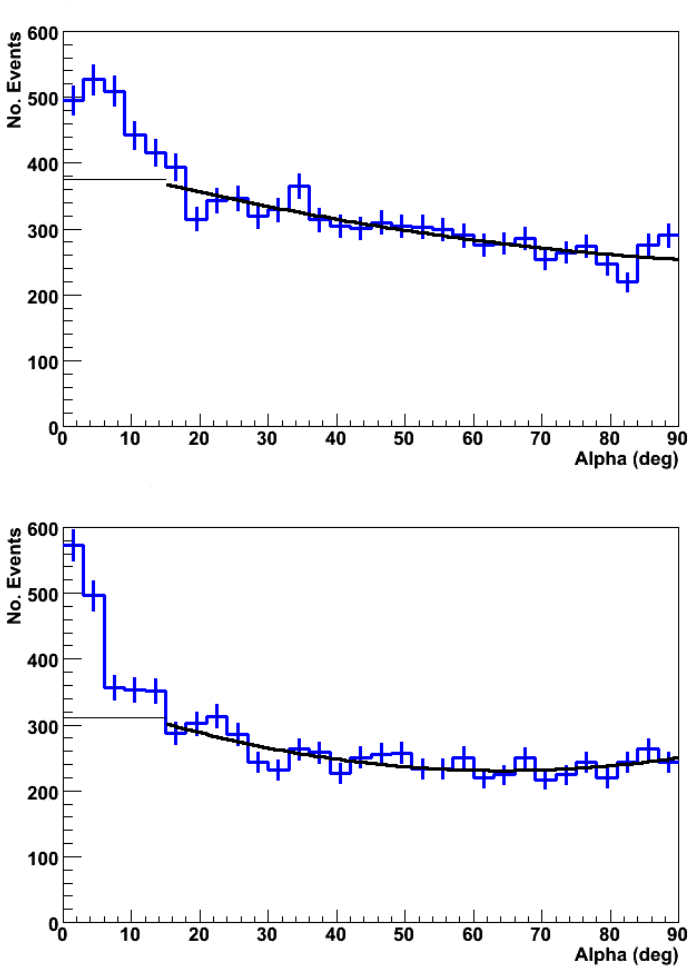

Figure 4.4: Alpha plots for Mrk 421 without (*top*) and with (*bottom*) pointing corrections applied.

If the telescope were mis-pointed, not the central but some of the adjacent PMTs would have the maximum reading.

An alternative method to correct the mis-pointing of the telescope for old data was proposed and developed (Kildea 2008). The basic idea was taken from Akerlof et al. (1991) and then improved. The apparent source location, finding the common intersection of the major axes of the images, was created from gamma-ray events, after hadronic rejection. Given this scenario, a 2D histogram was drawn, plotting all the lines for the major axis of every image that passes all the cuts. Then, the bin with more intersection lines was naturally built up (see Figure 4.5). For a strong source such as Mrk 421 or Crab, where the source was tracked at the presumed center of the camera, there should be no need to do any derotation of the lines, and the hotspot in the 2D histogram should correspond to the position of the source in the camera. The distance of the hotspot to the center of the camera should give the pointing correction. If applied over a range of elevations, it should be possible to determine the pointing corrections from real data. This

would also be useful for old data where the pointing monitor was not installed.

To test this method, 2.5 hours of Mrk 421 data in high state of activity which had a large set of gamma-rays was analyzed by using the standard method and the line analysis was applied to the ON and OFF data (see Figure 4.5). A 2D histogram of event lines were produced with and without pointing corrections applied. The resulting plots are shown in Figure 4.6. It can be noticed that the hotspot is on the left of the camera center for the non-corrected data whereas it is in the center for the pointing-corrected data, being the displacement $\sim 0.3°$ for an elevation of 40°.

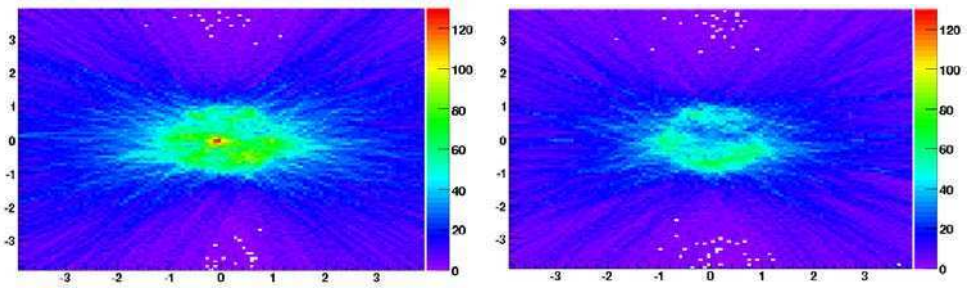

Figure 4.5: 2D histogram of event lines for the *on* (*left*) and *off* (*right*) data distribution corresponding to 2.5 hours of Mrk 421 during the big flare observed on May 02, 2008 with the Whipple 10 m.

Figure 4.6 shows in the bottom panel that the method works very well. It can be noticed that, after applying the pointing corrections, the position of the hot spot and the camera center are the same. This can be used then to examine Crab data and possibly any other older data in which there were no pointing corrections from stars. Possibly, the line analysis method would be useful to correct archival data and to improve sensitivity, combined with another calibration methods.

4.1.2 Optimization of image cuts

Since the last upgrade of the camera in 1999, a new set of cuts have been optimized to get the maximum significance. Those cuts were named Supercuts 2000 and were the standard cuts that have been applied since then.

For the data taken in the period 2008-09, an optimization method was performed to find a new set of cuts, using the ON/OFF runs from Crab observations for each season. There were several methods tested in the past for Whipple data to find the best optimization for each cut, such us the grid search method (Quinn 1997) and the simplex method (Moriarty et al. 1997). In this work, the single parameter variation method (Quinn et al. 1997) was used. The method consists of choosing a plausible starting value for each parameter before the optimization procedure begins. The algorithm then searched for the best value of a cut, one at a time, by keeping constant all the cuts except the one under optimization.

The peak in a plot of gamma-ray significance versus cut value for the cut under optimization represents its first best-estimated value. Once the best-estimated

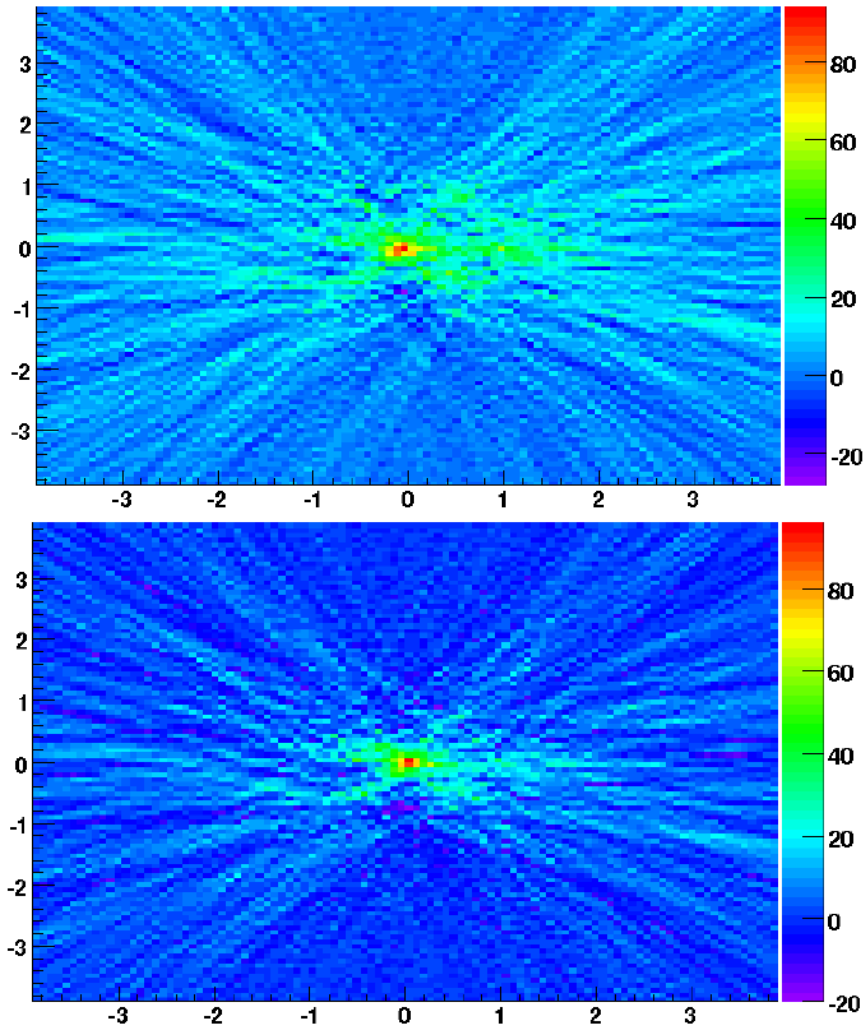

Figure 4.6: 2D histogram of excess (ON-OFF distribution) event lines of Mrk 421 without (*top*) and with (*bottom*) pointing corrections applied.

value for each cut was found, those values were taken as the starting ones, and the same process was repeated again. It was found that, after three iterations, the cuts converge into the optimized ones. Table 4.1 shows the optimized cuts for the 2008-09 season. The gamma-ray significance versus parameter-value plot for a trial optimization over all *size* values is presented in Figure 4.7. It can be noticed from the plot, that each parameter has a maximum significance and afterwards decreases. The maximum significance for each parameter was considered the optimized value.

For the 2008-09 season, 12 stable ON/OFF pairs of Crab data were used to find the best value for each cut. After the analysis, those 12 pairs were set aside and not used for the remainder of the analysis. Then, the rest of the Crab data (43 ON/OFF pairs) from the season were analyzed with the Supercuts 2000 getting a $18\,\sigma$ and re-analyzed again with the new set of cuts, showing a better result for the total significance by a 30 % ($24\,\sigma$). The same procedure was used for all the

Parameters	2008-9 season
Size	0-99999
Trigger	92-86-66
Frac3	0-1
Width	0.02-0.13
Length	0.13-0.24
Length/Size	0-0.0002
Distance	0.13-0.92
Alpha	0-10

Table 4.1: Optimized cuts for season 2008-09.

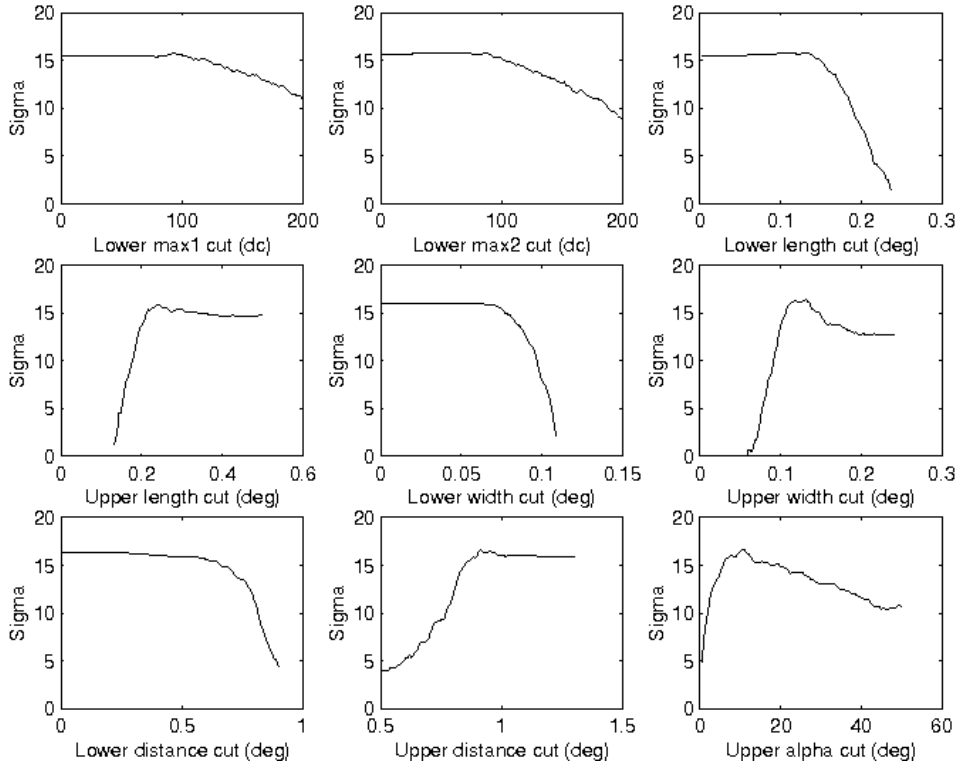

Figure 4.7: Significance of γ-ray excess versus Supercuts selection cut, from the re-optimization of Supercuts over all *size* values.

data of Mrk 421 and Mrk 501, getting improvements of 18 % and 5 %, respectively.

The *alpha* cut of 10°, given by the single parameter variation method, is considerably lower than the nominal value of 15° used in Supercuts 2000 (although it has to be noted that the bin width for the alpha plot is 5°). This fact, and a smaller value of *length/size* were the main differences between the optimized

parameters cuts used to analyze the 2008-09 data and Supercuts 2000; and was due to the fact that the cuts were optimized for maximum significance.

4.2 Whipple Simulations

The energy spectrum of a source offers an important insight into the processes responsible for the emission of VHE gamma-rays.

The flux and energy spectrum from a gamma-ray source are calculated from the number of selected excess events using the effective area of the instrument. The methods employed for the Whipple 10 m are verified in section 4.2.2 by comparing the measured gamma-ray flux and energy spectrum of the Crab Nebula from observations during 2008-09. The energy spectrum from the Crab Nebula was reconstructed and compared with old observations.

Monte Carlo simulations are crucial for data analysis of VHE gamma-ray observations as they are used for the reconstruction of the primary gamma-ray energy. Simulated gamma-ray images have to be similar to the real ones in a very high degree of precision in order to obtain the correct image parameters to be compared with the real data.

4.2.1 Whipple 10m Spectral Reconstruction

It is possible to obtain the energy for the primary gamma-ray due to the fact that Cherenkov light is a very good calorimetric component of the atmospheric particle shower.

The first step to achieve the energy reconstruction is to create Monte Carlo simulated gamma-ray showers, with as many similar observing conditions as possible, and then to compare to the ON/OFF Crab data for the same observing time and season in order to check if the simulations are correct and to adjust the free parameters.

In this work, a set of 100,000 Monte Carlo gamma-ray showers were simulated at a elevation angle of 70° and azimuth of 45°. A power law energy spectrum using equation 1.2 was used with $\Gamma = 2.5$ in an energy range from 100 GeV to 20 TeV. The air-showers were evenly spread over a circular radius of 300 m from the detector.

The KASCADE package (Kertzman & Sembroski 1994) was used to generate the simulated gamma-ray showers. The showers were tracked until they fell below the threshold for production of Cherenkov light. The primary gamma-ray energy was reconstructed from the measured amount of light and the impact distance for each observed shower. The simulated gamma-rays were used to calibrate the dependence between those quantities; a decrease in the calculated shower intensity means that the measured gamma-rays will be reconstructed with higher energy. As the Earth's magnetic field affects the lateral distribution of charged particles in the shower (and so that of the Cherenkov photons), a simple scaling (total Cherenkov light vs. distance) cannot be derived by just looking at one energy and impact distance.

The output from the KASCADE air showers were processed through the Whipple 10 m configuration contained within the GrISU [1] detector simulation package. This package consists of tracing the Cherenkov photons to the front of the PMT, followed by the production and propagation of the photoelectrons through the analog/digital electronic chain. The optics and the electronics are also modeled. For more information about the simulation processes see Schroedter (2004).

The effective area *A(E)* of the Whipple 10 m telescope is determined by the efficiency of collecting air-shower Cherenkov photons and is defined as:

$$A(E) \;=\; \pi\, R^2\, \frac{N_{\rm trig}(E)}{N_{\rm sim}(E)} \tag{4.1}$$

where $N_{\rm sim}(E)$ is the total number of simulated γ-rays, $N_{\rm trig}(E)$ is the total number of events that cause a trigger in the telescope at a given energy E. Simulated gamma-rays were used to calculate the effective area as a function of energy E and the telescope efficiency (which is tucked inside of $N_{\rm trig}(E)$). $R = 300$ m is the maximum impact distance centered on the telescope considered in the simulations.

Figure 4.8 shows the effective area for the Whipple 10 m telescope, obtained with simulated γ-rays as described above. The effective area has a correct performance for the energy range going from 400 GeV to 10 TeV, having a maximum effective area at 1 TeV with a value of $\sim 6 \times 10^4$ m^2. The energy threshold of the Whipple telescope is conventionally defined as the peak of the differential gamma-ray rate of the source convolved with the effective area curve of the detector. According to this definition, the threshold is 450 GeV.

The energy of the primary gamma-ray may be estimated by using a polynomial function that is dependent on the log of the image *size (S)* and *distance (D)* parameters of the shower. The energy estimator $E_{\rm est}$ can be written from the polynomial equation (Mohanty et al. 1998), as:

$$\log(E_{\rm est}) \;=\; a_1 \;+\; a_2 \log(S) \;+\; a_3 D \;+\; a_4 \log(S)^2 \;+\; a_5 D^2 \;+\; a_6 D \log(S) \tag{4.2}$$

The coefficients of this polynomial, a_i, were found by fitting the true energy of a large set of simulated gamma-ray events, comparing them to observational data. The energy resolution is the probability distribution for measuring an energy $E_{\rm est}$ when the true energy is E. This is measured from Monte Carlo simulations by comparing the true energy with the estimated energy. As an example, in the top plot in Figure 4.9 the result of the energy estimated for simulated γ-rays at 70° of elevation during the 2008-09 observing season is shown. The energy resolution in logarithmic energy-space shows a good reconstructed process, where the true energy and the reconstructed one are quite similar. The middle plot of Figure 4.9

[1] Grinnel-ISU is a package of programs for simulating the development of atmospheric showers and the response of the telescope to them. It was developed at the Iowa State University. The package also includes a data analysis program to process the data generated by the detector model. http://www.physics.utah.edu/gammaray/GrISU/

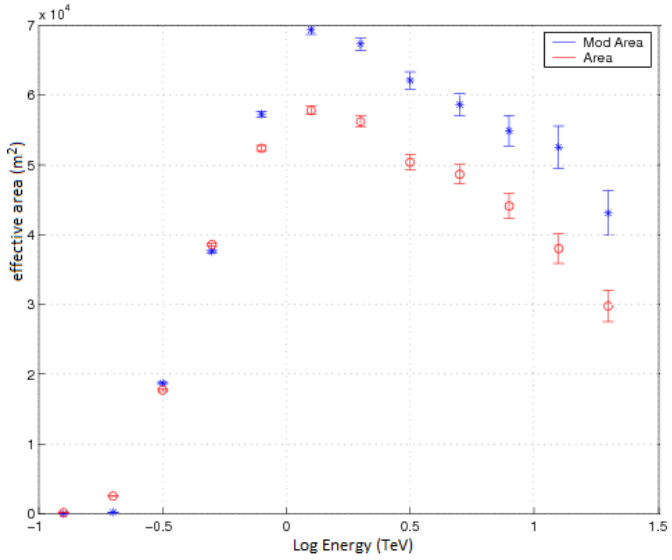

Figure 4.8: Effective area (*red circles*) and modified area (explained in section 4.2.2) (*blue stars*) for simulated gamma-rays at 70° of elevation as a function of the estimated energy.

shows the residuals $\log(E_{\rm est}) - \log(E)$ which were close to zero, showing that the estimation of the energy was correct. In the bottom plot of Figure 4.9, the mean and RMS difference are shown against energy. It can be noticed that the energy resolution varies slowly with energy and that the energy bias is less than 1 %.

Using equation 4.2, the energy for each event is calculated. The aim is to obtain the spectral energy distribution for the total number of events. The standard method to reconstruct the gamma-ray spectrum is to assume a power-law distribution, as equation 1.2., and fit it to the measured flux.

In some cases, like Mrk 421, an evidence of a high-energy cutoff was observed and then, this distribution is used to fit the measured flux:

$$\frac{dN}{dE} = F_0 \times 10^{-7}\ (E/1\ \mathrm{TeV})^{-\Gamma_{\rm VHE}}\ \exp(\mathrm{E/E_0}) \quad \text{photons m}^{-2}\ \text{s}^{-1}\ \text{TeV}^{-1} \qquad (4.3)$$

where E_0 is the high-energy cutoff.

In order to find the best-fit spectrum a grid search was made over possible values of F_0, E_0 and $\Gamma_{\rm VHE}$ (equation 4.3), determined by comparing the measured energy estimator distribution to the simulated one. If the simulated spectrum differed from the measured one, a new spectrum was simulated, equal in shape to the measured one, and the analysis repeated. The statistical error in the fitted power law was determined by the χ^2 method, in which the flux normalization and spectral index were varied according to their optimum value, until the desired increase in χ^2 was reached (Avni 1976, Lampton et al. 1976). So, a χ^2 map was produced including the probability content determined by the cumulative χ^2

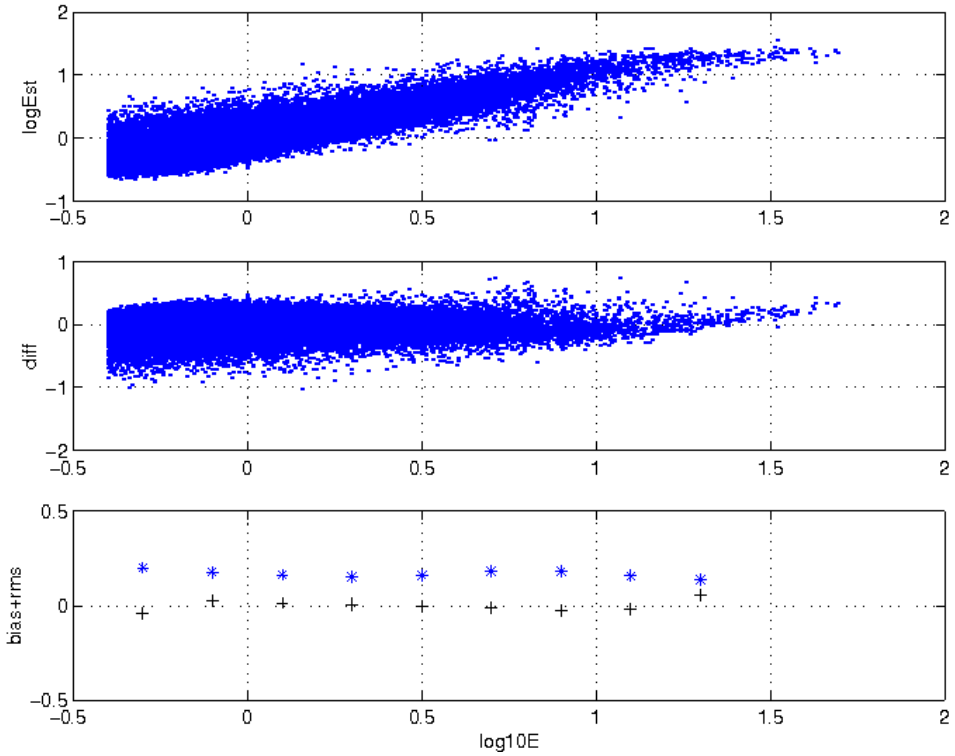

Figure 4.9: *Top*: Estimated energy vs. true energy of simulated events. *Middle*: Residuals of the fit. *Bottom*: RMS deviation of $\log(E_{\mathrm{est}}) - \log(E)$ shown by (*) and bias (+).

distribution with two degrees of freedom, with different confidence levels: 68.5 %, 90 % and 95 %.

4.2.2 Results from Crab Nebula Observations

The Crab Nebula is considered the Standard Candle in the VHE gamma-ray domain as its TeV gamma-ray emission (rate) is constant over time. It was used in this work to check the simulations and monitor stabilities of the system.

The data were analyzed by using the standard 2nd-moment-parameterization technique (Hillas 1985). Standard cuts (SuperCuts2000) and optimized cuts were used to select γ-ray events and to suppress background cosmic-ray events (de la Calle Perez et al. 2003). Using the zenith angle dependence of a Crab data set taken at similar epoches, the zenith angle dependence of the γ-ray excess rate was accounted for by normalizing the measured rate to the Crab rate at a corresponding zenith angle. It should be noted that this simplistic scaling is strictly valid for a TeV spectrum that is close to that of the Crab Nebula (spectral index of $\Gamma = 2.5$). However, the systematic error introduced by this scaling can be expected to be small compared to the statistical error of the flux points.

Observations of the Crab Nebula taken with the Whipple 10 m telescope during the 2008-2009 season were compared with the results from VERITAS and H.E.S.S.

in order to test the Whipple 10 m spectral analysis methods developed in this work. Only observations under good atmospheric conditions and with zenith angle less than 40° were analyzed. A total of 37 ON/OFF pairs were selected from December 2008 to March 2009, gathering a total of 16.3 hours. The overall significance of the 37 pairs was 24.9 σ showing more than 1500 excess events. The light curve from the Whipple 10 m observations is presented in Figure 4.10. The rate was steady during the observation time, so a constant fit was done, obtaining a best value of 2.54 ± 0.10 gamma/min with a reduced χ^2 of 1.433 (plotted with a dashed line).

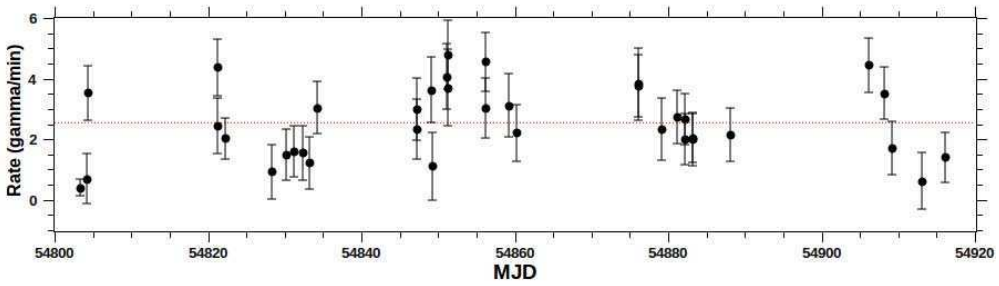

Figure 4.10: Light curve of the Crab Nebula taken with the Whipple Telescope from 2008-2009 season. The dash line is the best fit to a constant rate.

Histograms of several image parameters for the measured raw ON and OFF data sets in 2008-09 observing season are shown in Figure 4.11. While events in the raw data are mostly due to cosmic rays, the gamma-ray signal is very strong and an event excess in the ON data is visible for*alpha* $< 20°$ and to some extent in the *length* and *width* histograms as well. To increase the signal-to-noise ratio, a set of optimized cuts (see Table 4.1) was applied to reject more background events. After that, the gamma-ray excess is clearly visible as it can be seen in Figure 4.11 (thin lines).

For the simulations to be useful, it is necessary to verify that the simulated images are an accurate representation of the data. In order to do that, after applied cuts, the measured gamma-ray excess was compared to simulations as shown in Figure 4.12. The histograms show the distribution of the image parameters *alpha*, *width*, *length* and *distance* for the available data of the Crab Nebula during 2008-09 season. The simulated gamma-ray excess (ON-OFF differences) was normalized to the total number of events in the ON-OFF histogram. If there is a good agreement between the data and the simulations, then the Crab spectrum is generated. If not, the *max3* cut has to be adjusted until the *alpha* distribution is relatively unbiased (peak near $\alpha \sim 0°$ and flat with average around 0 for $\alpha > 20°$). In the case of the 2008-09 Crab data, the *max3* cut was raised to 65 digital counts (dc) so that the *alpha* plot was not biased towards negative fluctuations in the region $\alpha > 20°$. The image parameters derived from simulated gamma-rays (lines in Figure 4.12) were compared to the observed data (crosses in Figure 4.12) and it can be seen that both distributions match well.

The energy of an event is calculated from the *size* and *distance* using equation 4.2. Thus, small differences in other parameters between simulations and measured

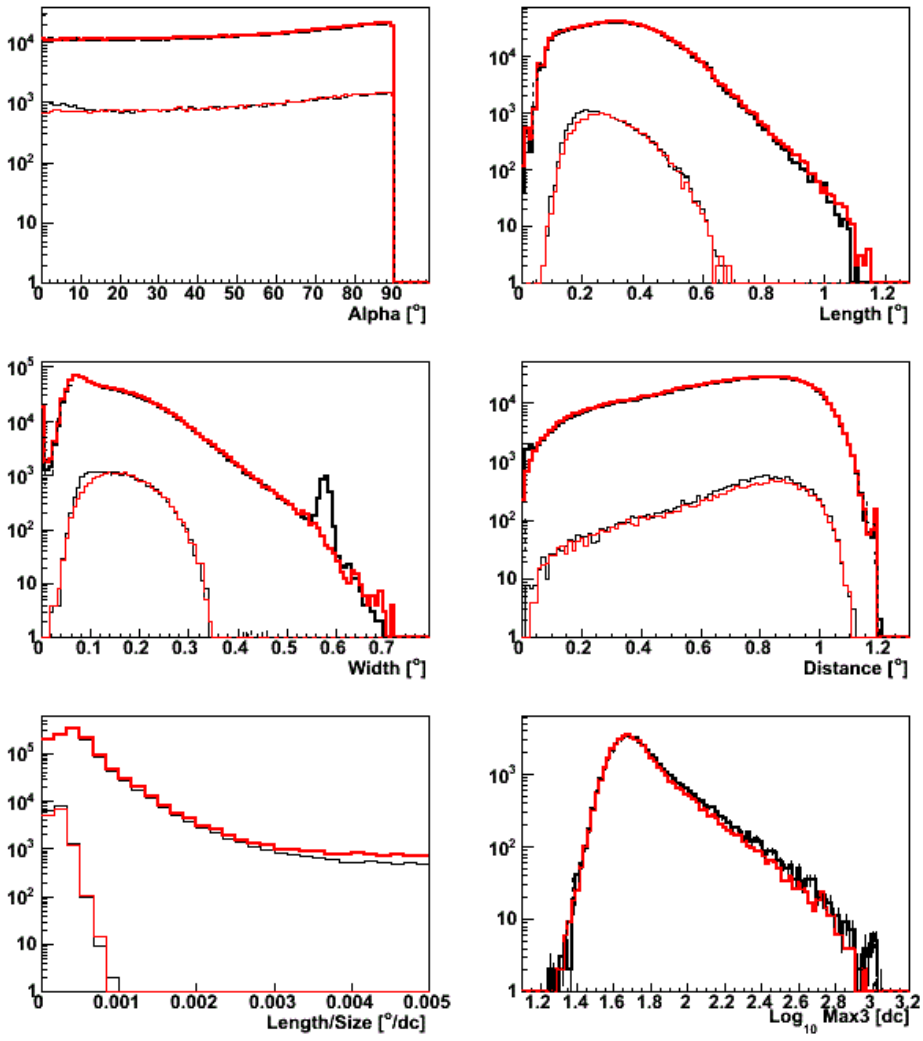

Figure 4.11: Histograms of parameters derived from raw data (bold) and after applying the optimized cuts (thin). ON data are shown in black and OFF data in red.

gamma-rays has no influence on the energy reconstruction.

Figure 4.13 illustrates how the distributions of the parameters derived for simulations depend on the image *size*. The parameter distributions are equally space-binned in log(*size*), and the mean and standard deviation for each bin were calculated. Both sets of values were fitted with a second order polynomial with a 2σ tolerance in which 85 % of the simulated gamma-rays pass all cuts. It can be noticed that the model fit cannot reproduce well the data for high values of log(*size*). This could be explained as a lack of statistics for the high-energy simulated gamma-ray events. As the parameter distributions derived from simulations are not independent of *size*, then the fit obtained is taken as a measurement of the dependence, which is used to reject cosmic-rays events.

Thus, the ON/OFF and the simulated data passed through all the same analysis steps. The comparison between real and simulated excess events is shown in

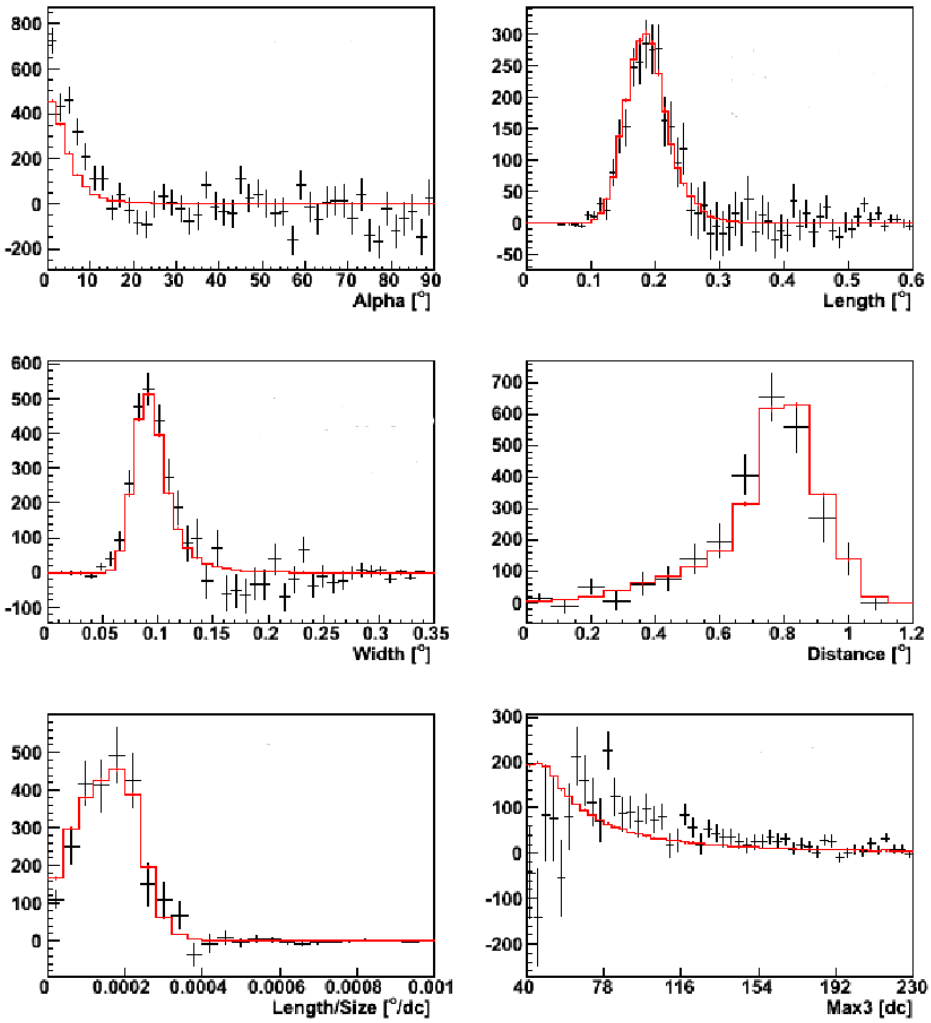

Figure 4.12: Histograms of the ON-OFF differences in the cut parameter distributions (crosses with error bars). Simulations of gamma-ray (line) are normalized to the total count of the difference histogram.

Figures 4.14 and 4.15. In Figure 4.14 histograms of the measured and simulated events are shown for the parameter distributions of *alpha*, *width* and *length*. It can be seen that there is a good agreement between the distributions. Figure 4.15 shows the histograms of the $\log(size)$ and $\log(E_{\mathrm{est}})$ distributions for simulated and measured events, where it can be seen that both distributions match well. These are two important plots to check if the reconstruction process works well.

After comparing the simulations to real data and checking that the methods and reconstruction worked properly, the last step before energy reconstruction was to calculate the estimated energy and the values for the modified effective area that are presented in Figure 4.8. The fall in the effective area at high energies is due mostly to the upper *distance* selection cut, which rejects high-energy air-showers at large impact parameters detected close to the camera edge.

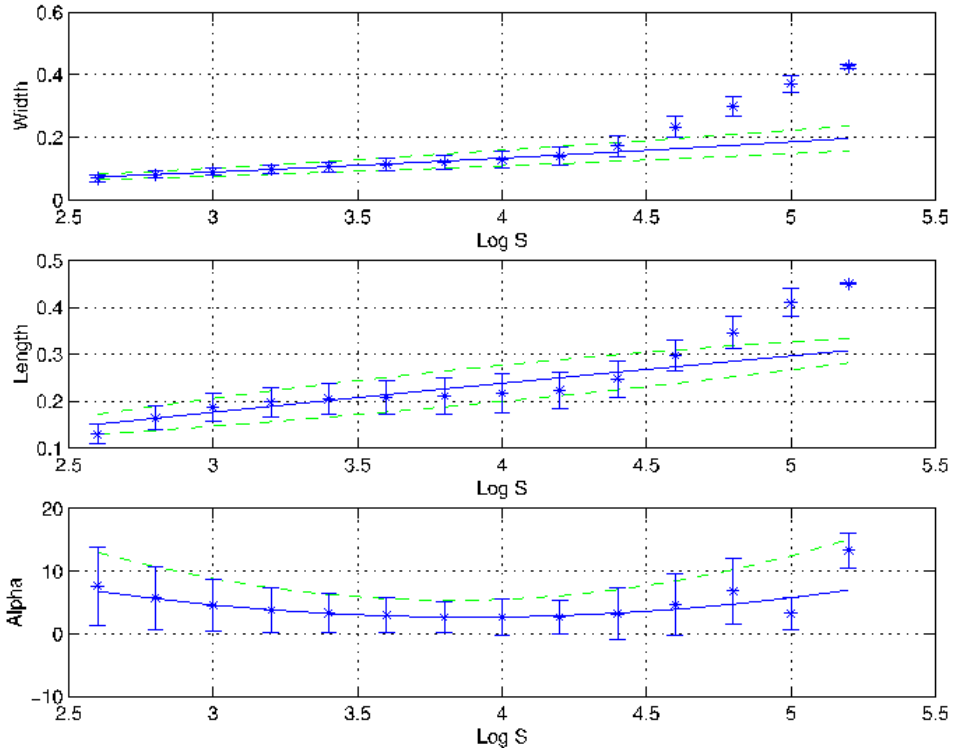

Figure 4.13: Simulated gamma-ray parameter distribution of *width*, *length* and *alpha* versus log(*size*). Blue crosses show the mean; *solid lines* show the polynomial fit; and *dashed lines* show the actual cut chosen for a tolerance of $2\,\sigma$.

Once the previous steps were all fullfilled, it was possible to reconstruct the energy spectrum of gamma-rays coming from the Crab Nebula, by applying the method outlined by Mohanty et al. (1998). The primary energies of the resulting gamma-ray events were estimated using equation 4.2.

Figure 4.16 shows the resulting reconstructed energy spectrum of the Crab Nebula during observations in the 2008-09 season. As the Crab Nebula did not show any curvature in the spectrum, a simple power-law was used to fit the data, getting:

$$\frac{dN}{dE} = (3.4 \pm 0.1)\ (E)^{-2.61\pm0.05} \times 10^{-11}\ \ \mathrm{TeV}^{-1}\ \mathrm{cm}^{-2}\ \mathrm{s}^{-1}. \tag{4.4}$$

The fit is also shown in Figure 4.16. The result agrees, within statistical uncertainty, with the spectrum from the VERITAS (see equation 1.2) and H.E.S.S Collaborations (Aharonian et al. 2006). Thus, the applied procedure was found to be suitable.

The uncertainty for the first point of the spectrum shown in Figure 4.16 is large because that point is below the energy threshold where the trigger calibration

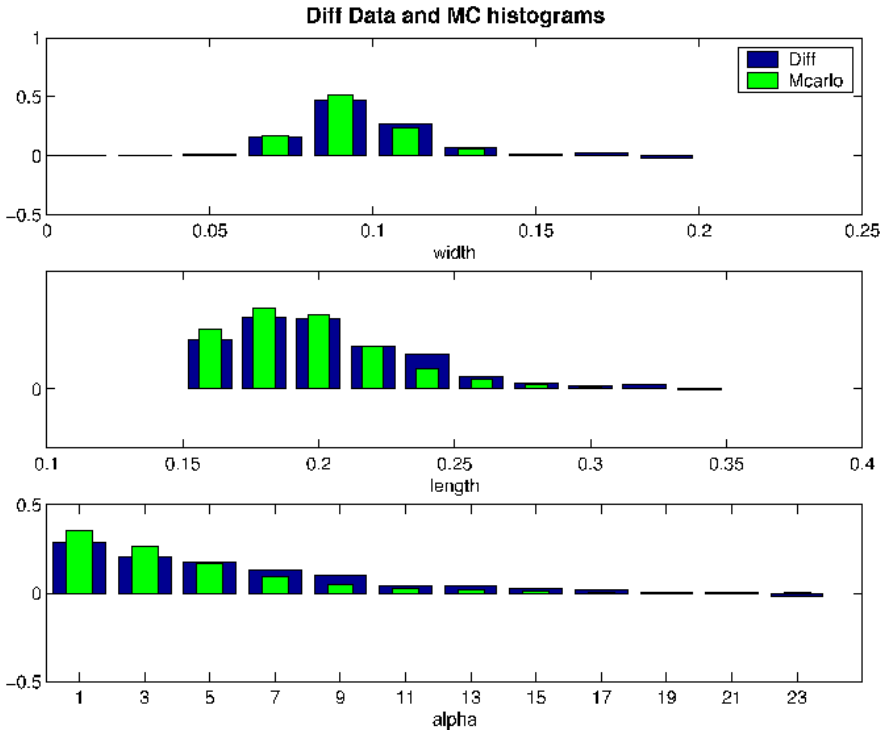

Figure 4.14: Histograms of the measured excess (ON-OFF differences, *blue*) compared to simulated events (*green*) for the cut parameter distribution of *width*, *length* and *alpha*.

cannot be reliable. The very-high-energy point might be correct, but the statistics are too low and the uncertainty is large, so it is better to take out that point in order to obtain a good fit.

Figure 4.17 shows the contours of the χ^2 fit for the Crab data in 2008-09. The dot at the center is the minimum value and χ^2 increases for each solid contour. The first inside-line contour represents the 68 % confidence level region; the second line the 90 % and the third line correspond to a 95 % confidence level region. It can be seen that the ellipses are approximately aligned with the axes, which might imply that the errors in the power index and normalization are approximately uncorrelated.

This method was applied to Markarian 501 in the 2008-09 observing season to get the energy spectrum for the VHE flare that was observed with the Whipple 10 m telescope. Those results are shown in Chapter 5.

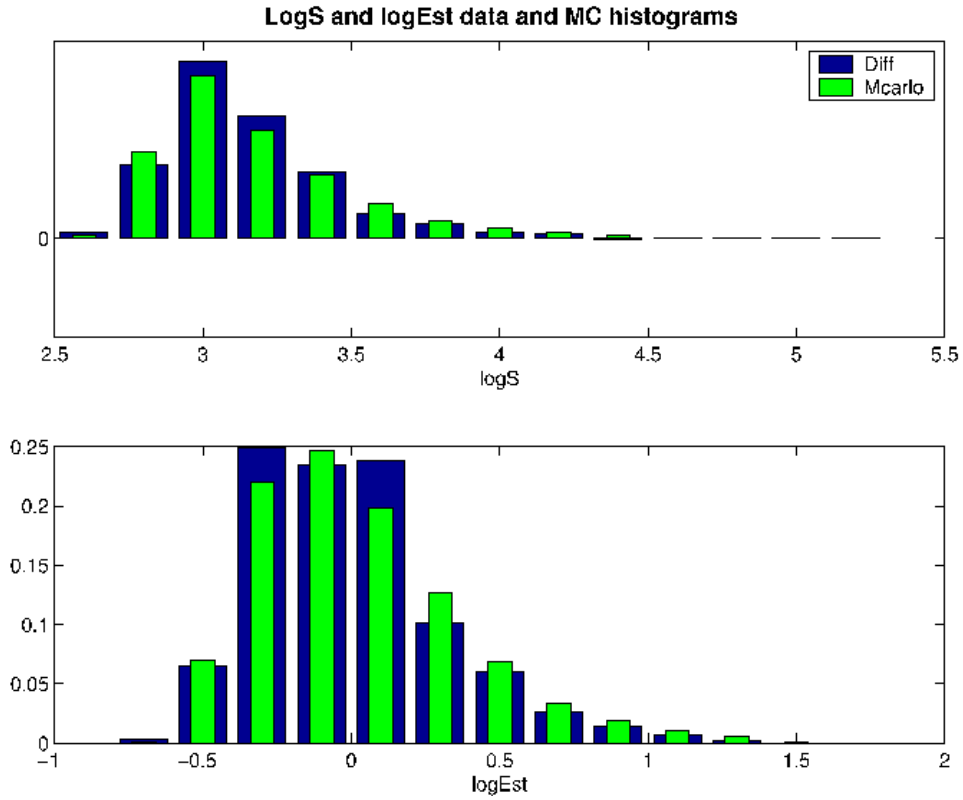

Figure 4.15: Histograms of the measured excess (ON-OFF differences, *blue*) compared to simulated events (*green*) for the log(*size*) and log(E_{est}) distributions.

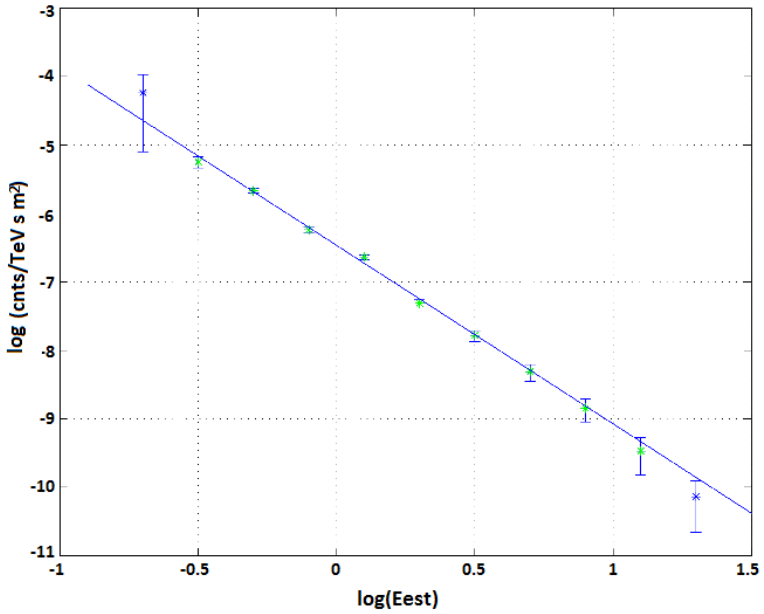

Figure 4.16: Energy spectrum of the Crab Nebula for the 2008-09 season observations taken with the Whipple 10 m telescope. The dotted line is the best fit.

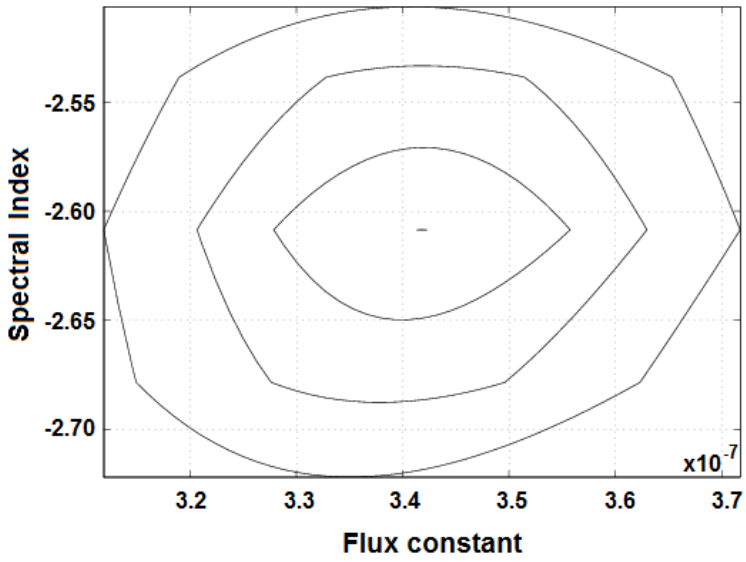

Figure 4.17: Contour plot of the 68 %, 90 % and 95 % confidence intervals from the χ^2 fit to a power law for all the data set.

Chapter 5

Multi-wavelength Campaigns of Mrk 421 and Mrk 501

During the 2007-2008 and 2008-2009 observing seasons with VERITAS and Whipple, several multi-wavelength campaigns were conducted. This chapter deals specifically with data from Markarian 421, taken in 2007-2008 (Acciari et al. 2011) and Markarian 501, taken in both 2007-2008 and 2008-2009 (Abdo et al. 2011a, Aliu et al. 2012, Kranich et al. 2009, Pichel et al. 2009).

Table 5.1 summarizes all the instruments involved in the mwl campaigns of Mrk 421 and Mrk 501. For both sources, the X-ray coverage was very well sampled, having some simultaneous observations between X-rays and γ-rays. The coverage from other instruments were quite varied; some of them had a good coverage during all the campaign while others had a few observations only. Nevertheless, those campaigns covered all the electromagnetic spectrum from radio to VHE γ-rays. Although the Whipple telescope was dedicated to blazar monitoring during those seasons, the γ-ray data have large gaps due to periods of daylight, bright moonlight or bad weather.

The analysis is focused on the study of possible correlations in flux and energy between different wavelengths of the electromagnetic spectrum, mainly concentrated in the X-ray/γ-ray bands. Variability studies of these multi-wavelength data, applying different methods to investigate the level of variation at different time scales for all wavelengths with good coverage, are presented.

Waveband	Instrument	Range
Radio	Metsahovi	37 GHz
	UMRAO	4.8-14.5 GHz
	OVRO	15 GHz
Optical	MitSume	r, Rc, Ic bands
	UVOT	193-260 nm
	WIYN	B,V,R band
	GASP	R band
X-ray	Swift	0.3-10 keV
	RXTE	2-10 keV
HE γ-ray	Fermi	0.1-100 GeV
VHE γ-ray	VERITAS	0.2-5 TeV
	Whipple	0.4-5 TeV

Table 5.1: Instruments involved in the multi-wavelength campaigns of Markarian 421 and Markarian 501 during 2007-2009.

5.1 Multi-wavelength Lightcurves

5.1.1 Markarian 421 in 2007-08

The lightcurves of Markarian 421 obtained during the multi-wavelength campaign in 2007-2008 are shown in Figure 5.1. Only the observations from December 2007 to June 2008 are included since for TeV instruments the source was only visible during that period. From top to bottom, the panels show optical data (R, V and B bands and 193-260 nm) obtained with several telescopes, radio data (37, 14.5, 8 and 4.8 GHz) acquired with several instruments, hard X-ray data from RXTE-BAT, soft X-ray data from *Swift*-XRT, *Swift*-ASM and RXTE-PCA, and VHE γ-ray data from the Whipple 10 m telescope and VERITAS (see Table 5.2 for further information). Most of the data points were taken run by run in order to obtain better statistics for investigating the characteristic timescales. To provide a comparison between the results obtained by Whipple and VERITAS (see Figure 5.1), the VHE light curve is shown with a common energy threshold of 300 GeV. Whipple data (which had an energy threshold of 400 GeV) were normalized considering a power law spectrum with index -2.5.

A constant function for each instrument was fitted to the fluxes for the whole period. The χ^2 per degree of freedom of these fits was taken as a simple measure of the variability over that time. The results for each fit are shown in Table 5.2. A large χ^2 indicates a poor model fit, likewise, a small, close to zero value of χ^2,

Waveband	Instrument	No of Data Points	MJD range	χ^2
Radio	UMRAO 4.8 GHz	9	54411-54608	0.06
	UMRAO 8 GHz	11	54417-54619	0.6
	UMRAO 14.5 GHz	21	54406-54611	0.08
	Metsahovi 37 GHz	23	54421-54589	0.66
Optical-UV	*Swift*-UVOT 260 nm	30	54505-54594	0.0001
	Swift-UVOT 220 nm	33	54502-54594	0.0001
	Swift-UVOT 193 nm	35	54502-54594	0.0001
	WIYN R	47	54482-54608	0.0007
	WIYN V	43	54482-54620	0.0005
	WIYN B	43	54482-54612	0.0003
X-ray	*Swift*-XRT	63	54417-54594	4.39
	RXTE-ASM	279	54400-54699	17.66
	RXTE-PCA	85	54472-54593	12.21
	Swift-BAT 15-150 keV	231	54400-54640	7.39
VHE γ-ray	VERITAS	148	54417-54623	3.86
	Whipple	286	54417-54622	2.88

Table 5.2: Dataset of Markarian 421 for the multi-wavelength campaign in 2007-2008.

means that the model fit is correct.

X-rays fluxes showed a long-term structure with phases of high activity followed by phases of lower activity (see Figure 5.1) with strong flux variability on nightly time scales. A flux variation of a factor two can be observed on a timescale of a few days. In the optical band, flux variations were also observed on timescale of weeks or even months, while no significant variations were found at radio energies. In the VHE γ-ray observations, a variability going from a few days to weeks was clearly observed. The source was almost all the time in medium and high states of activity, getting the maximum activity in May. Figure 5.2 shows the data of Figure 5.1 restricted to the period March-May, 2008, in which exceptionally bright X-ray flaring and strong VHE gamma-ray flare were found.

On May 2, 2008 (MJD 54588), the Whipple 10 m gamma-ray telescope observed a short flare of TeV γ-rays with some unusual luminosity from Markarian 421. The source was routinely monitored as part of the Whipple TeV gamma-ray monitoring program which serves as an early alert program for VERITAS. After a brief interruption in observations, the source was observed at an intensity of 15 Crab, brighter than any other previously observed at the Whipple Observatory.

The flux decreased to less than a half in five minutes. Shortly afterward, the source was observed by VERITAS, recording a level of 10 Crab. Figure 5.3 shows the short flare observed by Whipple and VERITAS with a time bin of 2 minutes.

On May 3, 2008 (MJD 54589), Markarian 421 remained in a high activity state. Figure 5.4 shows Whipple and VERITAS observations (2-minute time bin) for that night, reaching a flux level of 8 Crab. The following three days, after the VHE flare, the intensity decreased and the source went back to a low state.

Observations with Whipple and VERITAS on May 2 and 3, 2008 were taken under very different zenith angles ($10° - 60°$). A study searching for the gamma-ray excess rate of the Crab at different zenith angles for similar epochs was made. Thus, the results for Mrk 421 were normalized to the Crab rate for the same zenith angle. This simplistic scaling is strictly valid only for a TeV spectrum similar to the Crab Nebula spectrum with an spectral index of 2.5. However, the systematic error introduced by this scaling was small compared to the statistical error of the flux data.

It can be seen in Figure 5.2, that the strongest TeV emission is not coincident with the strongest soft/hard X-ray activity. The lack of increased X-ray emission during the peak of TeV flaring might indicate an "orphan" flare (e.g. Krawczynski et al. 2004). However, the characteristic time scales of flux changes in the TeV band can be shorter than an hour (the major flare is fully contained within a time interval of 5 hours), so the comparison has to be restricted to simultaneous or very contemporaneous data. The VHE flare is followed by an enhanced X-ray flux: the *Swift*-BAT, *Swift*-XRT and RXTE-PCA data indicate a doubling in flux level between the night of the flare and the following night, declining back to the previous level within a few days. The corresponding structure of the X-ray light curve does not substantially differ from low-state variations, so, a physical connection to the TeV activity cannot be claimed.

A simple approach to get a characterization for the VHE flare has been performed. A very simple flare model (Albert et al. 2007), in which the flare's amplitude, duration and rise/fall times can be quantified, was employed. The proposed model parameterizes a flux variation (flare) $F(t)$ superposed on a stable emission as:

$$F(t) = a + \frac{b}{2^{\frac{t-t_0}{c}} + 2^{-\frac{t-t_0}{d}}} \tag{5.1}$$

where a is the baseline emission before the flare; t_0 is the time when the highest flux in the light curve was observed; and b, c, and d are fitting parameters. The c and d parameters denote the flux-doubling rise and fall times, respectively. The resulting fit using equation 5.1 is shown in Figure 5.5. The value found for the rise time was (38.22 ± 1.15) minutes and for the fall time was (46.73 ± 2.05) minutes.

TeV flux variations were measured for different TeV blazars with characteristic time scales from $\sim$5 min (Albert et al. 2007, Gaidos et al. 1996) to one hour (Aharonian et al. 2009). The corresponding size of the emission region was calculated, obtaining the same order of the Schwarzschild radius of the black hole of

the corresponding AGN (Aharonian et al. 2009, Albert et al. 2007). This could indicate that the base of the jet is responsible for the VHE gamma-ray emission.

5.1.2 Markarian 501 in 2008

The well-known VHE blazar Mrk 501 was observed from radio to VHE gamma-ray from March to May 2008 as part of an extensive multi-wavelength campaign. The source remained in a low state of activity for all the period with a VHE flux of around 10-20 % of the Crab Nebula flux.

In the VHE domain, the Whipple telescope was dedicated to monitoring this blazar (among other 4 blazars) every possible night for a total of 45.7 hours with a total significance of $6\,\sigma$. VERITAS was also observing this source, as part of the campaign, for a total of 6.2 hours with a $30\,\sigma$ detection. In Figure 5.6 the light curves from radio to VHE gamma-ray are shown. For the Radio band, Metsähovi and UMRAO at 4.8, 8 and 14 GHz were monitoring the source. In the optical band, results from GASP with a very good coverage are presented, whereas for the X-ray band RXTE-PCA observations are shown. Details about the time period covered for each instrument can be found in Table 5.3. A constant fit was made for each instrument in order to look for variability; the resulting values are also shown in Table 5.3.

Waveband	Instrument	No. Data Points	MJD Range	χ^2
Radio	Metsähovi 37 GHz	84	54571-54612	2.67
	UMRAO 4.8 GHz	7	54532-54624	0.39
	UMRAO 8 GHz	5	54524-54620	0.01
	UMRAO 14 GHz	6	54536-54610	0.01
Optical	GASP R	269	54550-54630	0.05
X-ray	RXTE-PCA	28	54554-54601	30.6
VHE γ-ray	VERITAS	16	54557-54627	6.77
	Whipple	30	54555-54559	1.31

Table 5.3: Dataset of Markarian 501 for the multi-wavelength campaign in March-May 2008.

Whipple data were normalized to VERITAS data in order to get the same energy threshold for both instruments and make them comparable. From the light curves, it could be said that the behavior for both observations are not comparable, as Whipple data showed a higher baseline emission, with more signs of variability. In the optical band, Mrk 501 was observed by GASP, having a very extense coverage and a very good sampling over the whole period. Some evidence of variability was appreciated from the light curve but it was rather small. In the radio band, UMRAO (at three different energies) and Metsähovi were monitoring

the source with no sign of short nor large variability during the campaign. In the X-ray band a statistically significant variability was observed although the flux variations were relatively small.

5.1.3 Markarian 501 in 2009

As part of a large-scale multi-wavelength campaign (Abdo et al. 2011a), Mrk 501 was observed from April 17 to May 5, 2009. The monitoring included a number of ground- and space-based observatories covering the spectrum from radio to very high energy γ-rays.

Figure 5.7 shows the light curves of Mrk 501 for the instruments involved in the 3-week time interval. At VHE it was observed with the Whipple 10 m telescope (Kildea et al. 2007), every night for a total of 20 hours, and with VERITAS (Holder et al. 2006, Weekes et al. 2002) for a total of 4 hours (Huang et al. 2009). VERITAS observations during the nights of April 30 and May 1 were done with two telescopes, those on the remaining nights were done with three telescopes, because the other units were not operational due to hardware issues. To provide a comparison between the results that were obtained by Whipple and VERITAS, the VHE light curve is shown with a common energy threshold of 300 GeV. Whipple data (which has an energy threshold of 400 GeV) were normalized considering a power law spectrum with index -2.5 as done with Mrk 421. At the HE band, *Fermi*-LAT (Atwood et al. 2009) was constantly monitoring the source while the X-ray band was covered by *Swift*-XRT and RXTE-PCA. At optical frequencies the source was covered by various instruments, such as GASP, Mitsume and *Swift*-UVOT. Metsähovi and OVRO were used to monitor radio frequencies. Details are given in Table 5.4.

At radio and optical bands, the measured fluxes were constant (within statistical uncertainties). At the X-ray bands, it can be seen a statistically significant variability (due to the high sensitivity of *Swift*-XRT and RXTE-PCA), but the flux variations were relatively small (quite below 50 %). On the other hand, at the VHE domain, VERITAS, and especially Whipple, measured (statistically significant) flux variations of a factor of a few and up to a factor of 10 for MJD 54952. Therefore, during the mentioned 3-week time interval, the highest variability was found to be at the highest energies.

At VHE, the light curve was consistent with the constant emission of the source (3.9×10^{-11} ph cm^{-2} s^{-1}) until the night of May 1 (MJD 54952), when a high-emission state was detected with both Whipple and VERITAS, reaching a maximum γ-ray flux 10 times the average baseline flux, approximately 5 times the Crab Nebula flux.

Figure 5.8, in which each point corresponds to a 4-minute bin, shows the Whipple 10 m and VERITAS light curves for May 1, 2009. The flux increased by a factor of $\sim$4 in the first 30 minutes. The days after the flare (MJD 54953-55), the source continued in a high state; the flux being about twice the baseline flux each night.

Swift-XRT observations were not strictly simultaneous to the VHE observations performed by Whipple and VERITAS. The time difference between *Swift*

Waveband	Instrument	No. Data Points	MJD Range	χ^2
Radio	Metsähovi 37 GHz	12	54942-54956	15.75
	OVRO 15 GHz	5	54940-54955	4.43
Optical	GASP R	10	54938-54955	0.72
	MitSume r, Rc, Ic	5	54948-54956	3.08
	Swift-UVOT	10	54941-54955	$\sim$50
X-ray	*Swift*-XRT low	9	54941-54955	128.31
	Swift-XRT high	9	54941-54955	70.22
	RXTE-PCA	4	54941-54956	11.90
HE γ-ray	*Fermi*-LAT	6	54938-54956	2.36
VHE γ-ray	VERITAS	6	54938-54956	0.06
	Whipple	17	54938-54956	0.03

Table 5.4: Dataset of Markarian 501 for the 3-week period in 2009 mwl campaign.

observations and Whipple and VERITAS observations was 7 hours. VERITAS observations started 1.5 hours later than the Whipple observations and continued with simultaneous observations until the end of the night. These two instruments observed a flux enhancement by more than a factor of 5. Therefore, it was reasonable to assume that the VHE flare lasted more than 3 hours, and hence, that *Swift* observations might have occurred during this outstanding VHE state. However, Swift did not record any substantial flux increasing during MJD 54952. The flux in the energy range 0.3-2 keV was essentially compatible with the flux during previous days. In the range 2-10 keV, a flux increasing was observed on MJD 54952, lasting several days. However, the magnitude of this variation was about 50 %, being substantially smaller than the flux increase observed by Whipple and VERITAS at the VHE domain.

Fermi-LAT operates in a survey mode, which means that any point of the sky is observed during 30 min approximately every 3 hours. Hence, sources are observed continuously on timescales down to 3 hours. However, as Mrk 501 is a relatively weak source for *Fermi*-LAT an integration over several days is typically required, in order to have a significant detection. The light curve with the data binned in 5-day time intervals is presented in Figure 5.7. The last time interval did not show any significant variation with respect to the previous time intervals, despite it contains the entire VHE flare, started on MJD 54952. However, it is worth mentioning that on MJD 54952 (the day with the highest VHE flux), *Fermi*-LAT detected Mrk 501 with a significance larger than 5σ, significantly differing to the other days. The measured flux (above 300 MeV) for that day was $(3.46 \pm 2.37)\ 10^{-8}$ ph cm^{-2} s^{-1}.

The simple flare model (equation 5.1) was also used to fit the VHE flare ob-

served by Whipple. The results are shown in Figure 5.9, in which the rise time was (27.10±1.12) minutes and the decay time was (51.05±2.24) minutes. The fall time was twice larger than the rise time, implying that the emission region is extremely small. This fast variability was not similar to the one observed in previous works (Aharonian et al. 2007b), in which the rise and decay time went from 2 to 3 minutes.

Optical observations were performed as part of the Steward Observatory blazar monitoring program with the 2.3 m Bok and the 1.54 m Kuiper telescopes every night from MJD 54947 to MJD 54955, which included the night of the VHE flare. Figure 5.10 shows the light curve, the degree of the optical linear polarization and the electric-vector position angle (EVPA) from those nights. From MJD 54947-51, the degree of polarization was steady and dropped a 15 % after the VHE flare. The EVPA light curve showed a continuous increase from 15 to 30 degrees in 3 days, and the rotation stopped right when the large VHE flare occured. If both events can be physically linked, as it seems to be the case, that might indicate a common origin for the optical and γ-ray emission as it has already been seen in Abdo et al. (2010), Jorstad et al. (2010), Marscher et al. (2010).

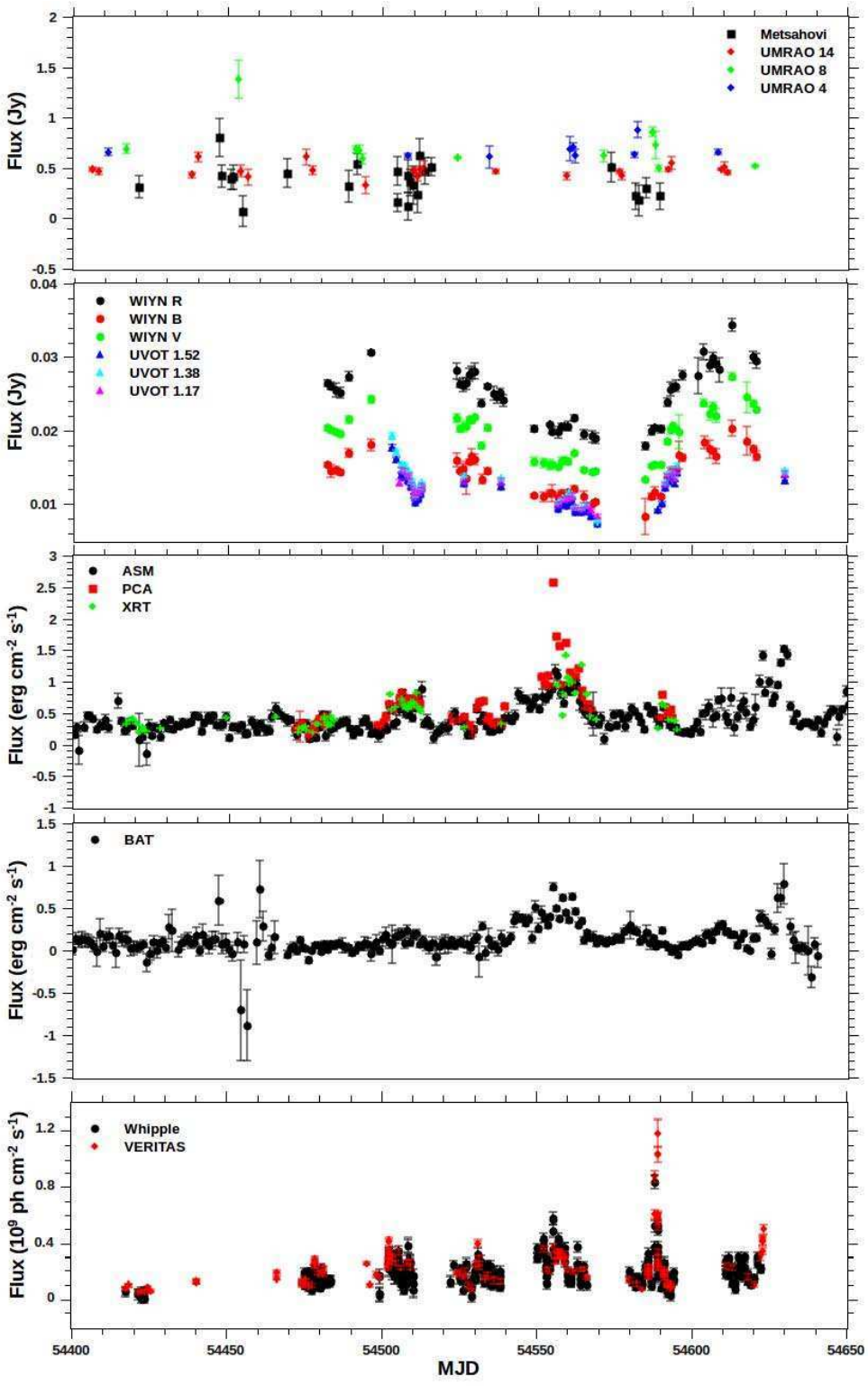

Figure 5.1: Light curves for Mrk 421 during the 2007-2008 observing season. *Top*: Radio observations with Metsähovi (filled squares) and UMRAO 14.8 GHz (red diamonds), 8 GHz (green diamonds) and 4 GHz (blue diamonds). *Second*: Optical observations with WIYN in the R (black circles), B (red circles) and V (green circles) bands; *Swift*-UVOT in the Ultraviolet with three different bands, UVW1 (260 nm, blue triangles), UVM2 (220 nm, light blue triangles) and UVW2 (193 nm, purple triangles). *Third*: Soft X-ray observations, 2-10 keV, with *Swift*-XRT (green diamonds), *Swift*-ASM (black circles) and RXTE-PCA (red squares). *Fourth*: Hard X-ray observations, 15-50 keV with RXTE-BAT. *Bottom*: VHE γ-rays: Whipple ($E > 400$ GeV, normalized to $E > 300$ GeV according to a power law with photon index -2.5; black filled circles) and VERITAS ($E > 300$ GeV; red filled diamonds).

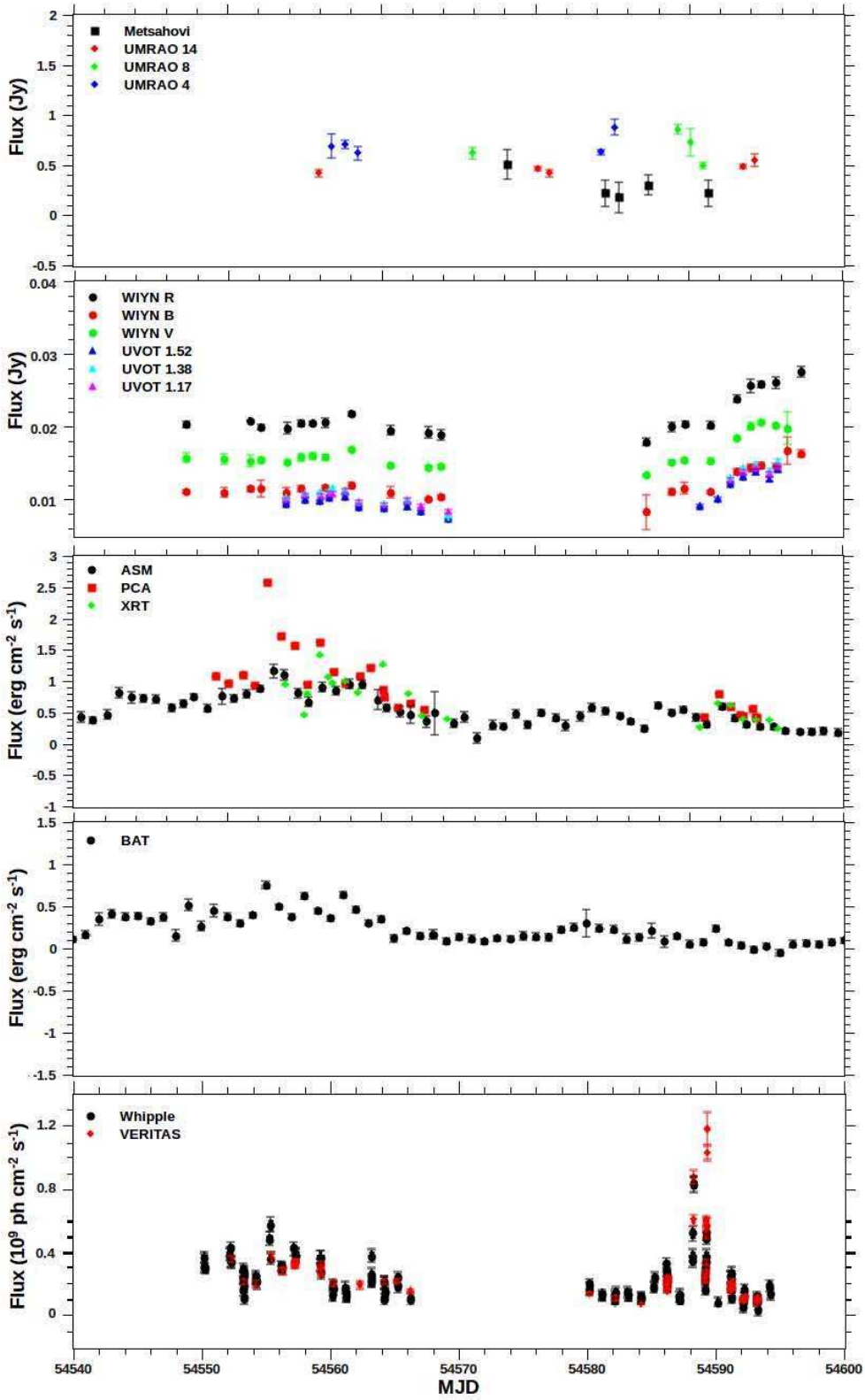

Figure 5.2: Light curves from Mrk 421 during March to May, 2008, with all the instruments involved at the campaign. For details see caption in Figure 5.1.

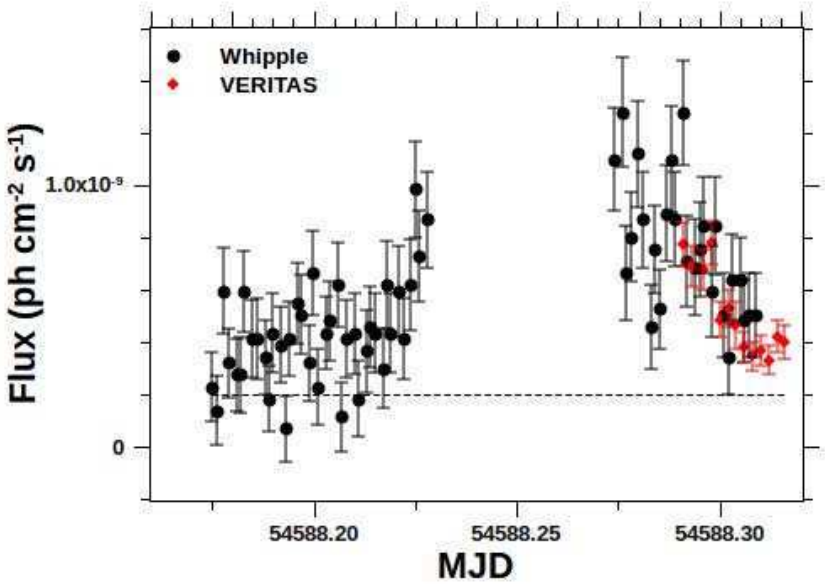

Figure 5.3: Light curve of Mrk 421 VHE flare during May 02 2008 with VERITAS and the Whipple 10 m Telescope (2-minute binned).

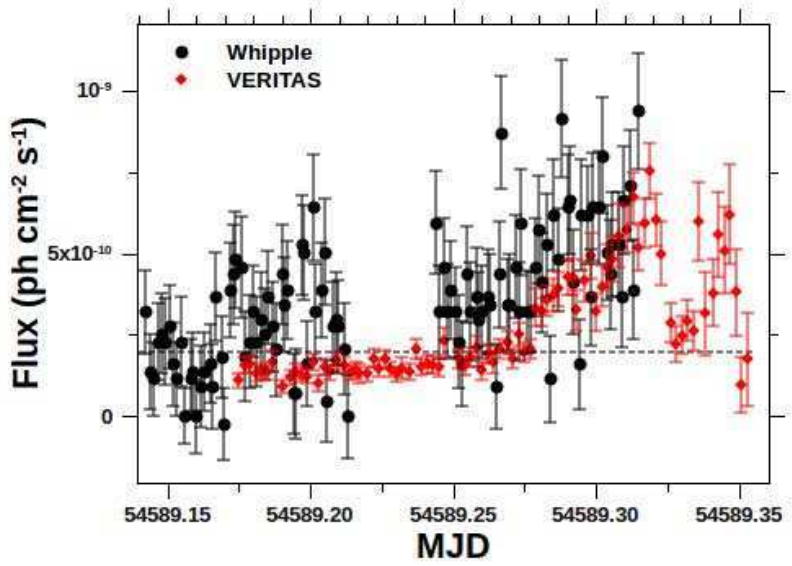

Figure 5.4: Light curve of Mrk 421 VHE flare during May 03 2008 with VERITAS and the 10m Whipple Telescope (2-minute binned).

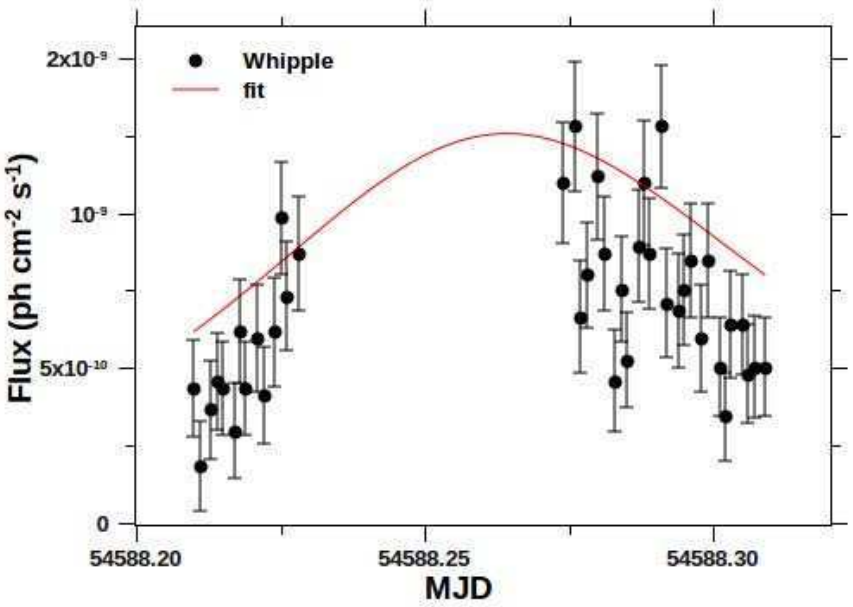

Figure 5.5: Light curve of Mrk 421 VHE flare during May 02, 2008 with the Whipple 10 m telescope (2-minute binned) in which the flare was fitted with a simple model.

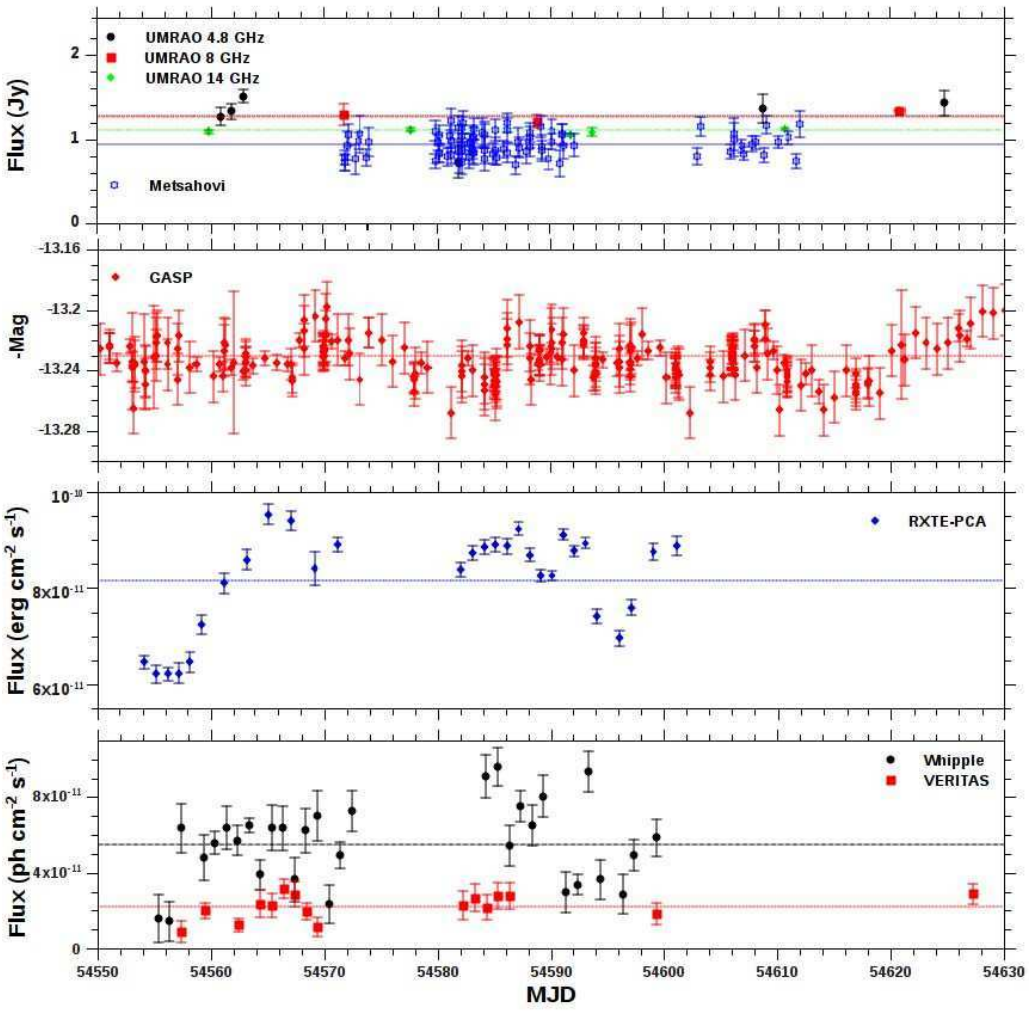

Figure 5.6: Light curve of Mrk 501 from radio to VHE gamma-rays as part of the multi-wavelength campaign from March-May 2008. Each dotted line is a constant fit made to each instrument to see if there is some indication of variability. *Top*: Radio observations with Metsähovi (open stars) and UMRAO 14.8 GHz (green diamonds), 8 GHz (red squares) and 4 GHz (black circles). *Second*: Optical observations with GASP in the R band. *Third*: X-ray observations in the 2-10 keV band with RXTE-PCA. *Bottom*: VHE γ-rays: Whipple ($E > 400$ GeV, normalized to $E > 300$ GeV according to a power law with photon index -2.5; black filled circles) and VERITAS ($E > 300$ GeV; red filled squares).

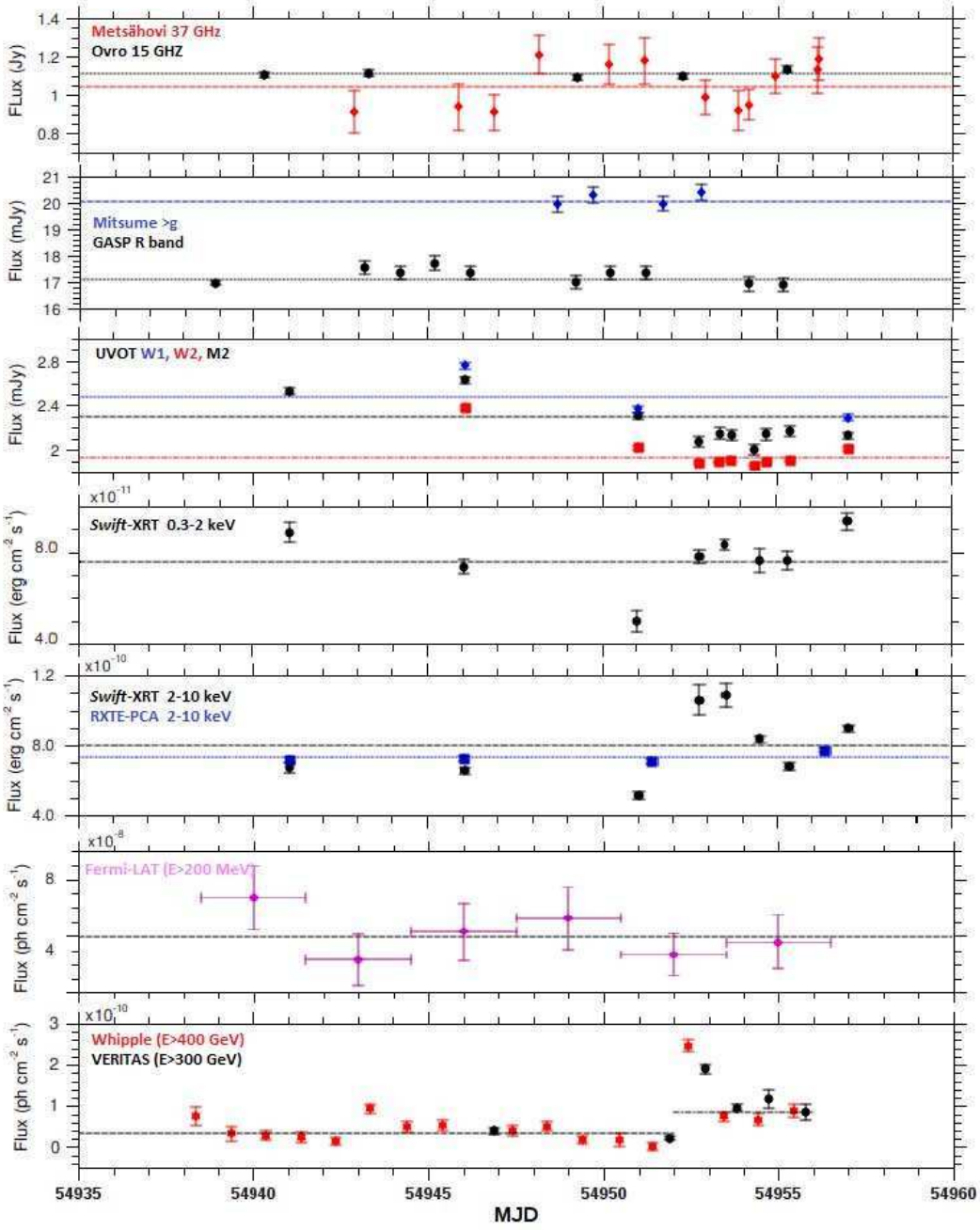

Figure 5.7: Light curves in a daily average for Mrk 501 from April 17 to May 5, 2009. Each dotted horizontal line represents a constant line fit for each instrument involved. *Top*: OVRO at 15 GHz (black filled circles) and Metsähovi at 37 GHz (red filled diamonds); *Second*: Mitsume in g band (blue filled diamonds) and GASP in R band (black filled circles). *Third*: *Swift*-UVOT in the Ultraviolet, with three different bands, UVW1 (260 nm, blue diamonds), UVM2 (220 nm, black circles) and UVW2 (193 nm, red squares). *Fourth*: X-ray: *Swift*-XRT 0.3-2 keV. *Fifth*: X-ray: RXTE-PCA (blue squares) and *Swift*-XRT (black circles) 2-10 keV (nightly average); *Sixth*: HE gamma-ray: *Fermi*-LAT (E > 300 MeV; 5-day average); *Bottom*: VHE γ-rays: Whipple (E > 400 GeV, normalized to E >300 GeV according to a power law with photon index -2.5; red filled stars) and VERITAS (E > 300 GeV; filled circles).

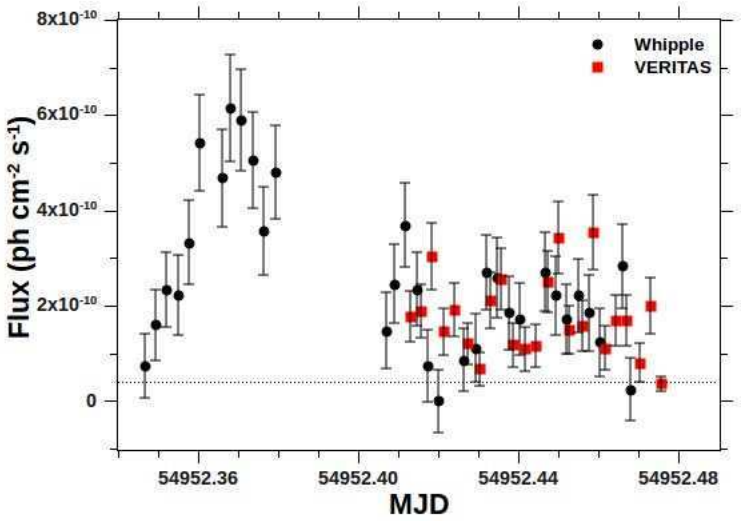

Figure 5.8: Whipple 10 m and VERITAS light curve (4-minute binning) for the night of the VHE flare. Dotted line shows the baseline emission for the source depicted in Figure 5.7.

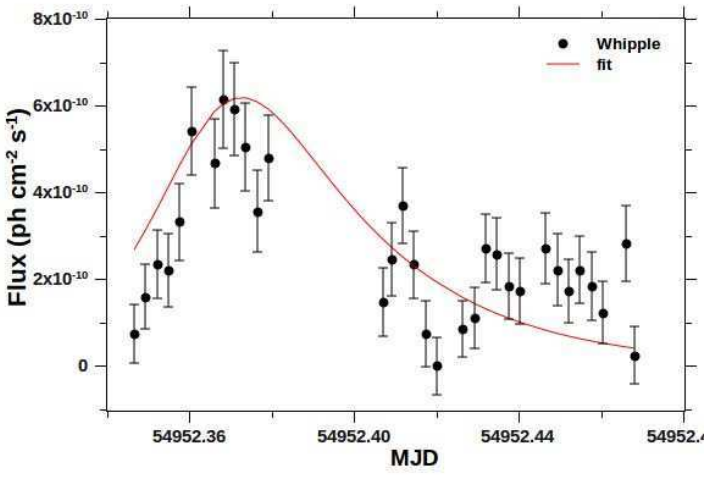

Figure 5.9: Whipple 10 m light curve (4-minute binning) for the night of the VHE flare with the fitted model.

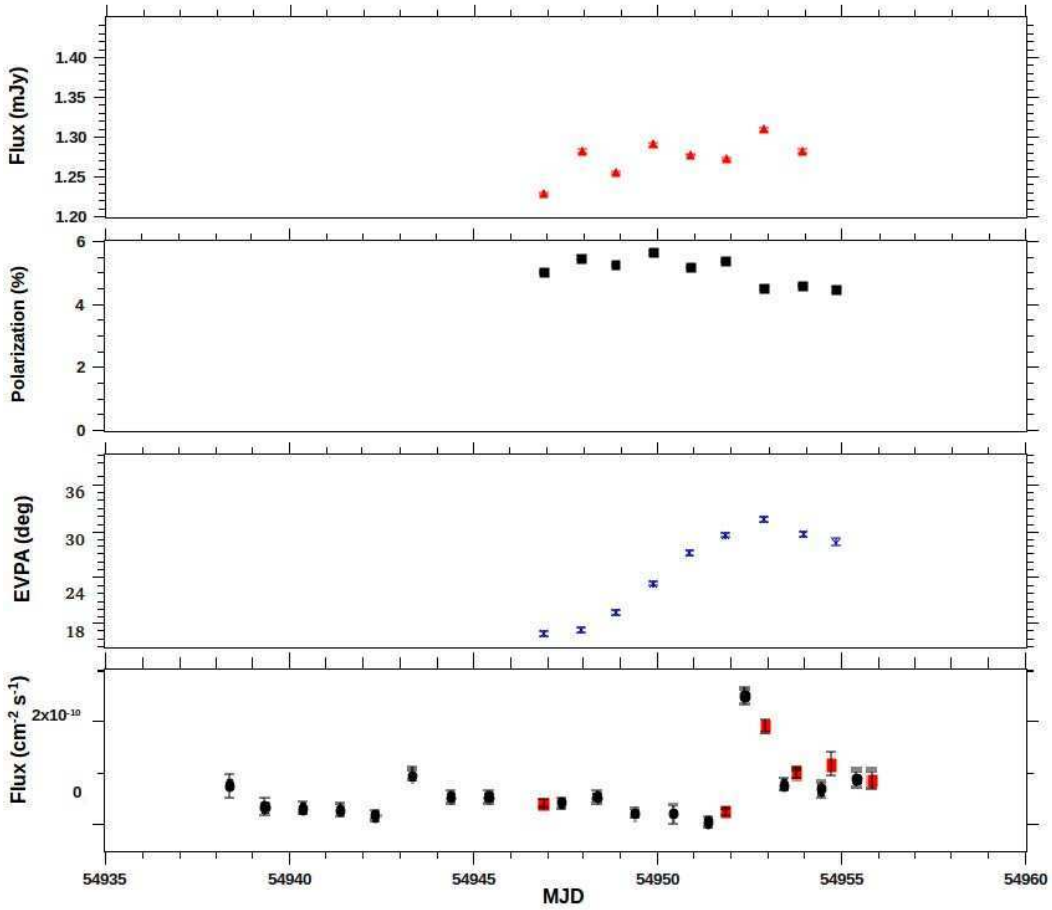

Figure 5.10: Optical flux, degree of the optical linear polarization and EVPA light curves (first, second and third plots respectively) measured with the Steward Observatory, and (fourth plot) the VHE light curve obtained with Whipple and VERITAS.

5.2 Variability & Correlation

Blazars are known to present rapid and irregular variability, exhibited over all the electromagnetic spectrum during different time scales, from minutes to months. The different variability time scales found in the same energy band are related to the emission zone size. The rapid emission could be related to a very compact zone, close to the black hole, while the slow emission could be related to slower changes in the structure and other effects, such as cooling effects (e.g. Kembhavi & Narlikar 1999).

The first approach to search for variability was done by fitting points in the light curve with a constant flux value. The value of χ^2 per degree of freedom of this fit was taken as a simple measure of the variability over time (see Tables 5.2, 5.3 and 5.4). The χ^2 method is an accepted standard test to solve the problem for binned data and to make a first approximation of the degree of variability.

In order to go further in quantifying the flux variability present in the light curves, the fractional RMS variability amplitude, $F_{\rm var}$, (Zhang et al. 2005), was calculated as:

$$F_{\rm var} = \sqrt{\frac{S^2 - \overline{\sigma}^2}{\overline{F}^2}} \tag{5.2}$$

where $\overline{F}$ is the average photon flux, S the standard deviation of the total number N of flux measurements and $\overline{\sigma}^2$ is the mean squared error. The uncertainty $\Delta F_{\rm var}$ is given by:

$$\Delta F_{\rm var} = \sqrt{\left\{\sqrt{\frac{1}{2N}} \cdot \frac{\overline{\sigma}^2}{\overline{F}^2\ F_{\rm var}}\right\}^2 + \left\{\sqrt{\frac{\overline{\sigma}^2}{N}} \cdot \frac{1}{\overline{F}}\right\}^2}. \tag{5.3}$$

$F_{\rm var}$ is a commonly used measure of the intrinsic amplitude of the variability of a time series in order to study the variability during a campaign (e.g. Edelson et al. 2002, Horan et al. 2009). An $F_{\rm var}$ value close to zero indicates that there was no significant variability over the period, and a value close to one, indicates a strong variability. The variability correlation between different wavelengths can indicate the processes involved in the emission or put some constrains on the mechanisms. A clear correlation between X-rays and VHE gamma-rays was found in several studies for blazars (e.g. Fossati et al. 2008). However, some other studies showed no clear correlation between both bands (Krawczynski et al. 2004). X-ray and VHE γ-ray fluxes were historically correlated, even the large VHE γ-ray flare not being accompanied by a large X-ray flare. So far, it has been difficult to affirm (even if the correlation between both bands is the most accepted theory) whether it is the same population of electrons the responsible for the synchrotron emission

at the X-ray band and the Inverse Compton at the VHE band.

The relationship between the VHE γ-ray flux and the X-ray flux was examined in this work by using flux-flux plots, whose trends indicate a correlation in the emission between both bands. The discrete correlation function (DCF) was calculated between different bands (Edelson & Krolik 1988). This method is an approximation of the standard correlation function that works with functions not over-well sampled, as it happens in the light curves for the observations used in this work.

For each pair of points $[a(ti), b(tj)]$, taken from two datasets a and b, the time difference $\Delta t_{ij} = t_i - t_j$ was calculated, and the unbinned discrete correlation function (UDCF) was obtained by:

$$UDCF_{ij} = \frac{[a(t_i) - \langle a \rangle][b(t_i) - \langle b \rangle]}{\sqrt{[\sigma_a^2 - e_a^2][\sigma_b^2 - e_b^2]}} \tag{5.4}$$

where $\langle a \rangle$ and $\langle b \rangle$ are the mean values, σ_a and σ_b the standard deviations and e_a and e_b the mean measured errors. For any given time delay between the two datasets $T_{\rm lag}$, $UDCF_{ij}$ values are sorted into bins of width τ, containing the N pairs (t_i, t_j) for which $T_{\rm lag} - \tau/2 < \Delta t_{ij} < T_{\rm lag} + \tau/2$. The most directly and useful quantity $DCF(T_{\rm lag})$ is then obtained by averaging over the N pairs:

$$DCF(T_{\rm lag}) = \frac{1}{N} \sum UCDF_{ij} \tag{5.5}$$

The estimation of the uncertainty of DCF is given by:

$$\sigma_{DCF(T_{\rm lag})} = \frac{1}{N-1} \sqrt{\sum [UCDF_{ij} - DCF(T_{\rm lag})]^2} \tag{5.6}$$

5.2.1 Markarian 421 in 2007-08

The light curves presented in Figure 5.1 were examined in order to study and characterize their variability properties. $F_{\rm var}$ was calculated for all the involved experiments with significant amount of data by using a daily average for each energy band and the results are shown in Figure 5.11. The value of $F_{\rm var}$ was compatible with signs of variability for all energy bands. The hard X-ray domain, where RXTE-BAT observed a $F_{\rm var}$ of 0.98 ± 0.05, presents the highest values. This large variability was highly appreciated in the light curve shown in Figure 5.1, where phases of low/high activity were clearly seen. Besides, the VHE range shows a considerable variability: for VERITAS $F_{\rm var} = 0.47 \pm 0.05$ and for Whipple $F_{\rm var} = 0.69 \pm 0.07$. This large variability in the VHE domain is clearly dominated by the high VHE flare observed on MJD 54588 and the following days.

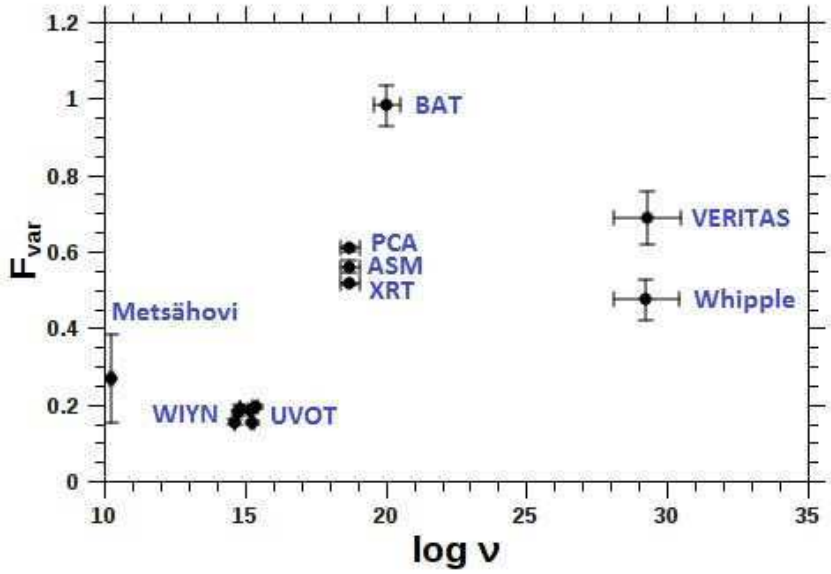

Figure 5.11: Fractional variability amplitude for all the instruments involved in the mwl campaign of Mrk421 in 2007-08.

Figures 5.12 and 5.13 show the VHE flux with VERITAS and Whipple vs. RXTE-BAT (15-150 keV) flux for different coincident times bins. The three plots together are useful to see how the average flux vs. flux relation varies as the window of coincidence is changed. If it had been some "orphan" flare present at X-ray or VHE bands during the observation time, it could be detected as an isolated point in a flux-flux diagram. Note that the "orphan" VHE flare of Mrk 421 becomes apparent when the coincidence window was opened to 24 hours.

A significant correlation between the hard X-ray and VHE fluxes was evidenced for the three different time windows. A linear fit was made obtaining for a 4 hrs a χ^2/NDF of 48/4 with a slope of 0.015±0.013; for 12 hrs a χ^2/NDF of 411/17 with a slope of 0.100±0.008 and for 24 hrs a χ^2/NDF of 409/21 with a slope of 0.109±0.006. No significant flux correlations were found between the VHE band and the remaining bands. This indicates that the emission in those bands and the X-ray and VHE γ-ray emissions are not originated in the same region.

Figure 5.14 shows the Discrete Correlation Function between the VHE with VERITAS and BAT light curves, positive values indicates that the RXTE-BAT light curve is lagging the VHE light curve.

The 2-10 keV light curve, combining data from *Swift*-XRT, RXTE-PCA and RXTE-ASM, was plotted in a flux-flux plot against the VHE γ-ray with VERITAS, for measurements that were coincident within 15 minutes and within 1 day, as shown in Figure 5.15. It can be seen that both bands are correlated and a linear fit was made for each time window, obtaining for 15 min a χ^2/NDF of 1083/47 with a slope of 0.116±0.004 and for 24 hrs a χ^2/NDF of 3335/108 with a slope of 0.083±0.003. It can be noticed in the figure an outlying point with high VHE flux and low 2-10 keV flux that is consistent with the "orphan" TeV flare seen in

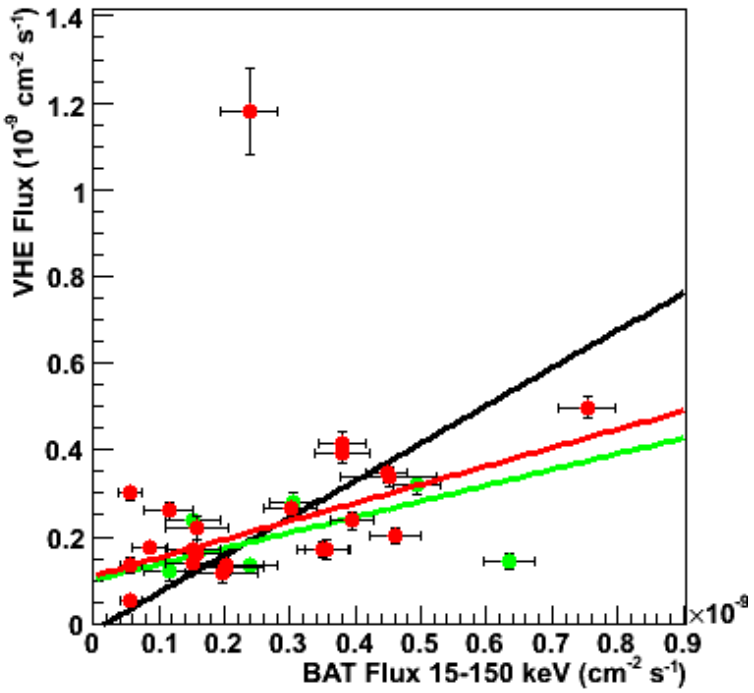

Figure 5.12: Flux-flux plot for VHE γ-ray with VERITAS and hard X-ray with BAT for Mrk 421. Black points correspond to 4hrs, green points to 12 hrs and red points to 24 hrs coincident time bins, respectively.

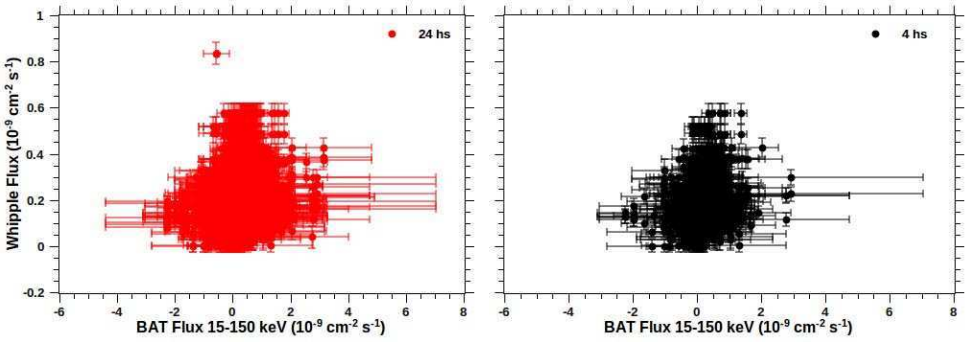

Figure 5.13: Flux-flux plot for VHE γ-ray with Whipple and hard X-ray with BAT for Mrk 421. Black points correspond to 4hrs and red points to 24 hrs coincident time bins, respectively.

the VHE vs. BAT flux (Figure 5.12).

Figure 5.16 shows the DCF between the VHE and soft X-rays light curves. An average correlation of R $\sim$0.2 between the two light curves at 0 days lag was found. The two big peaks at +40 days and $-$35 days arose almost entirely due to the giant VHE outburst, which was preceded and followed by X-ray flares near the end of the campaign (MJD 54550-54560).

It is possible to assume from the DCF and the flux-flux correlation plots be-

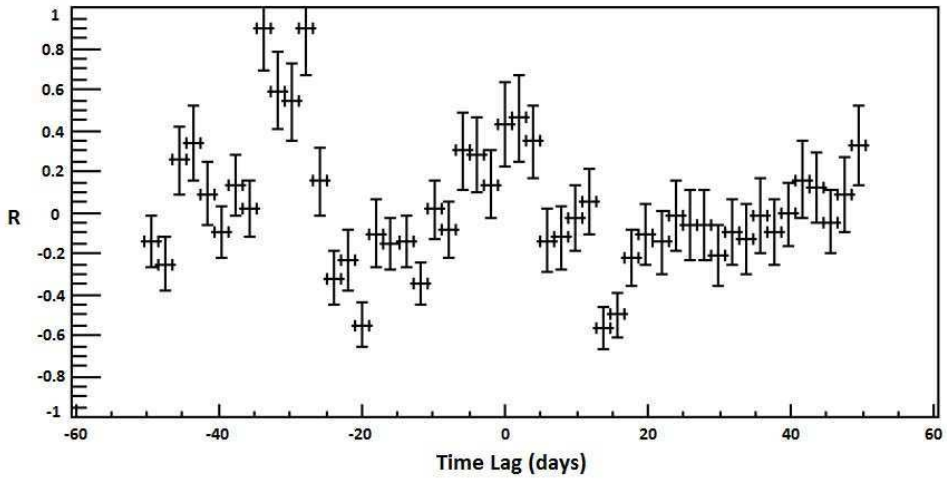

Figure 5.14: DCF plot for VHE γ-ray with VERITAS and BAT for Mrk 421.

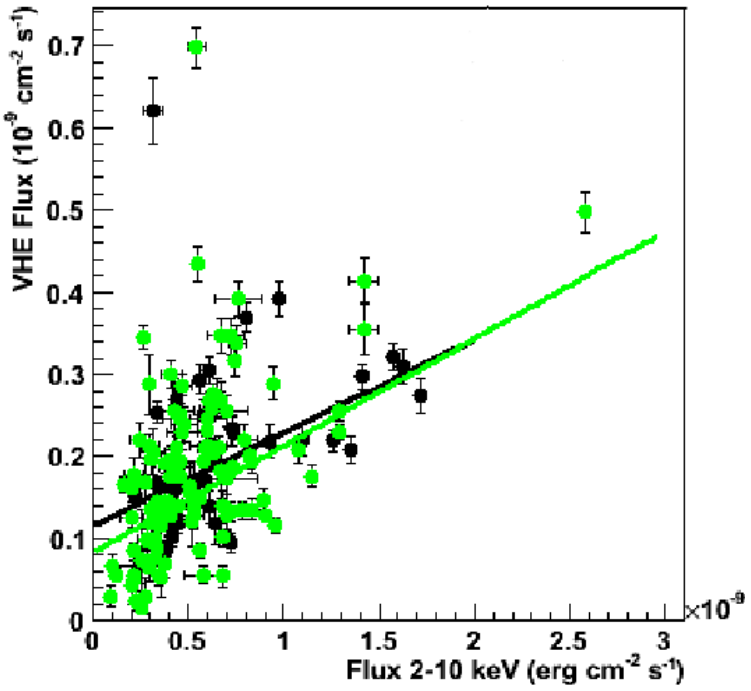

Figure 5.15: Flux-flux plot for VHE γ-ray and soft X-ray for Mrk 421.

tween VHE gamma-rays and X-rays, that the "orphan" VHE flare might be present even though there was no simultaneous observations in both bands.

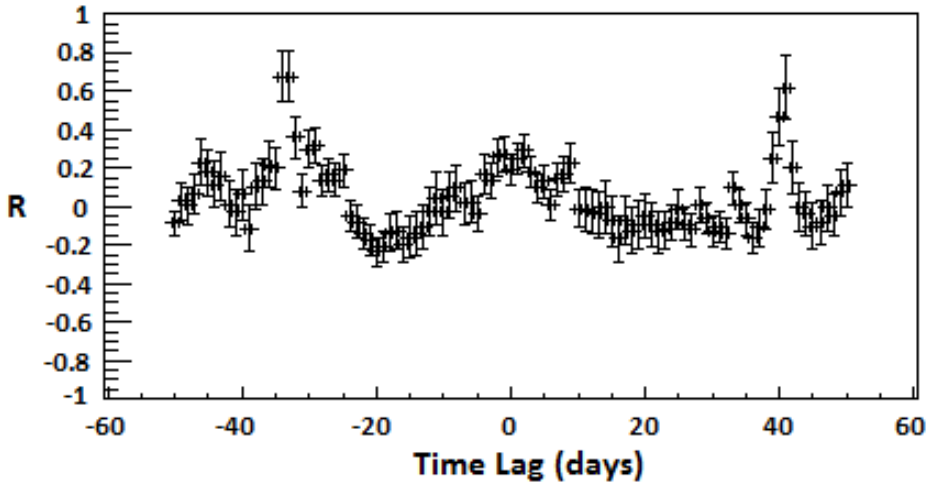

Figure 5.16: DCF plot for VHE γ-ray and soft X-rays.

5.2.2 Markarian 501 in 2008

Figure 5.17 shows the fractional variability as derived for each instrument involved in the multi-wavelength campaign. Only daily averages for each instrument were taken. The variability is significant for several energy bands, being 14 % for the X-rays and $\sim$ 27 % for the VHE gamma-rays. In spite of large errors, it can be seen that the variability is higher for the highest energies. Optical and radio bands showed no evidence of variability.

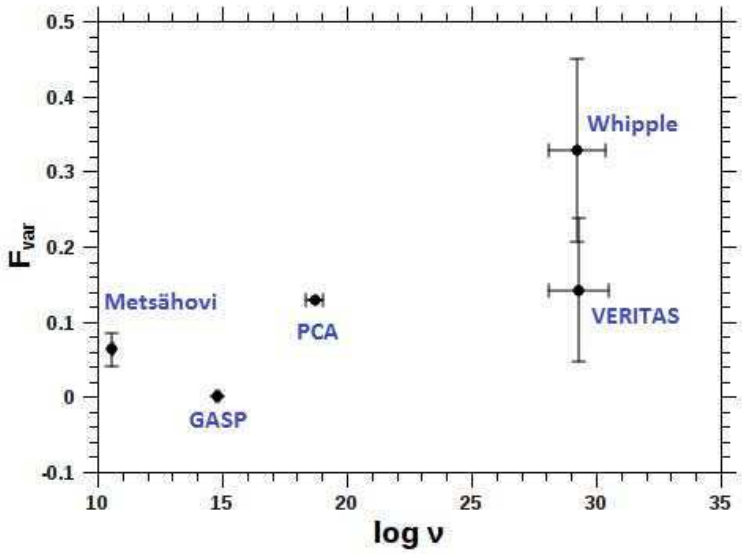

Figure 5.17: Fractional variability amplitude for all the instruments involved in the mwl Campaign in March-May 2008 of Mrk 501.

The evolution of the variability could be explained in a SSC scenario; the variations were produced by the injection of energetic particles, which were characterized by short time scales, being responsible for the high variability amplitude at the highest energies.

In the VHE domain, the behavior of the flux measured by the Whipple 10 m telescope was not similar to that observed by VERITAS, which can be seen in Figure 5.6. Whipple measurements showed more variability and a higher baseline. In order to compare both observations a flux-flux plot with a coincident time line of 0.1 days was built, as it is shown in Figure 5.18. There is no evidence of correlation, probably because the fluxes and the variabilities were too small to show up using these kind of studies. A linear fit was performed and it is also shown in Figure 5.6. A constant fit is also possible with similar probability.

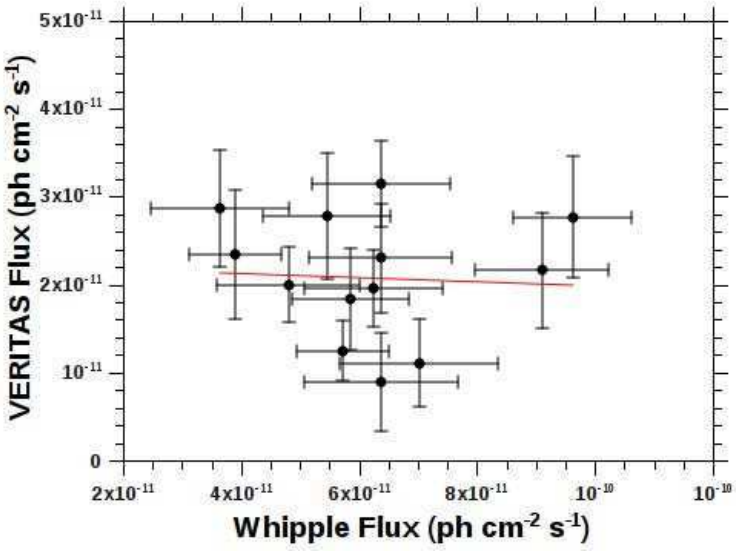

Figure 5.18: Flux-flux plot for the VHE gamma-rays, VERITAS and Whipple Telescope, looking for correlations. The red line is the linear fit.

Considering that a clear evidence of variability was observed only for the X-rays and VHE gamma-rays, finding a correlation between them would be important to give some constraints to the emission model. Then, a flux-flux plot with a time window of 0.1 days was done, as shown in Figure 5.19. Again, there is no sign of evidence of a correlation between both bands.

Some delay might have been present between both emissions, a multi-frequency cross-correlation study, using the DCF (see equation 5.6) for the X-ray and VHE gamma-ray bands was done. In this case, it can be noticed from Figure 5.20, that a significant correlation was found only with the DCF maximum located at zero time lags, showing a value of 0.5 ± 0.12. Due to the modest flux variability and/or the large flux error, no major conclusions can be done.

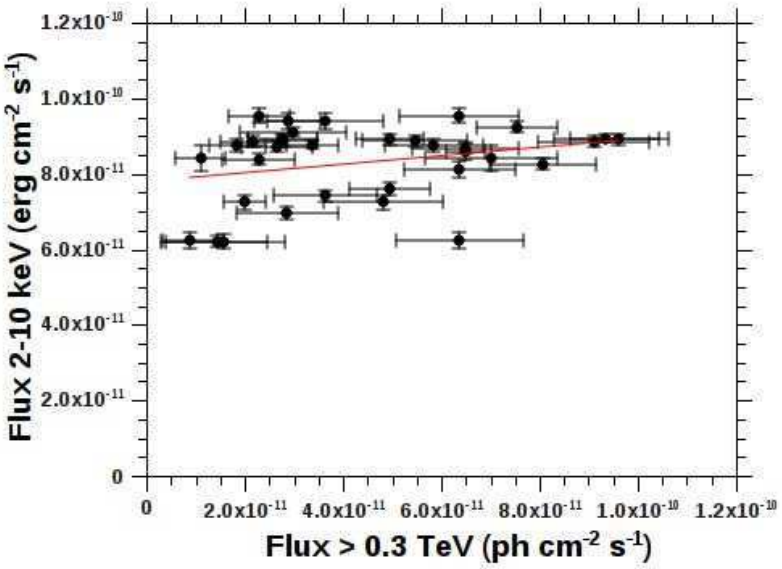

Figure 5.19: Flux-flux plot for the VHE gamma-rays compared to the X-ray with RXTE-PCA. The red line is the linear fit.

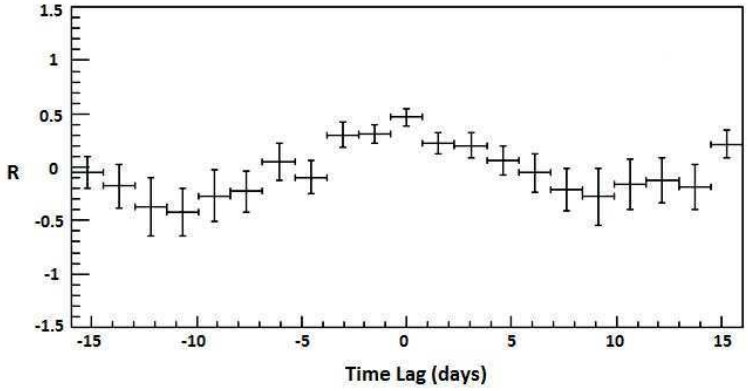

Figure 5.20: DCF for the X-ray 2-10 keV versus VHE gamma-ray.

5.2.3 Markarian 501 in 2009

Figure 5.21 shows the $F_{\rm var}$ values obtained for all the involved observations using a daily average for each energy band. *Fermi*-LAT was excluded because it shows a negative excess ($\overline{\sigma}^2 > S^2$), thus indicating a low level of variability and/or overestimated errors. Essentially such a result can be interpreted as no signature for variability, because either there was no variability or the instrument was not sensitive enough to detect it.

As seen in the figure, the value of $F_{\rm var}$ is very low or compatible with zero for all the energy bands except for the VHE range, where $F_{\rm var}$ is 0.62 ± 0.01 for VERITAS and 0.95 ± 0.01 for Whipple. The large variability in the VHE domain is clearly

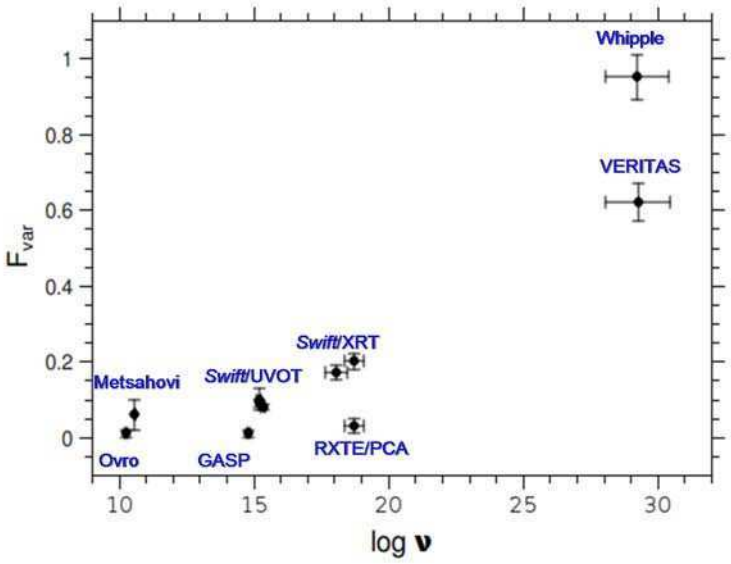

Figure 5.21: Fractional variability amplitude for all the instruments involved in the mwl Campaign in 2008-09 of Mrk 501.

dominated by the high VHE flare observed on MJD 54952 and the following few days.

The variability correlations between different energy bands can indicate the type of emission processes involved, and can provide constraints on the models. In the past, a correlation between X-ray and γ-ray emission was found (Katarzyński et al. 2005, Krawczynski et al. 2002), indicating that the same population of electrons was responsible for both emissions. In this work, the relationship between the VHE γ-ray with the X-ray was studied through a flux-flux plot. The results are shown in Figure 5.22 (bottom) for Whipple 10 m and *Swift*-XRT in the lower band (where the $F_{\rm var}$ is 0.17) for measurements within one day. There is evidence for correlated variability throughout all the period, except for the night of the flare. A linear fit was made obtaining a χ^2/NDF of 0.02, a correlation factor of $r = 0.94$ with a slope of 1.39 ± 0.16.

Swift-XRT observations for the night of the flare were not simultaneous but contemporaneous (7 hours later) with VHE observations and did not show any increase in the flux. The flux in the 2-10 keV band showed an increase of about 50 % during the days following the VHE flare, but this flux enhancement was substantially smaller than the one seen by Whipple and VERITAS during the same days. In order to investigate the relationship between the X-ray and the VHE γ-ray bands, the DCF was calculated and it showed negative results, not indicating a significant correlation between both datasets. It can be concluded that this VHE flare was likely to be an "orphan" flare (in the sense of not being accompanied by an X-ray flare), like the one that was previously detected on 1ES 1959+650 (Krawczynski et al. 2004). Or, alternatively, the X-ray flare did exist, but it was substantially smaller than that seen at VHE, as it occurred for

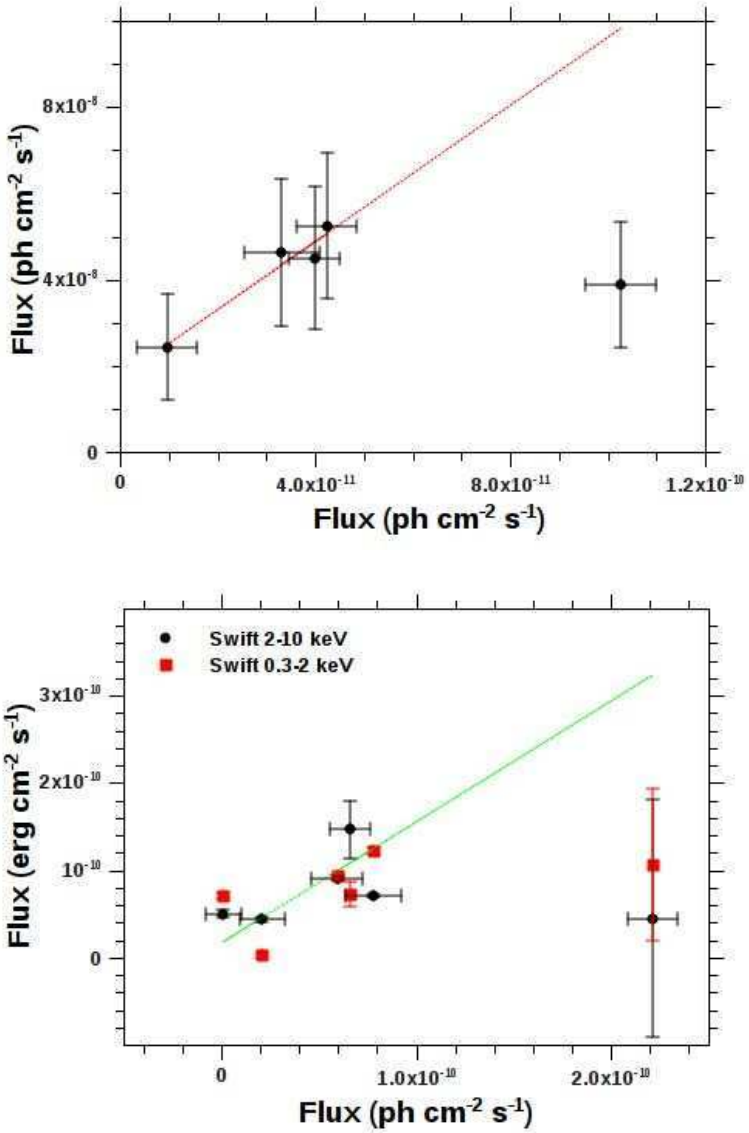

Figure 5.22: Flux-flux plot for VHE γ-ray and HE γ-ray (*Top*); VHE γ-ray and X-ray (*Bottom*) where only pairs within 24 hours of each other were used. The dotted lines are the best fits excluding the isolated point corresponding to the VHE flare.

PKS 2155-304 in 2006 (Aharonian et al. 2009).

At the GeV band the source remained steady with no variations during the days of high activity. A flux-flux correlation plot was made in order to investigate if the same population of electrons are responsible for the emission for the HE and VHE bands. It was the first time for this source to have simultaneous observations in low and high states of activity in the HE and VHE γ-ray bands with *Fermi*-LAT and Whipple/VERITAS, respectively. The results are shown in Figure 5.22 (top) where no sign of correlation is found and the fit is shown as a guide to the eye. This kind of analysis needs to be done with a larger sample, such as the entire data

set of the mwl campaign (4.5 months) in order to have enough statistics to detect the source, due to the low sensitivity on the 5-day scale used by *Fermi*-LAT.

5.3 Spectral Energy Distribution

Flaring episodes in blazars also enable the study of spectral evolution. Blazars have shown spectral features depending on the flux-level state. A clear hardening of the spectrum when the flux level increases has been noticed before in some blazars. Spectral evolution is important to understand how the acceleration mechanism occurs in the jets.

5.3.1 Markarian 421 in 2007-08

Figure 5.23 shows the Mrk 421 energy spectra from VERITAS corresponding to the nights of the VHE flares (May 2-3, 2008). For the night of May 3, the light curve was divided into two parts and two separated spectra were calculated. The division was made by considering the highest runs (very high state) in comparison to the lowest ones of this night flare itself (high state).

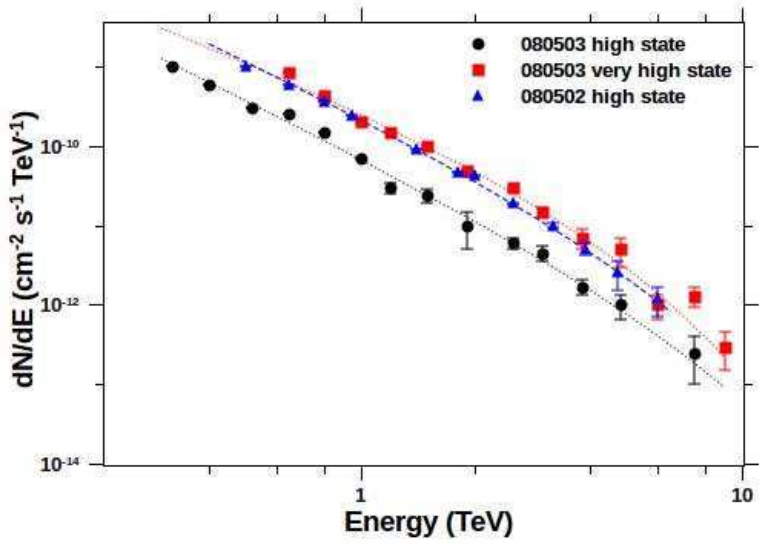

Figure 5.23: Spectrum of Mrk 421 obtained with VERITAS during the nights on May 2 and 3, 2008.

For each subset, the energy spectrum was derived, and fitted by a power-law function with exponential cutoff of the form:

$$\frac{dN}{dE} = I_0 \times 10^{-11} \ (E/1 \text{ TeV})^{-\Gamma} \exp(-\text{E}/\text{E}_{\text{cut}}) \ \text{ ph cm}^{-2} \text{ s}^{-1} \text{ TeV}^{-1}. \qquad (5.7)$$

A fit of a simple power-law function was done, getting a very low correlation factor, and this functional form can be excluded with high confidence for most of the spectra. The results of the fits are summarized in Table 5.5. This fit including a power-law function with an exponential cutoff was used before in Acciari et al. (2011).

	I_0	Γ	$E_{\rm cut}$	χ^2/NDF
030508 very high	8.10 ± 0.57	1.87 ± 0.17	2.74 ± 0.60	6.2/9
030508 high	35.77 ± 3.08	2.33 ± 0.12	5.40 ± 1.10	10.1/9
020508 high	27.10 ± 3.88	2.25 ± 0.21	4.10 ± 2.50	11.7/9

Table 5.5: Best-fit parameters for VERITAS data.

Clear indications for spectral hardening with increasing flux levels were found in the TeV band as it can be seen in Figure 5.23. A similar trend had already been found in earlier Whipple data of Mrk 421 (Krennrich et al. 2003).

5.3.2 Markarian 501 in 2008

The light curve of Mrk 501 during March-May 2008 at the VHE range was divided into two periods in order to look for TeV spectral variability. Periods were separated by taking the activity in the X-ray band into account, thus, the first period was considered from MJD 54550 to 54574, and the second period from MJD 54574 to 54602. For each period the energy spectrum was calculated and modeled with a simple power law as in equation 1.2. Results are shown in Figure 5.24.

The best-fit parameters and associated errors for the VHE data are summarized in Table 5.6.

	F_0	Γ	χ^2/NDF
MJD 54550-54574	0.70 ± 0.01	2.41 ± 0.16	5.2/7
MJD 54574-54602	0.75 ± 0.02	2.25 ± 0.24	2.1/5

Table 5.6: Best-fit parameters for VHE data.

There was no evidence of any hardening of the spectra between both periods.

The broadband SED of Mrk 501 for three different time periods, together with some historical data from the 2005 low and high states are shown in Figure 5.25. No difference can be noticed between the defined low and high states in the VHE domain, although a very small difference between both states can be found in the X-ray band. It can be seen how the SED changes during periods of high and low activity in different years. Thus, given the variability present in the source it is possible to obtain different values of the physical parameters involved, like the magnetic field and the emission region. During different years, then, similar

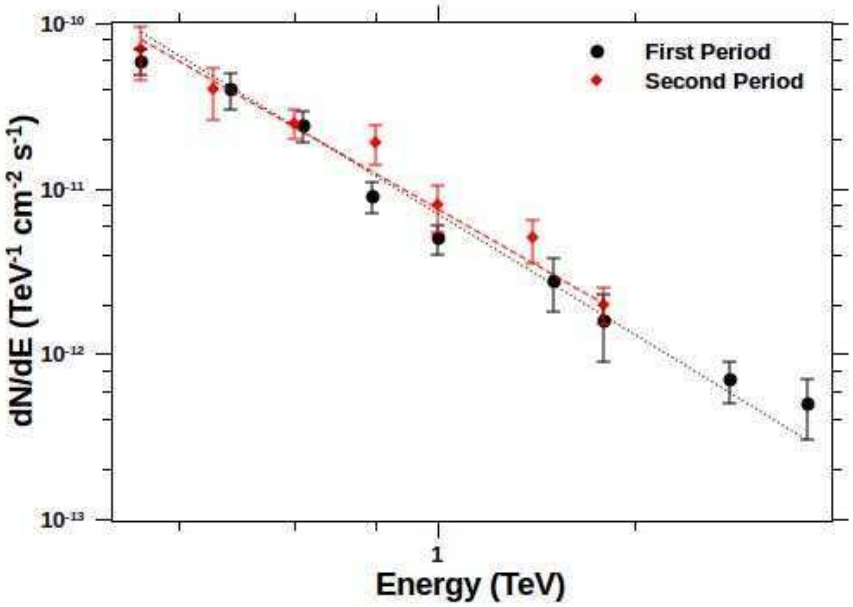

Figure 5.24: Time-averaged VHE photon spectra of Mrk 501 for discrete flux levels for the period MJD 54550-54574 (*first period*) and for the period MJD 54574-54602 (*second period*).

parameters are not obtained for the same state of the source, and it might be difficult to get any assumption about the physical parameters involved.

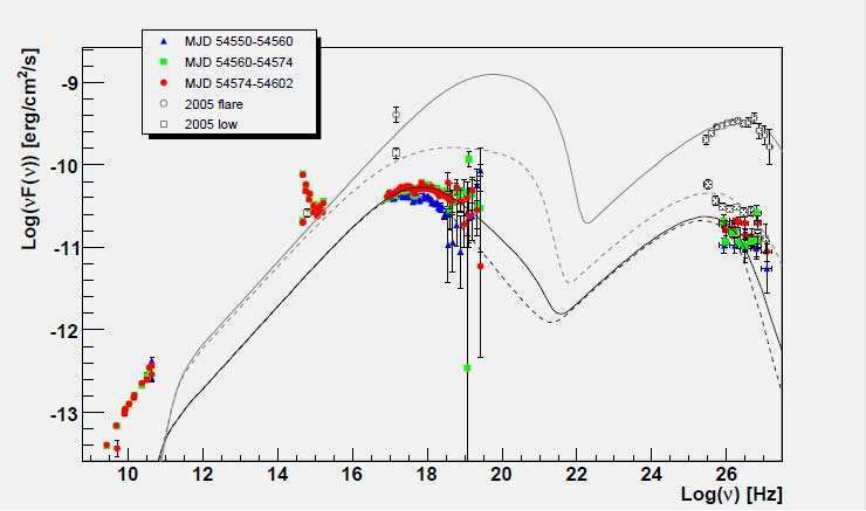

Figure 5.25: SED of Mrk 501 obtained during the mwl campaign in March-May 2008. Results obtained with the SSC model fit to the first (black dot-dashed curve) and the second period (black heavy-dashed curve) are shown. The 2005 low state (grey light-dashed curve) and the 2005 high state (grey solid line curve) are also shown for a comparison purpose. Figure taken from Kranich et al. (2009).

The broadband SED for Mrk 501 in both periods of the mwl campaign were ob-

tained and modeled by taking one-zone synchrotron-self-Compton model (Tavecchio et al. 1998). The model is based on a spherical emission region with radius R, a Doppler factor δ, a magnetic field of strength B, an electron distribution (density K) following a broken power law with slopes n_1 and n_2 and break energy $\gamma_{\rm break}$. The values of the parameters obtained by fitting the model for the two different emission states are given in Table 5.7. Given the small differences between the two states, only some small changes were applied to the SSC model to reproduce the data. For more detailed information and results about this model see Kranich et al. (2009).

	2008 First period	2008 Second period
$\gamma_{\rm break}$	$2.6 \cdot 10^5$	$2.2 \cdot 10^5$
n_1	2.0	2.0
n_2	3.9	4.2
B [G]	0.19	0.19
K [cm^{-3}]	$1.8 \cdot 10^4$	$1.8 \cdot 10^4$
R [cm]	$3 \cdot 10^{15}$	$3 \cdot 10^{15}$
δ	12	12

Table 5.7: The SSC model parameters used to describe the broadband SED for different flux states observed during the campaign. Table taken from Kranich et al. (2009).

The high emission state was satisfactorily modeled by increasing the amount of high energy electrons with respect to the low emission state. This parameterization is consistent with the energy-dependent variability trend observed during the campaign.

5.3.3 Markarian 501 in 2009

To study the evolution of the TeV energy spectrum during the short flaring state of Mrk 501 it is necessary to understand the mechanism of particles acceleration in a blazar source. The differential energy spectra of Mrk 501 obtained with the Whipple telescope and VERITAS are shown in Figure 5.26. They were modeled in each case, for the quiescent emission and for the flare state, with a simple power law as in equation 1.2. The best-fits are also shown in Figure 5.26 and the parameters and associated errors for the VHE data are summarized in Table 5.8. A marginal indication of spectral hardening with increasing flux activity was found for the TeV band. A similar trend had already been found in previous observations during 2005 with MAGIC (Albert et al. 2007). The softest photon index was 2.43±0.05 (for the low/medium state), and the hardest photon index was 2.09±0.03 (for the flare on MJD 53551).

The spectral results obtained for the high state (MJD 54952-55) of Mrk 501 during the three-week period are plotted in Figure 5.27. For comparison purposes,

	MJD Interval	F_0	Γ_{VHE}	χ^2/NDF
Whipple very high	54952.35-54952.41	16.1 ± 0.4	2.10 ± 0.05	13.48/8
Whipple high	54952.41-54955	5.6 ± 0.4	2.31 ± 0.11	3.10/8
Whipple low	54936-54951	1.16 ± 0.09	2.61 ± 0.11	3.40/8
VERITAS high	54952-54955	4.17 ± 0.24	2.26 ± 0.06	6.26/5
VERITAS low	54907-55004	0.88 ± 0.006	2.48 ± 0.07	3.76/5

Table 5.8: Best-fit parameters for VHE data.

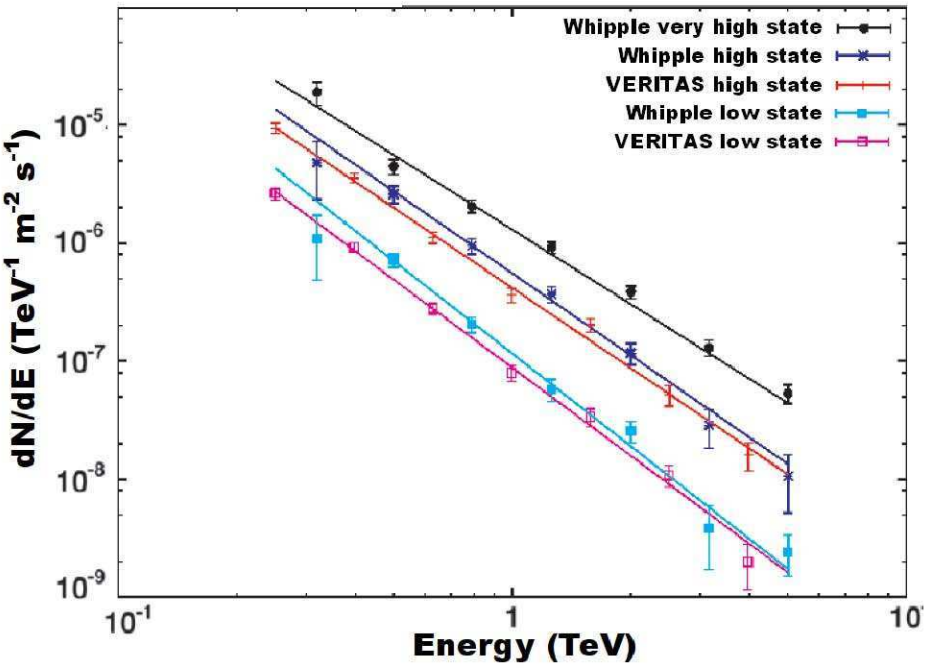

Figure 5.26: Time-averaged VERITAS and Whipple photon spectra of Mrk 501 for discrete flux levels (see text).

the average spectrum for the whole 4.5 months mwl campaign (Abdo et al. 2011a) including the three-week period is plotted. Figure 5.27 clearly shows that the largest variation in the emitted flux occured in the VHE domain.

The SED modeling was carried out by using a pure SSC model, based on Böettcher & Chiang (2002). The equilibrium version of the model is described more thoroughly in Acciari et al. (2009). In this model, the spectral distribution of relativistic electrons assumes a power-law distribution between a minimum energy, γ_{min}, and a maximum energy, γ_{max}, with power-law index q injected, and then evolves to equilibrium between injection, radiative cooling and escape. The emitting region of comoving radius R_B moves along the jet with a relativistic speed β, and the particles cool due to radiative losses and then might escape from the region. The viewing angle θ, between the jet direction and the line of sight, is

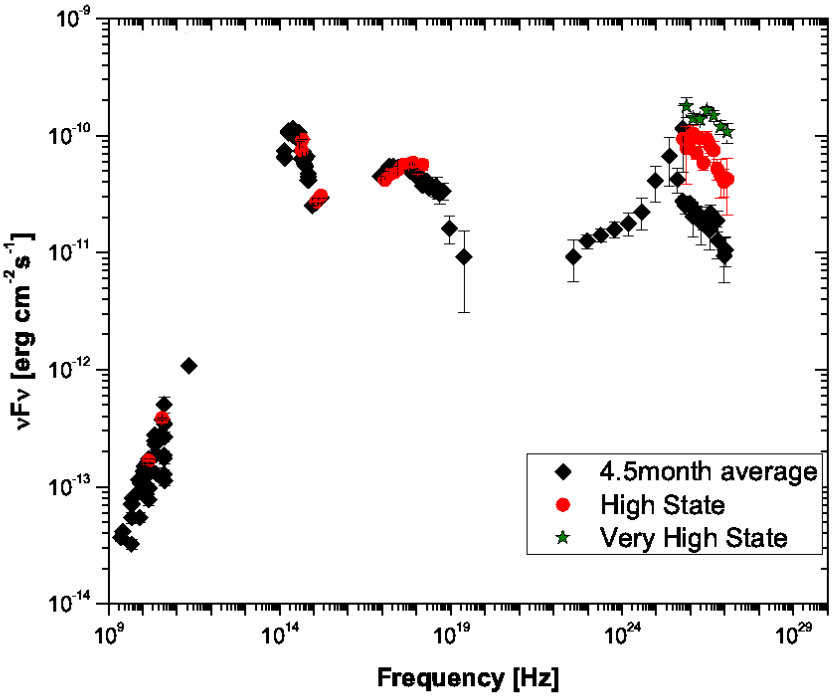

Figure 5.27: Spectral energy distribution of Mrk501 during the interval MJD 54952-54955 (depicted with circles), and the VHE spectrum measured by Whipple on MJD 54952 (depicted with green stars). For comparison purposes, the 4.5-months averaged SED from the entire campaign (extracted from Abdo et al. 2011a) is also shown.

set to be the superluminal angle, from where the bulk Lorentz factor Γ equals the Doppler factor $\delta = (\Gamma[1 - \beta cos\theta])^{-1}$.

For the fits to Mrk 501, only synchrotron and SSC were included, as that is usually sufficient for the two SEDs of Mrk 501 presented here. It can be noticed, that both states required far sub-equipartition magnetic fields (1×10^{-4} for the high state; 2.35×10^{-3} for the low state). The transition between the two states could not be achieved by changing only one or two parameters. The size of the emission region remained the same, then it was necessary to change the Doppler factor, the high-energy cutoff of the injected electron distribution ($\gamma_{\rm max}$), the electron injection index q and the magnetic field. To account for the optical emission of the host galaxy, a thermal blackbody core was added to fit the data, obtaining a much better overall fit. The values for the model parameters are shown in Table 5.9. The SED of Mrk 501 for the low state (MJD 54936-54951) and high states (MJD 54952-55) are shown in Figure 5.28. The results from the SSC model fit to low and high state are also plotted in Figure 5.28. It can be noticed from the figure that the spectral variability was seen in the highest energies of the spectral energy distribution, remaining the same at lower energies. In order to get the best fit to the high-state, it was necessary to reduce by one order of magnitude the

magnetic field and to increase the Lorentz factor.

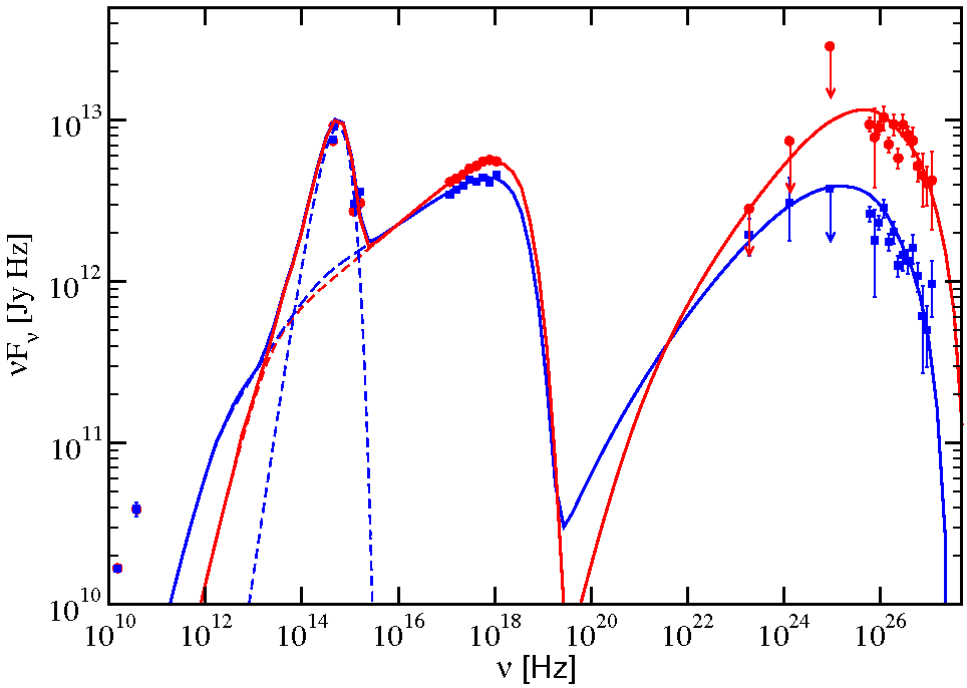

Figure 5.28: Spectral energy distribution of Mrk501 for the low state (MJD 54936-54951; blue squares) and high state (MJD 54952-55; red circles) of the three week period. The SSC model fit for low (blue solid line) and high (red solid line) states is also shown.

Parameters	Low State	High State
$\gamma_{\rm min}$	1×10^{4}	1×10^{4}
$\gamma_{\rm max}$	1.2×10^{6}	2×10^{6}
Injection electron spectral index	1.6	1.5
Escape time parameter ($t_{\rm esc} = \eta R/c$)	1000	1000
Magnetic field at z_0[G]	0.03	0.0075
Lorentz Factor	20	30
Blob radius [cm]	1.2×10^{16}	1.2×10^{16}
Observing angle [degrees]	2.866	1.91
L_e [erg s^{-1}]	8.27×10^{43}	2.53×10^{44}
L_B [erg s^{-1}]	1.94×10^{41}	2.73×10^{40}
L_B/L_e	2.35×10^{-3}	1.08×10^{-4}

Table 5.9: SED model parameters.

Chapter 6

Conclusions

The last twenty years were marked by a rapid development in the field of ground-based very-high-energy (VHE) gamma-ray astronomy, since the first confirmed source of VHE γ-rays was detected in 1989 by the Whipple 10 m telescope. Nowadays, the total number of detected sources exceeds 130, and four major third-generation ground-based observatories are currently operational. However, the physical processes involved in VHE emission are still not well understood and far from being resolved. Several leptonic and hadronic models have been tested so far trying to explain the radiative mechanisms, but the observations do not yet sufficiently constrain them.

In this work a contribution to the general problem of VHE gamma-ray emission is made from the observational point of view, focusing on the problem of the non-thermal radiation production for extragalactic sources. In particular, the well known blazars Markarian 421 and Markarian 501, the first two detected extragalactic sources, were studied. Due to the complexity of the spectral energy distribution (SED) of these kind of sources, multi-wavelength observations were used to complement the VHE observations carried out specifically for this purpose with the Whipple 10 m telescope and the VERITAS system.

The work has two main parts. The first one is dedicated to the Whipple 10 m telescope in the framework of the "blazar monitoring program", its calibration, pointing corrections and energy spectra determination in order to analyze the time behavior of the two blazars under study. The second part is dedicated to the multi-wavelength analysis searching for variability and correlation of the VHE observation with other wavebands.

Regarding the Whipple 10 m telescope and the monitoring program, in this work the development of methodologies for calibration and analysis of Whipple data were performed. A search of Hillas parameters was undertaken in order to increase the signal-to-noise ratio using a data set taken in the 2008-09 season on the Crab Nebula, which was already known to have a significant gamma-ray excess. By applying the single parameter variation method outlined in Chapter 4, the cuts used to select gamma-ray events were optimized. Re-analyzing the remaining data from the Crab Nebula, an improvement of 30 % of the total significance was achieved. Then, those cuts were applied to all other data taken during that

season with the Whipple telescope, getting an improvement of 18 % and 5 % in the detection significance of Mrk 421 and Mrk 501, respectively.

In the 2007-08 season, the Whipple 10 m telescope presented a systematic pointing offset. Several studies were conducted with the observations of bright stars, in order to find the relationship between the pointing offset as a function of telescope elevation and azimuth angles. As expected, the dependence was found mainly on the telescope elevation. Then, a software correction was applied to the analysis package and the sensitivity of the analysis was improved. In addition, an alternative method was developed in an attempt to correct the mis-pointing of the telescope for archival data. This method consisted of building a 2D histogram with the direction of the major axis of the image for each event and searching for the apparent source location by identifying the bin with more lines intersecting. The pointing correction was given by measuring the angular distance between that hotspot and the center of the camera. This method was successfully applied to the Mrk 421 flare in May 2008. This proved that the method might be useful for old data taken before the installation of the pointing monitor system. The drawback of this method is that it needs to be used for strong VHE sources, such as the Crab Nebula or Mrk 421, or only for periods with high activity in order to correctly determine the position of the hotspot in the 2D histogram.

One hundred thousand Monte-Carlo gamma-ray showers were simulated with an elevation angle of 70° and an azimuth of 45°, under similar conditions to most of the Whipple 10 m observing data. Then, the emitted Cherenkov light produced by the charged particles passing through the atmosphere was simulated until it reached ground. Finally, the detector response was simulated. These three steps were made in order to reconstruct the energy for the primary gamma-ray. Simulated gamma-rays produced image parameters similar to those taken with real data. Then, Crab Nebula was used as a calibration source due to its strong and steady emission in the VHE domain. The energy spectrum of the Crab was reconstructed for the 2008-09 data with compatible results to those previously presented in the literature. This result allowed the use of the same simulation process to reconstruct the Mrk 501 energy spectra for data taken in April-May, 2009, for both the low and high state of activity.

The results of the VHE blazars Mrk 421 and Mrk 501 data taken from 2007 to 2009 as part of several multi-wavelength campaigns, including the Whipple 10 m telescope and VERITAS array, are described. Light curves in daily and 30-minutes time scales were presented showing variability in almost all wavebands. A systematic search for short time scale variability of the data was done, yielding one big flare for each source with high significance and high intra-night variability, whose rise/fall time scale was in the range 30-50 minutes. No hint of long/short periodicity was found for any source in the VHE domain from these observations, even though there have been various reports indicating possible periodicity or quasi-periodicity (week-month time scales) in these two sources. The broadband temporal variabilities of Mrk 421 and Mrk 501 were examined by computing the fractional RMS variability amplitude ($F_{\rm var}$). Significant variability was detected

consistently throughout all the campaigns.

During the 2007-08 observing season, Mrk 421 presented high activity for almost the whole period with an average flux level of around 1.5 times the Crab Nebula. The highest night-averaged flux level detected during this campaign was the night of May 2 with a flux level around 5 Crab, with an unprecedented maximum peak of 15 Crab observed by the Whipple 10 m. After the peak, the flux decreased by more than a factor of two in two minutes and then increased again by almost the same factor in five minutes. This short intra-night variability was not simultaneously (or quasi contemporaneously) observed at any other wavelength.

The highest variability was found in hard X-rays although significant variability was also found in the VHE band. The $F_{\rm var}$ amplitude was similar to that obtained in previous multi-wavelength campaigns. This might suggest that the variability level of the source relative to its mean flux level remains constant, regardless of flare amplitudes or the activity of the source.

Correlation between blazar emission in the X-ray and the VHE energy band, including the investigation of time lags between the different energy regimes, was studied for Mrk 421. Significant evidence of a correlation between X-rays (2-150 keV) and VHE fluxes was found except for the night of the VHE flare. No significant flux correlations between the VHE band and the remaining bands were found, which indicates that the emission in those bands and the X-ray/VHE-γ-ray emissions were not from the same region. This might also indicate that the optical/radio emission is dominated by a region larger than the VHE emission region and/or different emission mechanisms for each regime are present. To further explore the energy dependence in variability, a discrete correlation function analysis was introduced. The correlation between gamma-ray and X-ray light curves in Mrk 421 was found to be modestly significant with R$\sim$0.2 at zero-lag day. Both big peaks found, at +40 days and $-$35 days, arose almost entirely due to the giant VHE outburst which was preceded and followed by X-ray flares near the end of the campaign.

In the case of the first multi-wavelength (mwl) campaign of Mrk 501 from March to May, 2008, this source remained in a low activity state for the whole campaign, with a low gamma-ray emission around 20 % of the Crab Nebula. No outburst was observed at any energy although the source showed some level of variability, mostly in the X-rays and VHE gamma-rays, which increased at higher energies (as expected in a SSC scenario) presumably due to the faster cooling times of the most energetic electrons. A search was made looking for short time correlations (few hours) to long time correlations (few days) between the X-ray and VHE gamma-ray bands. Some variability was detected using the DCF method at zero-time lag but a flux-flux plot did not show any correlation within less than 0.1 days. The low flux recorded and the low variability (compared to other epoches) cannot allow us to make any further comment.

An energy spectral variability was also investigated, for which the data were divided into two periods. The spectral index was similar and no hard spectrum was found in these observations from any of both periods.

In the case of Mrk 501 during the 2009 mwl campaign, a general trend of increasing $F_{\rm var}$ towards higher frequencies was observed. The radio and optical data exhibited very low variability while the X-ray and gamma-ray data had high fractional RMS variability amplitudes. This trend was more obvious for Mrk 501 during the 2009 season (compared to 2008) because there was a quite high activity state at VHE observed by Whipple and VERITAS for several days. Considering that these instruments observed a flux enhancement by a factor greater than 5, it was reasonable to assume that the VHE flare lasted more than 3 hours, and hence, that *Swift* observations might have occurred during this outstanding VHE state. Given that this source is known to have very fast variability, and not having strictly simultaneous observations between X-rays and VHE γ-rays, a possible association to an "orphan" flare can be made. However, the data were too sparse for a definite claim in this regard. Variability time-scales in flux and energy spectrum change during flares and can be interpreted in terms of the electron cooling time, the electron acceleration time, and the light crossing time, in order to understand the underlying physical properties of the jet. The unpredicted short time variability of flares strongly supports the leptonic origin of the VHE emission.

Observations of the optical linear polarization and the electric-vector position angle (EVPA) were undertaken during the VHE flare. As these events can be physically linked, the correlation between the gamma-ray and the optical polarized flares might indicate that both emissions were produced at the same location, and so have a common origin, as it occurred during several other outbursts reported recently. Then, this event could have been produced by a single blob passing through a standing shock after going through the acceleration and collimation zone of the jet (where the polarization angle rotated).

A significant correlation was found between X-rays (2-10 keV) and VHE γ-rays. No significant correlation was found with the remaining wavebands, indicating that the emission regions were not the same. Although there was no correlation with the optical flux, a significant correlation with EVPA was obtained, as mentioned above, so an explanation might have been found for this flare. Fermi-LAT flux did not show much variability in the three-weeks period of observation, which may be attributed to the relatively low sensitivity on the 5-day time scale duration of the flare. As such, no significant correlation between the VHE γ-ray and HE γ-ray bands was obtained, which might indicate that the same population of electrons is not responsible for both emissions, or that Fermi-LAT was not sensitive enough.

The physical parameters that govern the blazar SED were constrained by obtaining a well-sampled SED for both sources studied in this work, combining observations at different wavelengths with sufficient statistics. With such complete data on Mrk 501 in the 2008 and 2009 seasons, broadband variability in the spectrum was seen, and the parameters of synchrotron-self Compton model could be determined from the spectral energy distribution by fitting a one-zone SSC model.

For the mwl campaign undertaken in 2008, it was necessary to use a low Doppler factor ($\delta = 12$), a low magnetic field ($B = 0.19\,$Gauss) and an emission region of about $3 \times 10^{15}\,$cm. The main differences between these param-

eters and those from the campaign undertaken in 2009 were that in the latter, the Doppler factor was bigger (20-30), the magnetic field was even lower ($B = 0.03 - 0.0075$ Gauss) and the emission region was larger (about 1.2×10^{16} cm). In any case, there are too many free parameters to find a unique solution or draw definitive conclusions.

Further progress in the understanding of the jet physics requires simultaneous VHE observations with other wavebands, specially HE and X-rays. The complexity in the underlying processes occurring in sources like Mrk 421 and Mrk 501 can only be solved through an intense, well-sampled, coordinated multi-wavelength monitoring lasting for several consecutive years, an effort that would be difficult to organize. The next generation of Cherenkov systems might become the solution to this and other kinds of problems. The Cherenkov Telescope Array (CTA) is being planned as a system of several ten telescopes, with one order of magnitude more sensitivity and a much better angular resolution. CTA will open a new era in ground-based gamma-ray astronomy and might allow us to see what nature is vealing, the mechanisms behind the blazars systems and many other interesting astronomical objects.

Bibliography

Abbasi, R. et al. 2011, Phys. Rev. D84, 082001

Abdo, A. A. et al. 2010, Nature 463, 919

Abdo, A.A. et al. 2011a, ApJ 727, 129

Abdo, A.A. et al. 2011b, ApJ 736, 131

Abramowski, A. et al. 2012, A& A 537, 114

Acciari, V.A. et al. 2009, ApJ 707, 612

Acciari, V.A. et al. 2011, ApJ 738, 25

Acciari, V.A. et al. 2009, Nature 462, 770

Acciari, V.A. et al. 2011, ApJ 729, 2

Acciari, V.A. 2010 Ph.D. Thesis

Acero, F. et al. 2009, Science 326, 1080

Aharonian,F. et al. 1991, Proc. 22nd ICRC, Dublin, Ireland

Aharonian, F. & Atoyan, A.M. 2000, A&A, 362, 937

Aharonian, F. et al. 2005, Science 307, 1938

Aharonian, F. et al. 2006, A & A 457, 899.

Aharonian, F. et al. 2007a, A& A 467, 1075

Aharonian, F. et al. 2007b, ApJ 664, L71

Aharonian, F. et al.2009, A&A 502, 749

Aharonian, F. 2000, NewA, 5, 377

Aharonian, F. 2004, *Very high energy cosmic gamma radiation: a crucial window on the extreme Universe*, World Scientific Publishing, New York

Akerlof, C. W et al. 1991, ApJ 377, L97

Albert, J. et al. 2006, ApJ 648, L105

Albert, J. et al. 2007, ApJ 669, 862

Aliu, E. et al. 2012, paper in preparation (A. Pichel corresponding author)

Atoyan, A. & Dermer, C. D. 2003, ApJ 586, 79

Atwood, W.B. et al. 2009, ApJ, 697, 1071

Avni, Y. 1976, ApJ 210, 642

Barres de Almeida et al. 2011, Proc. 32th ICRC, Beijing, China

Baumgartner, W. et al, 2010, HEAD 41, 675

Beall, J.H. & Bednarek, W. 1999, ApJ, 510, 188

Begelman, M. C., Fabian, A. C. and Rees, M. J. 2008, MNRAS 384, L19

Beloborodov, I.S. 2004 ApJ 618, L13

Böttcher, M. et al. 1997, A&A, 324, 395

Böettcher, M. and Chiang, J. 2002 ApJ 581, 127

Böttcher, M. 2005, ApJ 621, 176

Burrows, D.N., et al. 2005, Space Science Reviews, 120, 165

Catanese, M. et al. 1998, ApJ, 501, 616

Cawley, M.F. et al., 1990, Experimental Astronomy 1, 173

Chaves, R.C.G. et al. 2008, Proc. 4th Int. Meeting on High Energy Gamma-Ray Astronomy, AIP 1085 372

Cogan, P., 2006, Ph.D. Thesis, University College Dublin

Cogan, P. 2007, Proc. of the 30th ICRC, Mérida, Mexico

Dar, A. & Laor, A. 1997, ApJ, 478, L5

Davies, J.M. & Cotton, E.S. 1957, Solar Energy 1, 2-3 (April-July), 16

Djannati-Atai, A., Piron, F., Barrau, A., et al. 1999, A&A 350, 17

de la Calle Perez, I., et al. 2003, ApJ, 599, 909

Dermer, C.D., Schlickeiser, R., & Mastichiadis, A. 1992, A&A, 256, L27

Dunlea, S. 2001, Ph.D. thesis, University College Dublin

Ebisuzaki, S. et al. 1991, Proc. 22nd ICRC, Dublin, Ireland

Edelson, R. et al. 2002, ApJ, 568, 610

Edelson, R. & Krolik, J. 1988, ApJ, 333, 646

Ellis J., et al 2008, Physics Letters B, 665, 412

Errando M. 2009, astro-ph/0907.0994

Finley, J.P. et al. 2001, Proc 27th ICRC, Hamburg, Germany

Fortson, L. & Kildea, J. 2008, Proc. of Science 39, Palaiseau, France

Fossati, G. et al. 1998, MNRAS, 299, 433

Fossati, G. et al. 2008, ApJ, 677,906

Gaidos, J. A. et al. 1996, Nature 383, 319

Gehrels, N., et al. 2004, ApJ, 611, 1005

Ghisellini, G., Tavecchio, F. & Chiaberge, M. 2005, A&A 432, 401

Grindlay, J.E. et al. 1976, ApJ 209, 592

Grindlay, J.E. 1972, ApJ 174, L9

Heck, D. et al. 1998, http://www-ik.fzk.de/corsika/

Hill, D.A. & Porter, N.A. 1961, Nature 191, 690

Hillas, A.M. 1985, Proc 19th ICRC, La Jolla, USA

Hillas, A. M. 1996, Space Science Reviews 75, 17

Hjorth, J. et al. 2003, Nature 423, 847

Holder, J. et al. 2006 Astroparticle Physics 25, 391

Holland, S.T. et al. 2008, GCN Circular 8112

Horan, D. et al. 2009, ApJ 695, 596

Horan, D. PhD thesis, University College Dublin, 2001

Huang, D. et al.,2009 Proc. of the *Fermi* Symp.

Jenner, L. 2008, http://www.nasa.gov/missionpages/GLAST/spacecraft/index.html

Jorstad, S.G. et al. 2010, ApJ 715, 362

Katarzyński, K. et al. 2005 A&A 433, 479

Katarzyński, H. & Walczewska, K. 2010, A&A, 510, 63

Kembhavi, A.K. and Narlikar, J.V. 1999, *Quasars and active galactic nuclei : an introduction*, Cambridge University Press, Cambridge.

Kertzman, M. & Sembroski, G. 1994, Nuclear Instruments and Methods A 343, 629

Kildea, J. et al. 2007, Astroparticle Physics, 28, 182

Kildea, J. 2002 Ph. D. Thesis

Kildea, J. 2008, *Private Communication*

Klebesadel, R. W., Strong, I. B., & Olson, R. A. 1973, ApJ, 182, L85

Kranich, D. et al. 2009,Proc. 31st ICRC Lodz, Poland

Krawczynski, H., Coppi, P. S., & Aharonian, F., 2002, MNRAS, 336, 721

Krawczynski, H. et al. 2004, ApJ, 601, 151

Krennrich, F. et al. 2003, Proc. 28th ICRC Tsukuba, Japan

Krimm, H. 2008a, http://swift.gsfc.nasa.gov/docs/swift/results/transients/

Krimm, H. 2008b, http://swift.gsfc.nasa.gov/docs/swift/results/transients/Transientsynopsis.html

Lampton, M. et al., 1976, ApJ 208, 177

Levine A. M., et al. 1996, ApJ, 469, L33

Li, T.P. & Ma, Y.Q. 1983 , ApJ 272, 317

Longair, M.S. 1992, *High energy astrophysics. Vol.1: Particles, photons and their detection*, Cambridge University Press, Camvridge

Lyutikov, M. 2003, New Astr. Rev. 47, 513

Maier, G. et al. 2007, Proc. 30th ICRC, Merida, Mexico

Mannheim, K. 1993, A&A, 269, 67

Maraschi, L. et al. 1992, ApJ, 397, L5

Marscher, A.P. & Gear, W.K. 1985, ApJ, 298, 114

Marscher, A.P. et al. 2010, ApJ 710, L126

Mastichiadis, A. & Kirk, J.G. 1997, A&A, 320, 19

McCann, A., Hanna, D., Kildea, J., & McCutcheon, M. 2009. ArXiv e-prints.

Mohanty, G. et al.1998, Astroparticle Physics 9, 15

Moriarty, P. et al. 1997, Astroparticle Physics 7, 315

Mucke, A. & Protheroe, R.J. 2001, Astropart. Phys. 15, 121

Otte, A. N. et al. 2007, Proc. 30th ICRC, Merida, Mexico

Pian, E. et al. 1998, ApJ, 492, L17

Pichel, A. et al. 2009, Proc. 31st ICRC Lodz, Poland

Pichel, A. et al. 2011, Proc. 32st ICRC Beijing, China

Pichel, A. & Rovero, A.C. 2008, BAAA 51, 321, San Juan, Argentina

Piran, T. 2004, Reviews of Modern Physics 76, 1143

Pohl, M. & Schlickeiser, R. 2000, A&A, 354, 395

Protheroe, R.J. & Stanev, T. 1996 Phy Rev Lett 77, 3708

Punch, M., & Fegan, D.J. 1991, AIP Conf.Proc., 220, 321

Punch, M., et al. 1992, Nature, 358, 477

Quinn, J. et al. 1996, ApJ, 456, L83

Quinn, J. et al., 1997, Proc. 25th ICRC, Durban, South Africa

Quinn, J. 1995, MSc Thesis, Galway-Mayo Institute of Technology

Quinn, J. 1997 Ph.D. Thesis

Reynolds, P.T. et al. 1993, ApJ, 404, 206

Rees, M.J. 1978, MNRAS, 184, P61

Roming, P.W.A., et al. 2004, Proc. SPIE, 5165, 262

Scarpa, R. & Falomo, R. 1997, A&A 325, 109

Schroedter, M. 2004 Ph. D. Thesis

Senturk, G. et al. 2011, Proc. 32st ICRC, Beijing, China

Sikora, M., Begelman, M.C., & Rees, M.J. 1994, ApJ, 421, 153

Spada, M. et al. 2001, MNRAS, 325, 1559

Steele, D. et al. 2007, Proc. 30th ICRC, Merida, Mexico

Swank, J. H. 1994, American Astronomical Society Meeting, 185, 6701

Toner 2009 Ph.D. Thesis

Tavecchio, F., Maraschi, L. & Ghisellini, G. 1998, ApJ, 509, 608

Urry, C.M. & Padovani, P. 1995, PASP, 107, 803

Vaughan, S., et al. 2003, MNRAS, 345, 1271

Weekes et al.1972, ApJ 174, 165

Weekes, T.C. et al. 1989, ApJ, 342, 379

Weekes, T.C. et al. 2002, Astroparticle Phys, 17, 221

Weekes, T.C. et al. 2003, Proc. 28th ICRC, Tsukuba, Japan

Weekes, T. C. 1996 , Space Sci. Rev., 75, 1

Weekes T.C. 2003, Very High Energy Gamma-Ray Astronomy, Institute of Physics, Bristol

Weekes, T. 2007, Nature 448, 760âĂŞ762

Weinstein, A. 2007, Proc. 30th ICRC, Merida, Mexico

Woosley, S.E. & Bloom, J.S. 2006, Annual Review of Astronomy & Astrophysics 44, 507

Zhang, Y.H. et al. 2005, ApJ, 629, 686